2008

Biomolecular Shuttles under Dielectrophoretic Forces

Yongkuk Lee
West Virginia University

INTEGRATED MOTOR PROTEIN BASED NANODEVICES FOR BIOMOLECULAR TRANSPORT

by

Yongkuk Lee

BSEE, MSEE

Dissertation submitted to the College of Engineering and Mineral Resources
at West Virginia University
in partial fulfillment of the requirements
for the degree of

Doctor of Philosophy
in
Electrical Engineering

Approved by

Parviz Famouri, PhD, Committee Chairperson
Lawrence Hornak, PhD
Dimitris Korakakis, PhD
Xian-An Cao, PhD
Nianqiang Wu, PhD

Lane Department of Computer Science and Electrical Engineering
Morgantown, West Virginia
2014

Keywords: Actin filament, Myosin, Gelsolin, Unidirectional transport

ABSTRACT

Integrated Motor Protein-based Nano-devices for Biomolecular Transport

Yongkuk Lee

A living cell can be considered as a miniaturized device, which carries out complicated tasks such as reproduction, energy conversion and molecule transport. Many cellular functions are highly efficient and mostly performed at nanoscale, which is pursued in fields of Micro total analysis system (μ-TAS) or lab-on-a-chip. Due to unique mechanical functions performing micro/nano transport with high efficiency of the chemo-mechanical energy conversion in cells, motor proteins have been emphasized to perform laboratory functions such as delivery, assembly, detection, and micro/nano-engines. However, several issues ranging from *in vitro* stability of motor proteins to understanding their functionalities with inorganic materials remain unsolved and continue to hinder the applications of motor proteins. One such issue includes directional control in the motion of motor proteins. Associated filaments are precisely controlled by cellular signals and provide tracks for motor proteins to play critical roles in biological movement and transportation in cells, which is difficult to mimic *in vitro*.

This study investigates the development of a new methodology for the directional transport of particles using actomyosin. This methodology is applicable to new devices for security, health or environmental applications. The general approach to be developed is based on creating unipolar F-actin arrays on an inorganic substrate. The barbed end of actin filament is anchored on streptavidin-coated surfaces through biotinylated gelsolin. A flow field driven by a mechanical pump is utilized to lay down actin filaments aligned along the direction of the flow. Meanwhile, fascin crosslinks actin filaments to prevent their resuspension. These precisely oriented F-actin arrays provide unidirectional transport of heavy meromyosin-coated particles over distances of several hundred micrometers. In processes of creating unipolar F-actin arrays, blocking solutions are investigated to prevent non-specific binding of F-actin on streptavidin-coated surfaces. Additionally, Ca^{2+} regulated gelsolin activity with actin filament is investigated in a function of free Ca^{2+} concentrations.

The advantages of this study are 1) no external regulation and influence is required to guide HMM-coated particles or maintain F-actin arrays, 2) a linear transport of micro/nano particles to desired locations can be accomplished, and 3) patterned tracks of F-actin arrays constructed using micropatterning techniques are available for various applications. This study may provide fundamental understanding of potential roles of myosin II as a nonprocessive motor protein in further applications and may significantly improve the applicability of hybrid devices using biomolecular motor proteins.

ACKNOWLEDGEMENTS

I would genuinely like to acknowledge the help and support of the individuals who have assisted me in completing the work presented in this dissertation.

First and foremost, I would like to express my sincere gratitude to my advisor, Dr. Parviz Famouri, for not only his technical input, but also his patience and guidance while I was completing this work. It is with his mentoring and encouragement that I was able to achieve this degree and all the accomplishments within.

Furthermore, I would like to thank my committee members, Dr. Lawrence Hornak, Dr. Dimitris Korakakis, Dr. Xian-An Cao, and Dr. Nianqiang Wu for their input and technical discussions. For the same reason, I would like to thank Dr. Lloyd Carroll and Dr. Lisa Holland.

I would also like to acknowledge my lab colleagues, both past and present, for investing their time and effort into various parts of this work and the lab in general.

Last but not least, I would like to thank my wife, Kyoungnae Lee, for her patience and support because she is the person who suffered the most during the years I was studying for my degree.

TABLE OF CONTENTS

LIST OF FIGURES

LIST OF TABLES

LIST OF ACRONYMS

Actomyosin	: Actin-myosin
F-actin	: Actin filament
G-actin	: Globular actin
ABPs	: Actin-binding proteins
ATP	: Adenosine-triphosphate
ADP	: Adenosine-diphosphate
P_i	: Inorganic phosphate
ELC	: Essential light chain
RLC	: Regulatory light chain
HMM	: Heavy meromyosin
LMM	: Light meromyosin
ABSF	: 4-(2-aminoethyl) benzenesulfonyl fluoride
S1	: Subfragment-1
S2	: Subfragment-2
PMMA	: Poly(methylmethacrylate)
TMCS	: Trimethylchlorosilane
AC	: Alternating current
DC	: Direct current
DEP	: Dielectrophoresis
EO	: Electro-orientation
PMSF	: Phenylmethylsulfonyl fluoride
NHS	: *N*-Hydroxysuccinimide
PEG	: Polyethylene glycol

BSA : Bovine serum albumin

APTES : (3-aminopropyl)triethoxysilane

XPS : X-ray photoelectron spectroscopy

DMF : Dimethylformamide

T-20 : Tween-20

EGTA : Ethylene glycol tetraacetic acid

PLL : Poly-L-lysine

DTT : Dithothreitol

AFM : Atomic force microscopy

SEM : Scanning electron microscopy

GA : Glutaraldehyde

HMDS : Hexamethyldisilazane

SE : Secondary electron

BSE : Backscattered electron

CL : Cathodoluminescence

GB : Gentle mode

WD : Working distance

TEM : Transmission electron microscopy

SAXS : Small-angle X-ray scattering

ELISA : Enzyme-linked immunosorbent assay

bGA : Biotinylated gelsolin-actin

BS^3 : Bissulfosuccinimidyl suberate

DMS : Dimethyl sulfide

LUTs : Look up tables

μTAS : Micro total analysis systems

CHAPTER 1 - INTRODUCTION

1.1 Statement of the Problem

Nanotechnology, the concepts of which was first introduced in "There's Plenty of Room at the Bottom" by Richard Feynman in his lecture given in 1959, is the study focusing on development of nano-sized materials and systems. It is very challenging to manipulate materials at the atomic scale but doing so provides endless possibilities in most areas of research, including medicine, computer science, electronics and energy production. Recently, significant advances in micro/nanotechnology have occurred, due to constant efforts by researchers from various fields. This technology can help us build or manipulate complicated nano-sized structures in more detail, providing more precise control, higher efficiency and occupation of smaller space. However, despite recent advances, human-made miniaturized devices with multiple laboratory functions continue to pose a challenge.

It is not surprising that researchers frequently endeavor to mimic nanotechnology which evolved in nature for practical solutions to exceed the limit of current technology. For instance, the living cell, typically 10 μm size, can reduplicate itself, change its shape, react to environment and produce energy using a large number of different nano-sized proteins. If one can mimic or manipulate all of the cell's functionality at molecular scale, a whole new world will have arrived.

With recent development of nanotechnology and advances in molecular biology, a hybrid methodology combining synthetic nanomaterials and biological systems is emerging to improve existing nanotechnology or create new nanotechnology. This research field is often called "bionanotechnology". This novel methodology is often very attractive due to their size, function and efficiency [1].

Motor proteins and associated filaments such as actin-myosin (actomyosin) and kinesin-microtubule play critical roles in biological movement and transportation. Motor proteins transport cargo such as vesicles, chromosomes and organelles along associated filaments and aid in cell division and cell motility. Furthermore, actomyosin is used in muscle contraction to generate mechanical forces [2]. Due to precise control of these unique mechanical functions and high efficiency of the chemo-mechanical energy conversion, many researchers have focused on whether these proteins can be employed to construct nano-sized structures in synthetic environment.

To utilize the abilities of motor proteins and associated filaments in an artificial environment, directional control in the motion of motor proteins is required. Once directional control is achieved, a

broad range of applications from delivery, assembly, sorting and detection to micro/nano-engines and energy transduction can be realized for a whole new generation of hybrid bio-devices.

Since *in vitro* assay of biomolecular motor was successful, many researchers successfully demonstrated controlling the direction of cytoskeletal filaments on associated motor protein-coated surfaces or motor protein-coated beads on associated cytoskeletal filament-coated surfaces using a DC electric field [3], an AC electric field [4], a hydrodynamic flow field [5] and engineered pattern by photolithographic method [6]. However, it is still difficult to control their direction and avoid any damage to protein. Spudich's group first showed directed movement of myosin-coated beads by creating actin filament (F-actin) arrays with structural polarity on the carbon-coated electron microscope grid [7].

This dissertation describes the development of a methodology that will have applicability on the transport of specific proteins from one location to a targeted location, at which point these proteins can be further manipulated for security, health or environmental applications. The general approach to be developed is based on F-actin arrays whose structural polarity is oriented on an inorganic substrate. The barbed end of F-actin, where is capped by biotinylated gelsolin, is anchored on streptavidin-coated surface. In the presence of a flow field, F-actin is aligned along the flow, and fascin crosslinks F-actin to prevent rising from the surface. The unidirectional transport of myosin-coated particles has been successfully demonstrated on the F-actin arrays. In order for the successful development of the methodology, 1) the blocking of non-specific binding sites has been investigated, 2) Ca^{2+} regulated gelsolin activity has been shown and 3) actomyosin motility on the particle surface has been demonstrated. Furthermore, F-actin arrays have been observed via scanning electron microscopy to verify the arrangement of structural polarity.

1.2 Outline

This work addresses the development of a methodology for the directional transport of particles using actomyosin. Chapter 2 covers the background related to this work. Structures and functions of actin and myosin II are discussed. Properties of actomyosin motility including step size, force and speed are discussed. As this work uses various actin binding proteins, their functions are also discussed in detail. Literature reviews for previous works to realize directional control of motor proteins are included.

Chapter 3 contains a summary of the experimental methods used in this work. A description of microscopy and recording system is provided. The procedures of protein purification including actin and myosin II are discussed in detail. The preparation of solutions used for this work is provided. The procedure of sample preparation for AFM or SEM observation is provided. The procedures of protein biotinylation and fabrication of streptavidin-coated surface are also discussed. Data measurements developed during the duration of this work are discussed in detail.

Chapter 4 contains results and discussions for this work. The structural analysis of actin filaments using both AFM and SEM is discussed. SEM observation of actin filaments with or without HMM decoration is presented and discussed in detail. The sample preparation is also discussed in detail. During this work, a heterogeneous assay is developed to clearly understand gelsolin activity in relation to F-actin. The development of the heterogeneous assay is presented. The blocking non-specific binding sites with BSA and Tween-20 is discussed. The direct observation of actin filament interacting with gelsolin in a function of free Ca^{2+} concentrations is discussed in detail. The development of fascin-crosslinked actin arrays is also discussed in this chapter. The influence of the surface population of F-actin, the length of F-actin and the strength of flow fields on the alignment of fascin-crosslinked actin arrays is presented. The movement of HMM-coated particles on the arrays is discussed. The development of patterned arrays is also covered.

Finally, Chapter 5 contains future direction for this work. The development of highly ordered self-assembled actin tracks is discussed in detail.

CHAPTER 2 – BACKGROUND

2.1 Structure and Function of Actin

Actin was first isolated in 1942 from muscle [8], where it forms stable microfilament systems assembled within myofibrils. While the highest concentrations of actin (about 20% of total protein) are found in muscles [9], actin is one of most abundant proteins found in many eukaryotic cells and plays an important role in various cellular functions. These functions include, but are not limited to, maintaining cell shape, cell division, cell motility, and intracellular transport processes. To support such cellular functions, actin, like other cytoskeletal filaments such as microtubules, has the ability to assemble and disassemble depending on cell requirements.

Actin exists in two forms: monomeric units of actin called G-actin and polymeric filaments called F-actin, which is made up of many G-actin monomers. Actin undergoes reversible transformation between monomeric state (G-actin) and filamentous state (F-actin) under the control of nucleotide hydrolysis and ions [10]. In addition, a large number of actin-binding proteins (ABPs) exist to control the dynamics of actin. ABPs interact with actin molecules in order to inhibit or stimulate actin polymerization, crosslink actin filaments into linear bundles or in three-dimensional gels, or couple actin filaments to specific locations such as cell membranes.

The structure of actin has been extensively investigated. Actin consists of a single polypeptide chain of typically 375 amino acid residues with a molecular weight close to 42 kDa [11]. In the electron microscope, G-actin is in a globular shape with overall dimensions of $5.5 \times 5.5 \times 3.5$ nm. However, three-dimensional structure of X-ray analysis reveals that G-actin consists of two domains, which are further subdivided into two subdomains referred as subdomain 1 – 4 as shown in Figure 2.1.

There are two clefts formed between the domains. The upper cleft, called a deep cleft, between subdomain 2 and 4 binds the nucleotide (adenosine-triphosphate, ATP or adenosine-diphosphate , ADP) and associated divalent metal ions (Ca^{2+} or Mg^{2+}). The binding of nucleotide affects the conformation of actin molecule. The lower cleft between subdomain 1 and 3 is hydrophobic. This cleft plays an important role in actin polymerization and binding with most ABPs, therefore this cleft is called hydrophobic or target binding cleft [11].

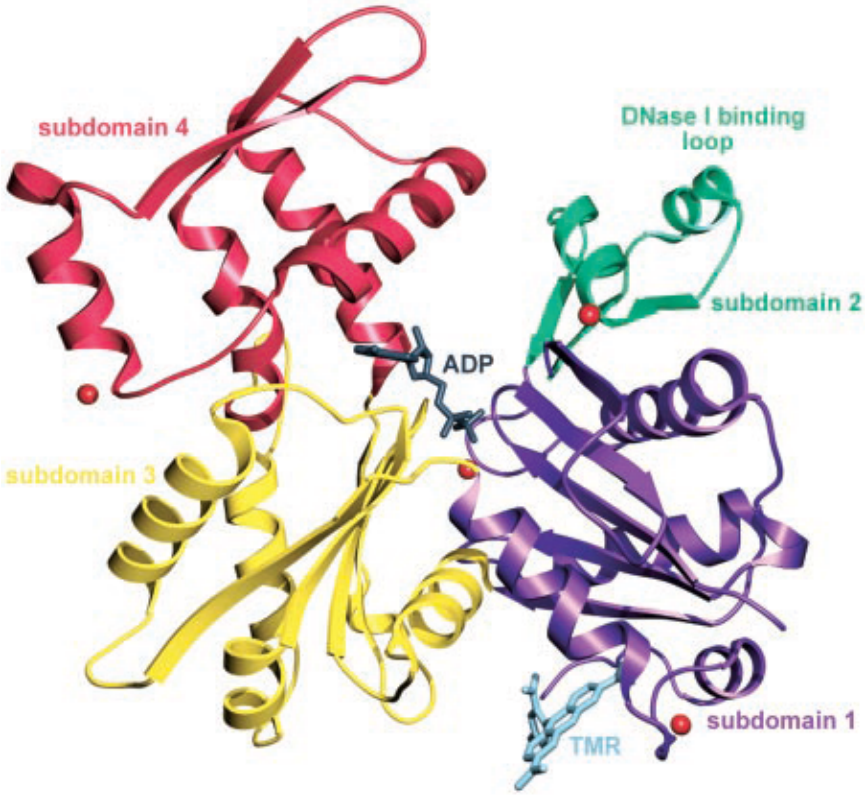

Figure 2.1 Ribbon representation of the actin structure in the ADP state. G-actin consists of four subdomains. A deep cleft is located between subdomain 2 and 4, while a target binding cleft is located between subdomain 1 and 3 [12].

G-actin can be polymerized into filamentous actin called F-actin [10, 13]. In 1990, Kenneth C. Holmes *et al.* proposed three-dimensional structures of G-actin and F-actin according to X-ray fiber diffraction patterns [14]. Each G-actin binds with two other G-actins rotated by 166 °in the actin filament. As a result, 13 monomeric subunits of actin form a 36 nm loop of helix. F-actin consists of two parallel actin strands twisted around each other in a right-handed helical formation approximately 7 – 8 nm in diameter. F-actin is relatively flexible compared to microtubules with hollow cylindrical structures composed of 13 parallel protofilaments formed by tubulin subunits [2].

Actin dynamic is regulated by the ionic strength of solutions and the critical concentration of G-actin *in vitro* while more regulating factors including actin binding proteins such as cofilin, profiling, CapZ, gelsolin etc. exist *in vivo* [15]. In Actin polymerization *in vitro*, if the ionic strength is increased to physiological levels and the concentration of G-actin is higher than the critical concentration, then G-actin

polymerizes into F-actin spontaneously. In other words, F-actin can depolymerize to G-actin in low ionic strength or below the critical concentration. The *in vitro* actin polymerization proceeds in three sequential stages: nucleation, elongation, and steady state as shown in Figure 2.2. Even under polymerizing condition, actin molecules cannot be polymerized directly. To start polymerization, actin molecules must assemble into nucleus. The nucleus is stable and acts as a seed for elongation. The nucleation is relatively slow, thus this stage is known as the rate-limiting step in the process of polymerization. If F-actin fragments are added at the nucleation stage, they act as nuclei, so elongation can start without any lag period. After ATP bound G-actin is incorporated into a filament, the bound ATP is slowly hydrolyzed to ADP. This hydrolysis of ATP does not generate any energy in the process. ATP is not required for polymerization since ADP bound G-actin also polymerizes. However, ATP bound G-actin is easier to polymerize than ADP bound G-actin.

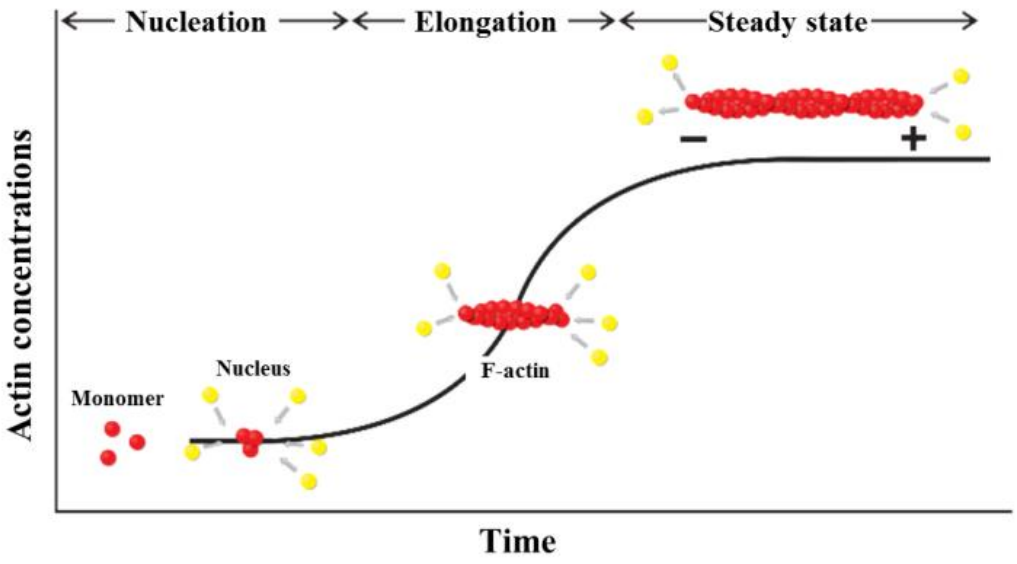

Figure 2.2 Three phases of actin polymerization: nucleation, elongation, and steady state. Adapted from [16].

In the elongation stage, actin monomers are added to both ends of growing filament. Both ends have different kinetic rate constants for association and dissociation, k_{on} and k_{off}, respectively, which are related to the growth and shrinkage rate of each end. For example, one end of the filament grows faster than another end of the filament, so called plus end and minus end, respectively. The unequal growth rates at

the two ends can be demonstrated. When short myosin-decorated filaments acted as the nuclei during polymerization, electron microscopy showed much longer undercoated filament can be found at the plus end. In contrast, the plus end shrinks faster than the minus end during the depolymerization of actin. The elongation stops when equilibrium is reached between filaments and monomers, a stage which is called steady state. At this stage, the assembly of G-actin to the filament is not ceased. However, the disassembly rate is identical to the assembly rate, so the filament maintains a constant length. This phenomenon is known as treadmilling [2]. The newly associated subunits at the plus end travel through the filament until they reach the minus end, where they dissociate.

F-actin has structural polarity. When G-actin is polymerized to F-actin, the clefts of all polymerized G-actin are arranged toward the same end of the filament, the minus end. The polarity is verified by electron microscopy [17] when F-actin is decorated with myosin S1 fragment as shown in Figure 2.3. Arrangements of Myosin S1 binding to F-actin show arrowhead patterns. The pointed end of the arrowhead indicates the minus end, while a barbed end indicates the plus end. The polarity of F-actin can be also determined by the direction of myosin movement when it walks along F-actin. Most classes of myosin (except myosin VI) move along F-actin toward the plus end [2].

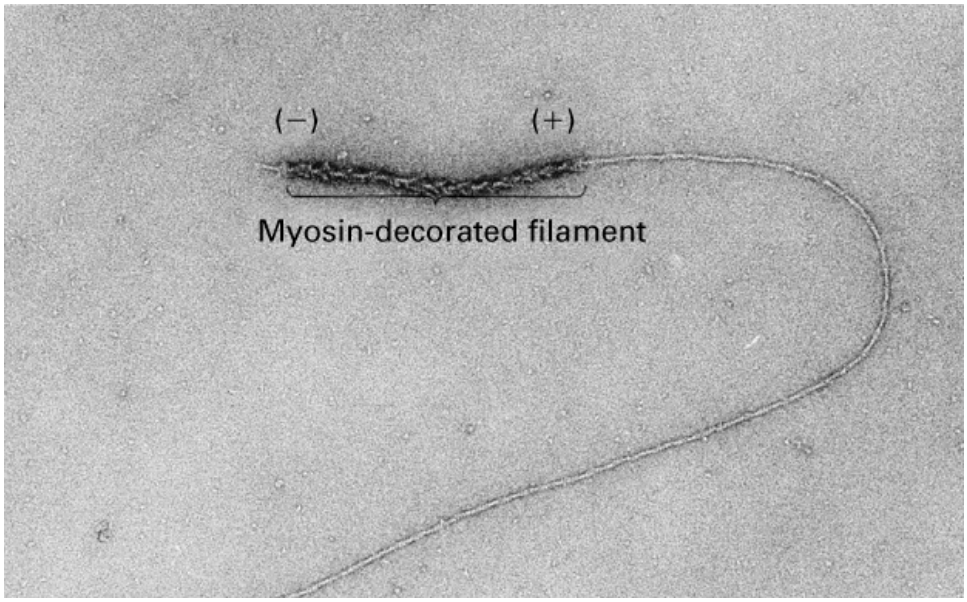

Figure 2.3 Electron microscopy of F-actin decorated with myosin S1 fragment. It shows an arrowhead pattern as myosin S1 binds. Pointed end of arrowhead indicates the minus end of F-actin [16].

Some natural toxins bind to F-actin or actin monomers and prevent depolymerization of F-actin or polymerization of actin monomers. Cytochalasins, a group of fungal metabolites, and Latrunculins, toxins produced by certain sponges, including genus *Latrunculia*, inhibit the formation of F-actin through different mechanisms [18-21]. Cytochalasins bind to the plus end of F-actin, resulting in depolymerizing filaments as blocking further addition of subunits, while Latrunculins binds to G-actin and prevents it from attaching to ends of filaments. Phalloidin from the fungus *Amanita phalloides* (the "angel of death" mushroom) binds to the space between two subunits of F-actin and causes a reduction in the kinetic rate for dissociation in both ends in filaments [21]. As a result, Phalloidin prevents depolymerization of F-actin. F-actin labeled by Phalloidin is stable even when the actin solution is diluted below its critical concentration. The actin binding properties of Phalloidin is not altered after the conjugation with fluorescent analogs. Therefore, Phalloidin has provided an enormously useful tool to localize F-actin both *in vivo* and *in vitro*.

2.2 Actin binding proteins

There are a large number of actin binding proteins interacting with actin to fulfill cellular functions. Some promote actin depolymerization by binding G-actin or capping the plus end of F-actin while others form a nucleus with actin to accelerate actin polymerization. In addition, some actin binding proteins crosslink F-actin to form focal adhesions for aiding cell movements. These proteins can be classified as follows: actin monomer binding proteins, capping proteins, crosslinking proteins, and membrane attachment proteins. Some isolated and characterized actin binding proteins are introduced in order to understand how they work with actin in cells.

Controlling actin polymerization and depolymerization in cells is performed by a different mechanism as compared to *in vitro* assays. Cells usually maintain high ionic concentrations, in which actin should be polymerized into filaments. In addition, the actin concentration in cells is much more than the critical concentration. However, many cells contain large pools of G-actin. Measurements using DNase I inhibition assays show that at least 40% of actin in cells is unpolymerized [22]. Therefore, it is generally believed that there are actin sequestering proteins preventing actin polymerization. Due to its high concentration in cells and its ability to bind G-actin but not F-actin, thymosin β_4 is considered the main actin sequestering protein. Thymosin β_4 (5,000 MW) forms a 1:1 complex with G-actin to block the ATP-binding site, thereby preventing its polymerization. The increase of thymosin β_4 binding G-actin causes the decrease of F-actin due to low G-actin concentration available for actin polymerization [23].

Some actin binding proteins bind to actin filaments and sever them to create fresh minus ends. These proteins have been called actin severing proteins. Gelsolin (87,000 MW) and severin (40,000 MW) are known as actin severing proteins [24]. To assist rapid disassembly of actin filaments or filament networks in cells, actin severing proteins break down actin filaments. After they sever a filament, they remain bound at new plus ends, which results in preventing the growth of filaments. Meanwhile, actin subunits at the minus ends of shortened filaments are disassembled until the actin monomer concentration reaches the critical concentration for the minus end. Activity remaining bound at the ends of filaments is called capping, so those actin severing proteins are also called actin capping proteins. Although the capping activity in gelsolin and severin aids rapid disassembly of actin filaments, some capping proteins cap ends of filaments in order to stabilize their organization. For instance, tropomodulin (40,000 MW) [25] caps the minus end of actin filaments while CapZ (36,000 MW) [26] caps the plus end of actin filaments in a muscle sarcomere. As they prevent actin thin filaments from addition or loss of actin subunits at each end, the structure of the muscle sarcomere is able to be maintained.

Actin filaments can form stable networks and bundles in a broad range of cytoskeletal structures such as filopodia, microvilli, lamellipodia, and stress fibers. In such structures, there are proteins interacting with actin filaments to manage the dimensions and mechanical properties of the structures. As mentioned previously, these are called actin crosslinking proteins. These proteins crosslink actin filaments to create actin networks or bundles to serve specific biological functions, as shown in Figure 2.4. Several different actin crosslinking proteins often exist in the same structure to improve its structural stabilization. Most actin crosslinking proteins have a pair of actin-binding domains, but the distance between actin-binding domains varies. The distance between actin-binding domains in small actin crosslinking proteins such as fimbrin (68,000 MW) [27], α-actinin (102,000 MW) [28], villin (95,000 MW) [29], and fascin (55,000 MW) [30] is close enough to bind actin filaments into bundles, where actin filaments are packed tightly. Tightly bundled actin filaments provide stiffness, which is required in cell extensions or maintaining biological structures. Some actin crosslinking proteins such as spectrin (280,000 MW) [31], dystrophin (427,000 MW) [32], and filamin (280,000 MW) [33] have actin-binding domains, which are farther at the end of flexible arms. These actin crosslinking proteins bind the sides of two different actin filaments to create large, loosely packed actin networks. The physical properties of those actin networks are similar to gels, so are often called actin gels.

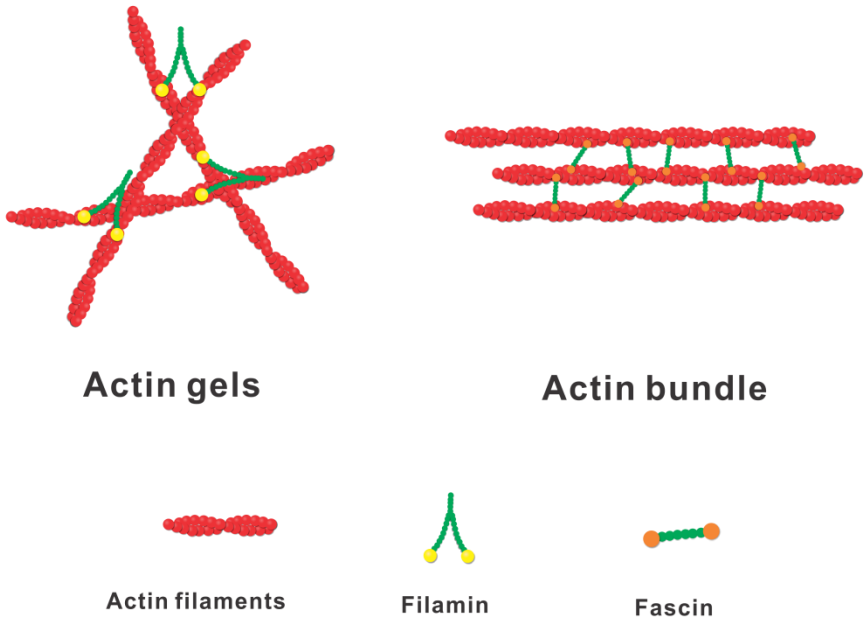

Figure 2.4 Actin networks and bundles. Some actin crosslinking proteins like filamin create actin gels while others, like fascin, bind actin filaments into bundles. Adapted from [34].

Large three-dimensional actin networks and bundles are generally found beneath the plasma membrane. These bundles and networks associate with the plasma membrane to perform a variety of cell surface activities, including cell shape. For instance, when the membrane is associated with dense actin bundles, it may form the fingerlike shape of microvillus. When associated with loose actin networks, these networks may allow red blood cells to have strength and flexibility, which make red blood cells squeeze through the body's blood capillaries without damage in their membrane.

To stabilize the association between the actin structures and membranes, actin structures are attached to the overlying membrane with proteins called membrane attachment proteins. Membrane attachment proteins connect actin filaments or actin binding proteins to specific membrane proteins. Ankyrin is one of the membrane attachment proteins. Ankyrin allows the spectrin-actin based cytoskeleton to connect to band 3 protein, an integral membrane protein [35].

An additional connection between the spectrin-actin based cytoskeleton and the plasma membrane is performed by band 4.1 protein. Band 4.1 protein connects spectrin-actin junctions to the integral membrane protein, glycophorin [36]. A membrane attachment protein called dystrophin can be found in skeletal muscle tissue. Dystrophin is a flexible rod-shaped cytoplasmic protein which forms dimers in order to link actin filaments to transmembrane proteins residing on the muscle cell plasma membrane. As a result, dystrophin plays an important role in stabilizing sarcolemma during muscle contraction or stretch [32].

Stress fibers composed of bundles of 10-30 actin filaments, cross-linked by α-actinin, are found in non-muscle cells. As stress fibers can anchor to the cell membrane or other substrates such as the extracellular matrix, they promote cell motility and contractility [37]. These contact sites are called focal adhesions. The attachment between stress fibers and substrates, which is not yet well understood, may be mediated by several membrane attachment proteins. For instance, α-actinin, which forms bundles with actin filaments in stress fibers, binds to the cytoplasmic domains of integrins [38]. Talin also plays a role in the attachment of actin filaments in stress fibers to the membrane. Talin binds to integrins and vinculin, which is an actin binding protein, found in stress fibers [38].

2.3 Structure and Function of Myosin

The first motor protein identified was myosin II due to its role in skeletal muscle contraction. In muscle, myosin II molecules form large bipolar thick filaments, in which several hundred myosin heads are oriented in opposite directions, moving along the adjacent actin-based thin filaments to generate contraction [39, 40]. It was initially thought that myosin was present only in muscle, but a large number of myosin types with different functions and structures have been discovered in the realm from animals to plants. Some myosins such as myosin VIII and myosin XI have been found only in plants, but most types of myosin can be found in all eukaryotes [2, 41].

Most myosin heavy chains generally consist of three distinct regions: a recognizable head domain at the N-terminus; a neck region where light chains bind; C-terminal tail domains, which have been diversified during evolution to allow the proteins to interact with a variety of cargos and/or to dimerize other subunits [41].

Myosin I, first found as unconventional myosin in amoebae, is a single-headed myosin with a relatively short tail. Unlike myosin II, myosin I does not form filaments, but its tail domain contains membrane binding sites. With the membrane binding sites, myosin I often acts as cross-linker between the actin bundles and the membrane in microvilli. In addition to the attachment of the cytoskeleton to the membrane, myosin I also supports a variety of cellular functions including intracellular transport [42].

Next to myosin II, myosin V is probably the most studied myosin. Myosin V has two heavy chains like myosin II except a longer neck region, which contributes to longer step size up to 36 nm. In addition to the large step size, myosin V is a processive motor protein. These properties make myosin V ideally suited for its role in intracellular transport. In most eukaryotes, long-range intracellular transport is performed with microtubule, but short-range intracellular transport at the cell periphery occurs with actin-based movement. Myosin V often involves such intracellular transport towards the plasma membrane [41].

Myosin VI was first identified in *Drosophila*. It is not clear whether myosin VI functions as a monomer or dimer (or possibly both) in cells, but it functions as a processive dimeric motor protein and as a nonprocessive monomeric motor protein *in vitro*. Myosin VI appears to be unique among myosin superfamily members because of an inserted sequence called the “reverse gear” between head domain and neck region. It enables myosin VI to walk towards the minus end of actin filaments while all other myosins travel in the opposite direction along actin filaments. As a minus-end directed motor protein, myosin VI may have unique cellular functions and properties. Although precise polarity of actin filaments in cells is not well established, it is believed that actin filaments have their plus ends toward the plasma

membrane. Therefore, myosin VI would transport cargo away from the plasma membrane into the cell [41]. Figure 2.5 shows an example for different functions of some myosins.

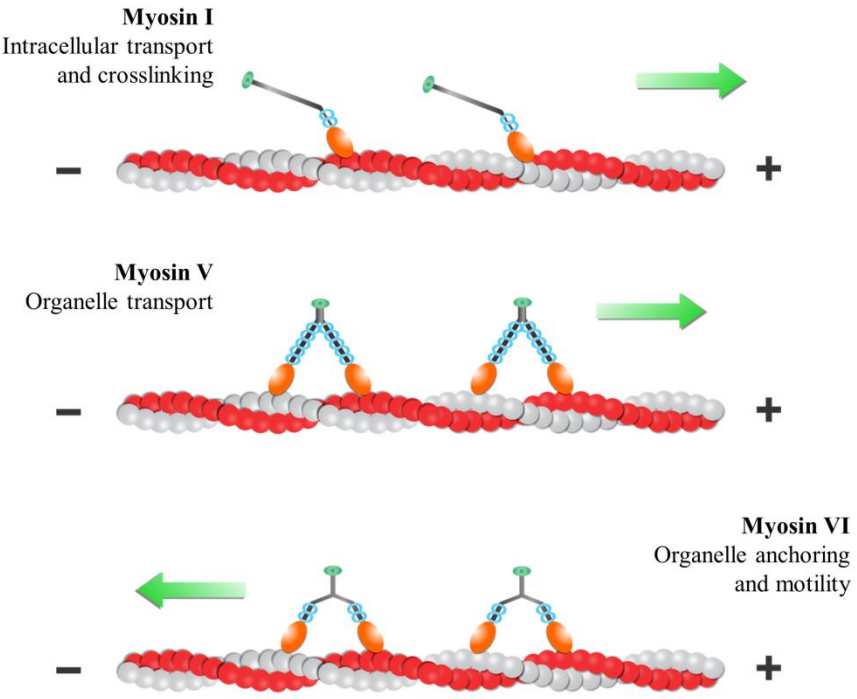

Figure 2.5 Different structures and functions of some myosins. Adapted from [43].

The atomic structures of myosin II have been revealed by X-ray crystallography as shown in Figure 2.6 [44, 45]. Crystallography shows myosin II is composed of two heavy chains and four light chains. One heavy chain consists of a globular head domain, neck region, and tail domain. The length of the head domain in myosin II is about 20 nm with 5 nm in diameter and the length of tail is about 130 nm to 140 nm and 2 nm in diameter [2]. The head domain, also called a motor domain, contains an actin-binding site and nucleotide-binding site.

Hydrolysis of ATP occurs at the nucleotide-binding site in the head domain, which creates energies to force mechanical movement in the reaction between myosin and actin filaments. In the ATP hydrolysis cycle, the nucleotide-binding site becomes closed, which generates a small movement. This movement is amplified through the neck region. The neck region, an 8-nm-long α-helix, extends from near the

nucleotide-binding site to the COOH-terminus of the heavy chain. It is also called the light-chain binding domain because two distinct light chains; essential light chain (ELC) and regulatory light chain (RLC), are bound for the structural stabilization of the neck region. Through the neck region, especially at the area known as the "lever arm", the small angstrom-sized movement in the nucleotide-binding site is amplified into a large nano-sized motion [45].

The length of the lever arm is considered an important factor in determining the strep size in motor proteins. For instance, myosin V has a lever arm three times longer than myosin II, so the step size in the hydrolysis of single ATP molecule is about 36 nm for myosin V while the step size of myosin II is about 5.5 nm [46-49].

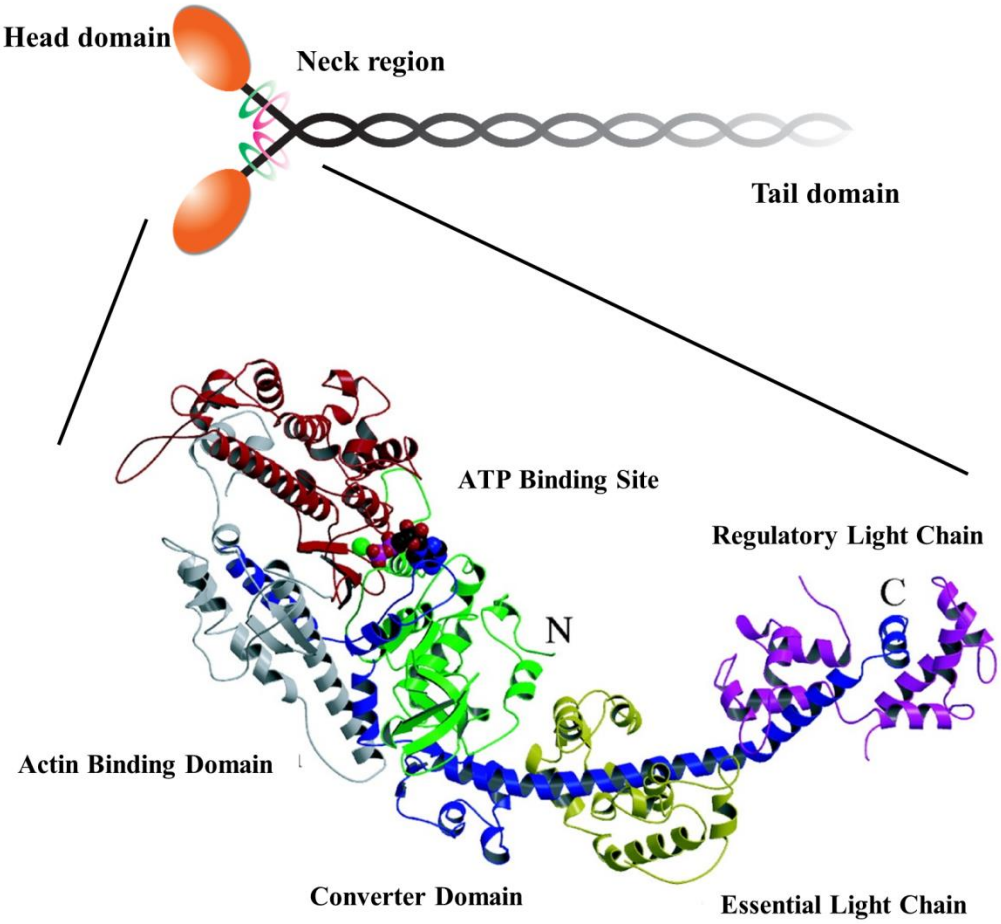

Figure 2.6 Atomic structure of myosin II. Myosin II is composed of two heavy chains and four light chains. One heavy chain consists of a globular head domain, neck region, and tail domain. Adapted from [45].

It is widely believed that the neck region rotates during the hydrolysis of ATP, due to the converter domain, forming a junction between the head domain and the neck region. The converter domain creates a rotation of the neck region by more than 70 degree in a nucleotide-dependent manner. As a result, myosin II walks along the actin filament by the angular rotation of its lever arm. The concept of the converter domain is useful to explain the reversed directionality of myosin VI. Myosin VI has the inserted sequence in the converter domain, which may reverse the direction of the rotation [50].

The tail domain is very long amino acid sequence wrapping around another tail domain of another heavy chain to form α-helical coiled-coil tail reactions. These tail-tail interactions often play important roles in living organisms. Myosin II forms large bipolar thick filaments by tail-tail interactions in skeletal muscle, which interact with actin thin filaments to be responsible for muscle contraction.

Myosin II can be cleaved by proteolytic digestion. Full-length myosin II is cleaved by α-chymotrypsin into heavy meromyosin (HMM), which is composed of two head domains, light chains and some coiled-coil tail domains, and light meromyosin (LMM), composed of coiled-coil tail domain,. The digestion reaction of α-chymotrypsin is stopped by 4-(2-aminoethyl) benzenesulfonyl fluoride hydrochloride (ABSF), a protease inhibitor. The molecular weight of HMM is known to be approximately 340 kDa and the molecular weight of LHH is known to be approximately 150 kDa while the molecular weight of full-length myosin II is known to be 500 kDa [51].

Proteolytic digestion in HMM is performed by papain. It cleaves HMM into HMM subfragment-1 (S1) which is composed of two head domains and light chains and HMM subfragment-2 (S2) which is composed of coiled-coil tail domains [51].

In our research, heavy meromyosin (HMM) from myosin II in rabbit muscle is used due to its high motor activity. Native myosin II and HMM subfragment-1 can drive movement of F-actin *in vitro* but HMM is the fastest motor among them [52]. The reason HMM produces quicker movement of F-actin than full length myosin is still under investigation but some researchers think it is due to tail domain [53]. Tail domains might regulate the activity of myosin head domains or interact with F-actin so that movement of F-actin can be reduced.

2.4 Mechanism in the Movement of Myosin

As mentioned earlier, myosin changes its conformation during hydrolysis of ATP in the head domain of myosin. The conformation is designated from the head domain but it is amplified through the neck region, especially at “lever arm”, an area which is structurally stabilized because light chains are bound. Hydrolysis of ATP is associated with binding affinity changes of myosin head for F-actin. As a result, the conformation in the head domain doesn’t occur without F-actin binding [2].

Figure 2.7 shows the actomyosin crossbridge cycle during hydrolysis of ATP. When there is no nucleotide like ATP and ADP in the nucleotide binding site (a large cleft on the back of the head domain), myosin heads are tightly bound to F-actin as shown in Figure 2.7A. This state is called a “rigor” state and is used to check the status of F-actin in our research.

When a molecule of ATP is bound to nucleotide binding site, it causes weak affinity between the F-actin binding site in myosin head and F-actin as shown in Figure 2.7B. Experimentally, the velocity of F-actin moving across the myosin-coated surface is proportional to the concentration of ATP. However, if the concentration of ATP exceeds a certain concentration, the movement of F-actin becomes slower. This is because myosin stays in this state longer with a higher concentration of ATP, contributing to the number of myosins which are bound to F-actin, causing F-actin movement to decrease. Eventually, the movement of F-actin is stopped or F-actin which is bound to myosin escapes from myosin with a higher concentration of ATP.

When hydrolysis of ATP occurs from the nucleotide binding site, there is a large conformational change in the lever arm as shown in Figure 2.7C. During hydrolysis of ATP, the nucleotide binding site becomes close and this movement causes small rotations in a converter domain located at the end of the lever arm near the head domain. This small movement at the converter domain can swing the lever arm, 8.5 nm long α-helix. This swing causes approximately 5 nm movement in the far end of the lever arm. Thus, the length of the lever arm is considered an important factor to determine movement speed in myosins. For example, myosin V has a lever arm three times longer than myosin II so the step size in hydrolysis of a single ATP molecule is 30 to 40 nm for myosin V, while the step size of myosin II is 5 to 10 nm. In this state, ATP is decomposed into ADP and inorganic phosphate (P_i) by the reaction with water but ADP and P_i remain in the myosin head. As the myosin head binds the new site of F-actin, inorganic phosphate is released from the head domain, concurrently causing tight binding of the myosin head to the new site of F-actin as shown in Figure 2.7D.

Releasing inorganic phosphate from head domain also triggers the power stroke in the next state. After releasing inorganic phosphate, phosphate causes the nucleotide binding site to open and ADP is released. As a result, a long lever arm is swung by this small change which is caused by the converter domain connecting the movement of the nucleotide binding site. However the direction of this swing is opposite from the swing caused during hydrolysis of ATP, as shown in Figure 2.7E. This swing is called “power stroke” because a movement of F-actin is created by this conformational change in myosin. At the end of the cycle, myosin is in a state, called the rigor state, and the myosin head binds to a new site on the F-actin.

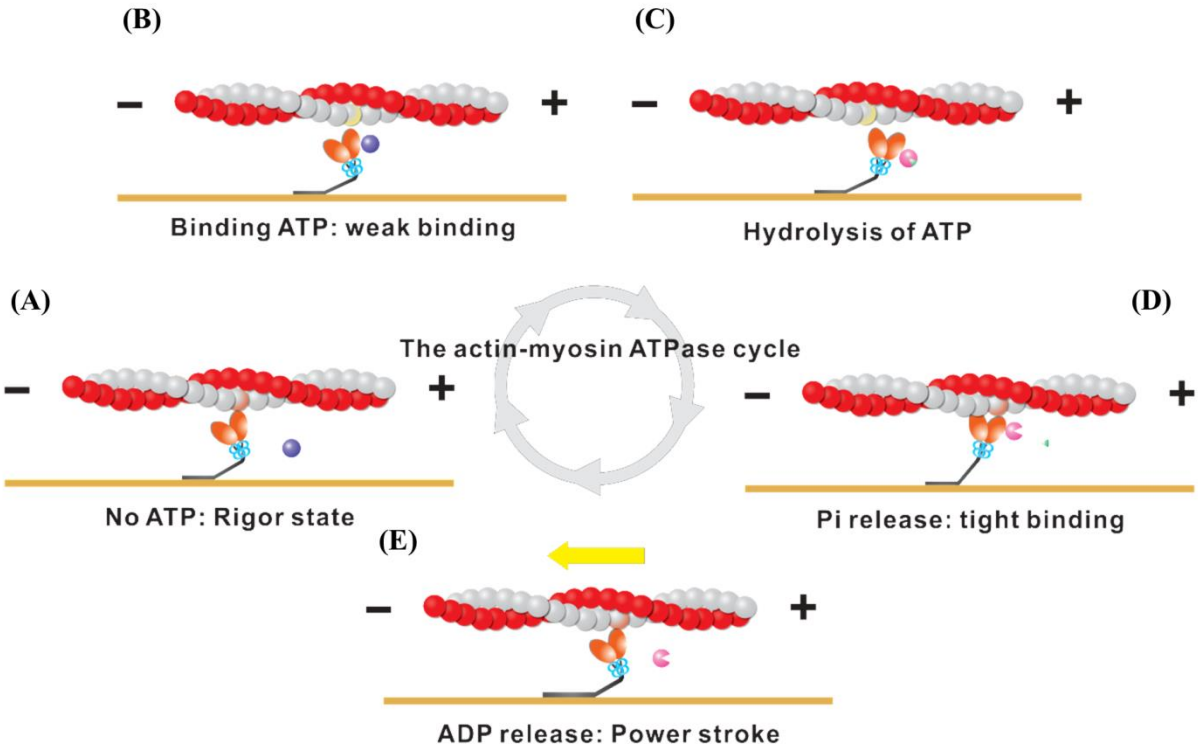

Figure 2.7 The actomyosin crossbridge cycle during hydrolysis of ATP. Adapted from [2].

2.5 *In vitro* assay

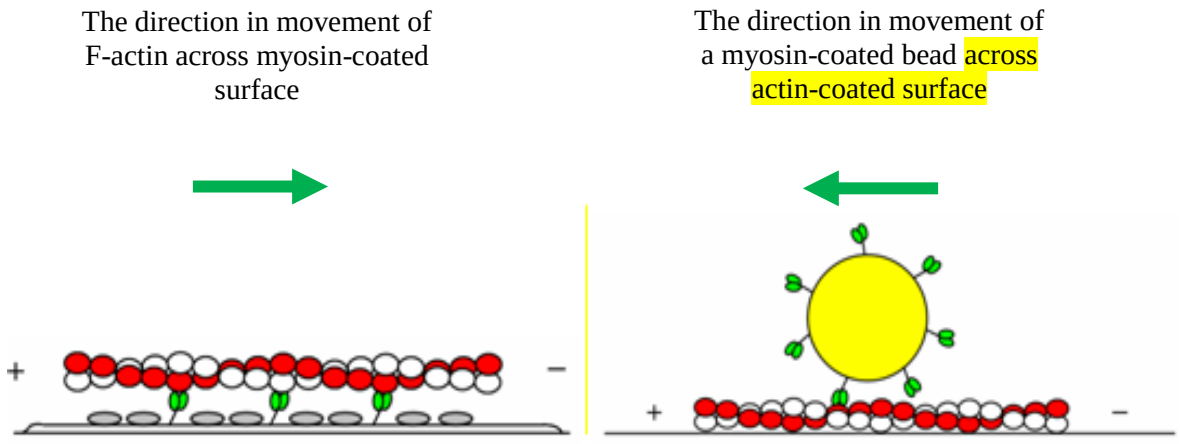

Figure 2.8 Comparison between the gliding assay and the bead assay. Adapted from [54].

The development of motility assay in cell-free conditions helps the study of motor proteins. In 1983, M. P. Sheetz *et al.* demonstrated unidirectional movement of fluorescent beads coated with purified HMM along actin cables in the algae, *Nitella*, which has the same polarity [55]. J. A. Spudich *et al.* then reported the first completely reconstituted assay in which an oriented array of purified actin filaments was constructed using severin as protein anchor on the surface of a grid. Myosin-coated beads were observed to move along the array [7]. In 1986, S. J. Kron *et al.* developed a simple and controllable *in vitro* assay for myosin motility which is most employed for the study of myosin movement along actin filament [56]. In this experiment, single actin filaments were stabilized using fluorescent conjugated phalloidin and moved in random manner on myosin filament-coated glass surfaces.

To make *in vitro* assay for actomyosin motility, two different methods of the motility assay are employed. Depending on the place where myosin is fixed in the assay, one is called "bead assay" and another is called "gliding assay" [57]. For the bead assay, myosin is immobilized on beads moving along F-actin. In this assay, actomyosin motility causes the movement of beads across the surface coated by F-actin. Studies of M. P. Sheetz *et al.* in 1983 [55] and J. A. Spudich *et al.* in 1985 [7] utilized the bead assay to observe actomyosin motility. In contrast to the bead assay, for the gliding assay, myosin is immobilized on a surface, for example, a glass slide, and F-actin moves across the myosin-immobilized surface. For both assays, myosin molecule-surface interaction is a key to success in actomyosin motility. In early studies, salinized surface [58] or nitrocellulose-coated surface [52] was used to immobilize

myosin molecules on the surface while retaining the abilities of myosin to support the movement of actin filaments. Further investigations of myosin molecule-surface interactions [59-61] discovered that surface properties such as hydrophobicity or surface charge are critical for actomyosin motility *in vitro*. High-quality motility is generally found on hydrophobic surfaces and positive charged surfaces while poor motility is observed on hydrophilic surfaces and strongly negatively charged surfaces. More detail will be discussed in Chapter 4.

In vitro studies have revealed several important properties of myosin II. The forces and steps of motor proteins have been measured using single-molecule techniques. In these techniques, a single motor protein is held in the probe of AFM to interact with filaments or a filament is held in optical tweezers to interact with motor proteins. Both AFM and optical tweezers should be able to measure piconewton forces and sense subnanometer displacements.

Finer *et al.* developed the three-bead assay, in which a single actin filament suspended between two beads, each held in independent optical tweezers, was placed above a third bead, on which myosin molecules were bound at low surface density [62]. In this geometry, F-actin was prevented from diffusing away from myosin during the detached phase of the crossbridge cycle. The three-bead assays were popularly used to study actomyosin interaction, since it was possible to measure force as well as displacement. The maximum force generated by myosin molecules has been measured, and it ranges from 1 pN to 10 pN [49, 62-64]. In earlier measurements [62, 65], the working distance of myosin II was varied. However, recent study found the working distance was approx. 5 nm using the three-bead assay [49]. A similar observation was made with a scanning probe [47]. Mysoin S1 was biotinylated, and the scanning probe was coated with streptavidin so that myosin S1 could be captured. The displacements resulting from interactions of myosin heads and actin filaments indicated the working distance of myosin II is approx. 5.3 nm.

When myosin II moves along the actin filament, it follows a path parallel to the axis of the actin filament. In other words, myosin II doesn't follow the two-stranded helix of actin filament that would result in one rotation of myosin II around actin filament every 72 nm (the full loop of a helix). Suzuki *et al.* developed a method in which a bead was covalently coated with gelsolin to be selectively attached to the end of an actin filament [66]. In this method, the sliding force and the torque generated during the actomyosin crossbridge cycle were measured. Suzuki *et al.* found that actin filaments did not completely rotate as they glided across myosin-coated surfaces. This observation coincides with other biological and structural considerations. For example, if myosin II follows the two-stranded helix of actin filament, a torque will be generated, which would disrupt the arrangement of actin and myosin filaments in muscle.

The speed of motor proteins moving along their filaments varies. Generally, nonprocessive motor proteins like skeletal myosin II (approx. 4 μm/s) [56] are significantly faster than processive motor proteins such as conventional kinesin (approx. 0.8 μm/s) [67] or myosin V (approx. 0.3 μm/s) [68]. An exception is myosin XI. Myosin XI is a processive motor protein with 35 nm steps, but it moves at 7 μm/s [69]. The processivity of motor proteins can be understood using the concept of the duty ratio [54]. The duty ratio is the fraction of the time that each motor domain spends attached to its filament in the ATPase cycle. If a myosin head attaches to an actin filament most of the ATPase cycle, the duty ratio will be large, while the duty ratio will be small if it detaches to the filament most of ATPase cycle. Non-processive motor proteins such as myosin II have a low duty ratio. As a result, a certain density of myosin molecules on the surface is required for continuous movement of actin filaments. Otherwise, actin filaments dissociate from myosin-coated surfaces [70]. In contrast, processive motor proteins such as kinesin have a high duty ratio, so a single molecule of processive motor proteins is enough for continuous movement of its filaments [67]. When the viscosity of the buffer solution increases, the observation of continuous movement of filaments is possible for processive motor proteins at lower densities than the threshold density. Viscous solutions slower the diffusion of filaments away from the surface. Unlike non-processive motor proteins, however, the velocity of filaments was proportional to the density of motor proteins at lower densities [71].

The speed of motor proteins may vary depending on physiological conditions. The concentration of ATP influences the speed of motor proteins. In lower concentration of ATP, the ATPase rate of motor proteins is slower. As a result, the speed of motor proteins becomes slower. Temperature is one of the factors having influence on the ATPase rate of motor proteins [72, 73]. Kawai *et al.* studied the influence of temperature on sliding force, velocity, and unbinding force generated during F-actin-HMM interaction [73]. To measure the forces, optical tweezers were used, and F-actin was bound to a polystyrene bead while it interacted with HMM immobilized on the surface. The study demonstrated that the velocity of F-actin propelled by HMM increased as temperature increased. For instance, the velocity of F-actin was approx. 2 μm/s at 20 ℃, while it was approx. 10 μm/s at 35 ℃. Kawai *et al.* found that the increase of the velocity was due to the increase of ATPase rate. However, temperature change did not affect the sliding force, which suggests that a particular architecture is required for force generating applications using an actomyosin system.

2.6 Applications of motor proteins

Motor proteins can be considered as dedicated nano-sized mechanical components which are much smaller than those fabricated with current technologies. They are powered by chemical energy, derived by ATP hydrolysis, and its efficiency is remarkable [74]. These biological mechanical systems therefore have received attention because of their great potential for applications such as a nano-scaled actuator or transport system in an artificial environment.

Controlling the direction of motility movement is essential to achieve technological goals. Various scientific methods including engineered tracks, driven flows, electric fields, and bio-mimic approaches have been investigated to gain directional control. Here, we introduce each, with associated limitations. Examining each approach will give us fundamental understanding of current motor protein-related applications and may provide the guideline for the next step we pursuit.

2.6.1 Engineered tracks

H. Suzuki *et al.*, in 1997 demonstrated a technique to regulate the trajectory of the actin sliding movement in actin-myosin motility [75]. HMM molecules bind to poly(methylmethacrylate) (PMMA) with high affinity. PMMA is a positive photoresist, which can be patterned on the glass substrate by photolithography. As a result, actin-myosin motility can only happen on PMMA tracks where HMM molecules bind, as shown in Figure 2.9. The data showed that the movement of actin filaments was restricted to move only on PMMA tracks. It was also found that there is no significant movement of actin filaments on a bare glass surface, and the sliding movement on PMMA tracks is comparable to movement on the nitrocellulose surface.

However, the data also indicated several critical problems to be solved. 1) The PMMA tracks were not restricted with any sidewall, so actin filaments easily fell off the tracks. As a result, the population of actin filaments on the tracks was not controllable. 2) The PMMA tracks only regulated the trajectory of the actin movement but not the polarity of F-actin, so bidirectional movement of actin filaments was observed. 3) Technical limitations of conventional UV photolithography affected the width of the PMMA tracks (1-2 μm), which caused actin filaments to turn around on the tracks.

To prevent actin filaments from turning around and falling off the pathway, nano-scaled channels were used. Y. Arai *et al.* (1999) found that an actin filament has been shown to break when it is forced to be bent too sharply. The actin filament bent to a radius of only 0.2 μm before breaking [76]. This suggested that actin filaments will not turn around in channels below 0.2 μm. A better understanding of actin filament had great influence on later development of engineered tracks for motility.

R. Bunk's group demonstrated the control of the direction of actin-myosin motility by combining two different methods: fabrication of nano-sized channel structure and chemical functionalization of surfaces [77-79]. Nano-sized channels were created using electron beam lithography. Channels with different widths, a range of 50, 100, 200, 400, and 600 nm, were investigated. Data indicated no U-turns of actin filaments occurred in channels smaller than 500 nm in width. In addition, the channels were surrounded by PMMA sidewall, which prevented actin filaments escaping from the channels. Selective binding of HMM molecules on channel surfaces for motility was achieved by chemical vapor deposition of trimethylchlorosilane (TMCS), which was covalently bound to the SiO_2/Si surfaces and supportive of actin-myosin motility. As a result, channel surfaces exhibited high quality motility, while photoresist-covered area showed low quality motility, as shown in Figure 2.10. However, polarity of actin filaments remained improperly regulated.

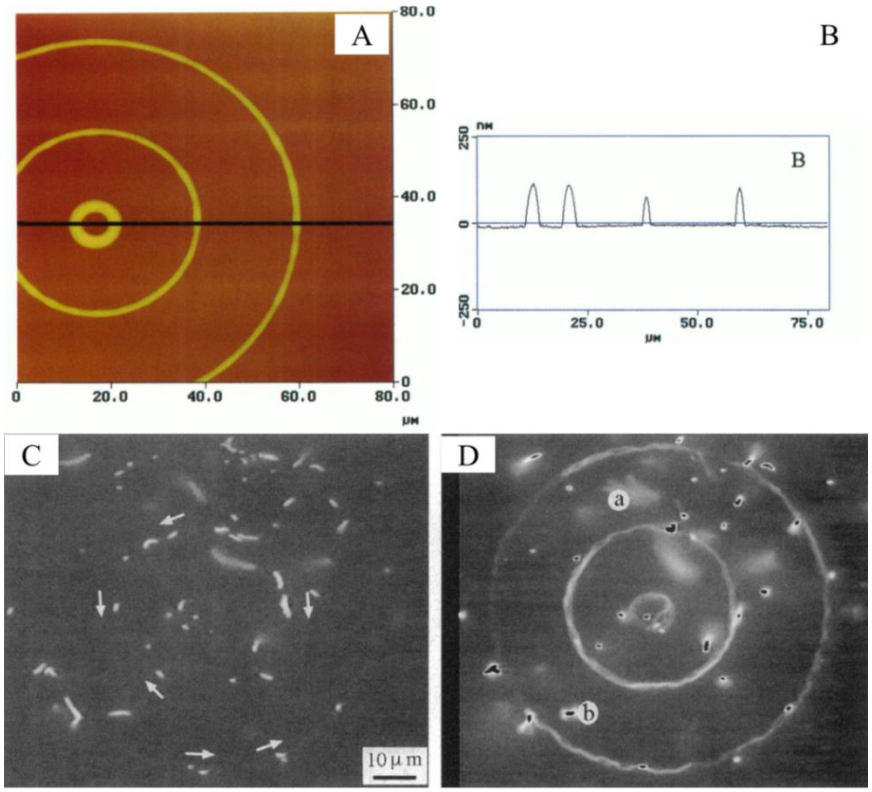

Figure 2.9 Actin sliding movement on the triple concentric circular PMMA tracks coated by HMM molecules [75]. (A) AFM image of the circular PMMA tracks on the glass substrate. The radii of the tracks were 5, 20, and 40 μm. (B) Cross section along the black line in A). It indicated that the width and the height of the tracks were 1–2 μm and 200 nm, respectively. (C) A fluorescent image of actin filaments on the PMMA tracks. The polarities of actin

filaments were not regulated, which resulted in the bidirectional movement of actin filaments on the tracks. D) Accumulated image of 256 fluorescent images. Traces of actin filaments were exactly matched with the PMMA tracks.

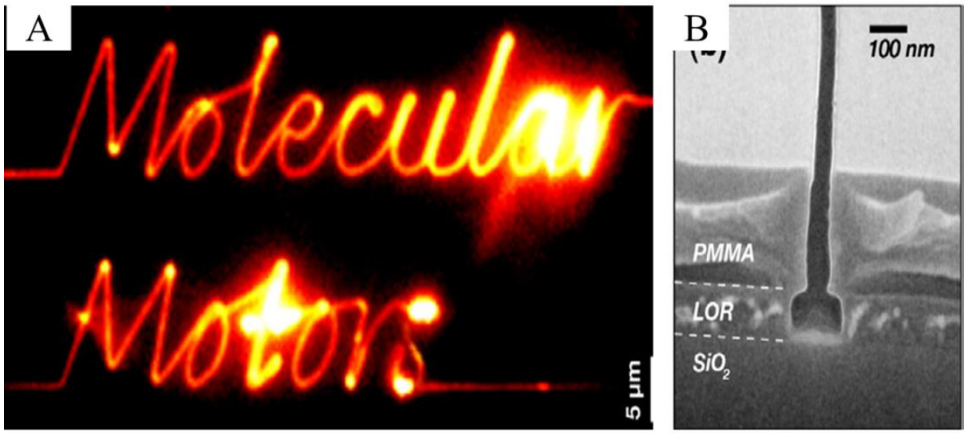

Figure 2.10 Actin sliding movements in nano-sized channels. (A) Accumulated image of fluorescent actin filaments moving on HMM molecule bound 200 nm wide channels. The channel structure did not allow U-turn of actin filaments. (B) SEM image showing the cross section of the fabricated channel [79].

In addition to confinement along linear tracks, some research groups utilized rectification patterns, which transform bidirectional movement into unidirectional movement. The utilization of rectification patterns is more suitable for kinesin-microtubule based motility. The flexibility of microtubules is lower than actin filaments, indicating that less complicated structures are required to confine the trajectory of microtubule movements. Y. Hiratsuka *et al.,* developed arrowhead patterns, which rectified microtubule movements. If a microtubule enters the arrowhead pattern from the correct direction, the microtubule passes through the arrowhead pattern. However, the microtubule entering the arrowhead pattern from the wrong direction makes a 180 ° turn to move along the correct direction. Hiratsuka's group demonstrated unidirectional rotational movement of microtubules along circular tracks and transport of microtubules between two pools connected by arrowhead patterns, as shown in Figure 2.11 [6]. Selective adsorption of kinesin on the tracks was performed as the system was constructed with two different layers. Sidewalls existed along the tracks such that microtubule movements were efficiently restricted inside the tracks.

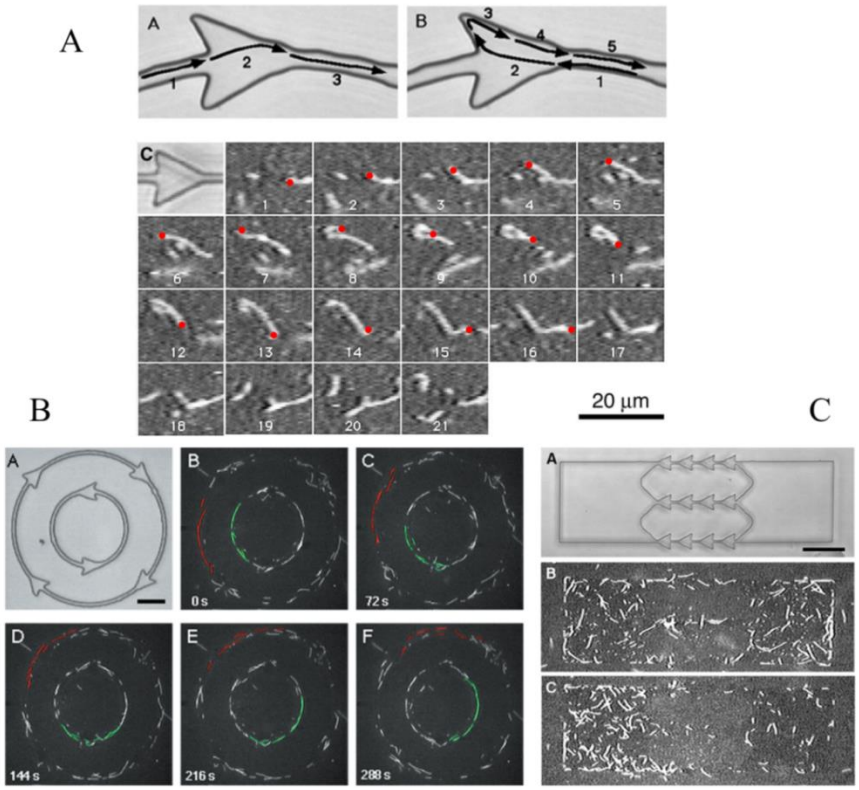

Figure 2.11 Controlling the direction of microtubule movements using rectification patterns. (A) An arrowhead pattern as a rectification pattern. The image showed how a microtubule entering from the wrong direction changes the direction to the correct direction in the arrowhead pattern. (B) Unidirectional movements of microtubule in circular tracks with arrowhead patterns. Microtubules on outer tracks showed clockwise-rotation while microtubules on inner tracks showed counter-clockwise rotation. (C) The transport of microtubules between two pools connected by arrowhead patterns. The population of microtubules in the right pool decreased as they shifted to the left pool [6].

Rectification patterns provide redirection, controlling the trajectory of motility movement. It is important to note that earlier systems using lithography including rectification patterns [6, 80-83] were designed so that the top of the channels were open to bulk solution. Such structures facilitate refreshing chemicals or materials required for experiments, but the attachment of filaments on the channels relied only on diffusion. As a result, the ability to control the quantity of filaments on the channels and their motion for long distances was not possible. Therefore, the development of enclosed microfluidic channels naturally followed [84, 85].

Huang's group fabricated a three-tier hierarchical structure with enclosed glass microchannels [85]. The system supported kinesin-microtubule based motility. Its structure also provided simple fluidic

connections for sample introduction and fluorescent imaging of microtubule movement. During etching of the glass substrate to make microchannels, Cr/Au layer was used as a mask along with photoresists in order to prevent photoresist lifting. The system was composed of rectifiers and a concentration ring, and was able to collect high densities of oriented microtubules, as shown in Figure 2.12.

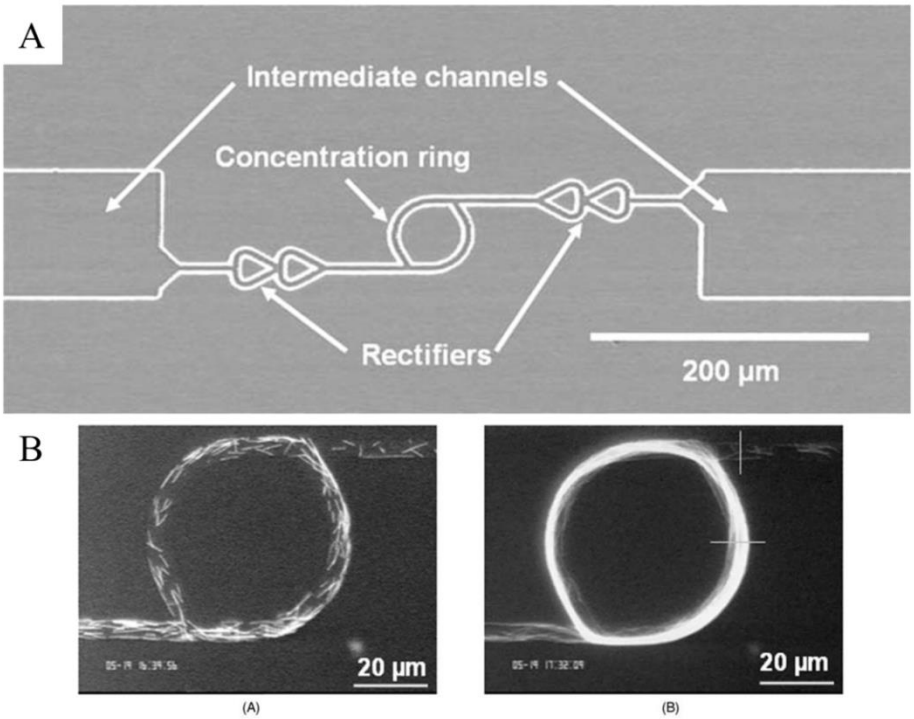

Figure 2.12 A 60 μm diameter circular ring to collect uniformly aligned microtubules. (A) SEM image of a microtubule storage ring. The microchannels were designed so that microtubules were collected in the concentration ring and traveled counterclockwise in the ring. (B) The movement of fluorescent microtubules in the ring. When microtubule solution was injected, microtubules moved in both directions. After 90 min of accumulation, the image showed that most microtubules moved counterclockwise in the ring [85].

The development of enclosed microfluidic channels allows combinations with localized applications in a more efficient way. One of most successful experiments is M. van den Heuvel's work which demonstrated molecular sorting of microtubules using DC electric fields, as shown in Figure 2.13 [86]. When DC electric fields were applied perpendicular to the direction of microtubule motion on kinesion-coated surfaces, the negatively charged microtubules gradually changed course and moved toward the positive electrode. Using this phenomenon, Heuvel's group successfully steered individual microtubules into desired channels. The group fabricated enclosed submicron microfluidic channels with a Y junction.

A perpendicular cross-channel existed at the Y junction. Ends of the cross-channel connected to reservoirs where platinum electrodes were inserted. When individual microtubules entered the Y junction from the central channel, the electric force was used to selectively steer them into the right or the left channel.

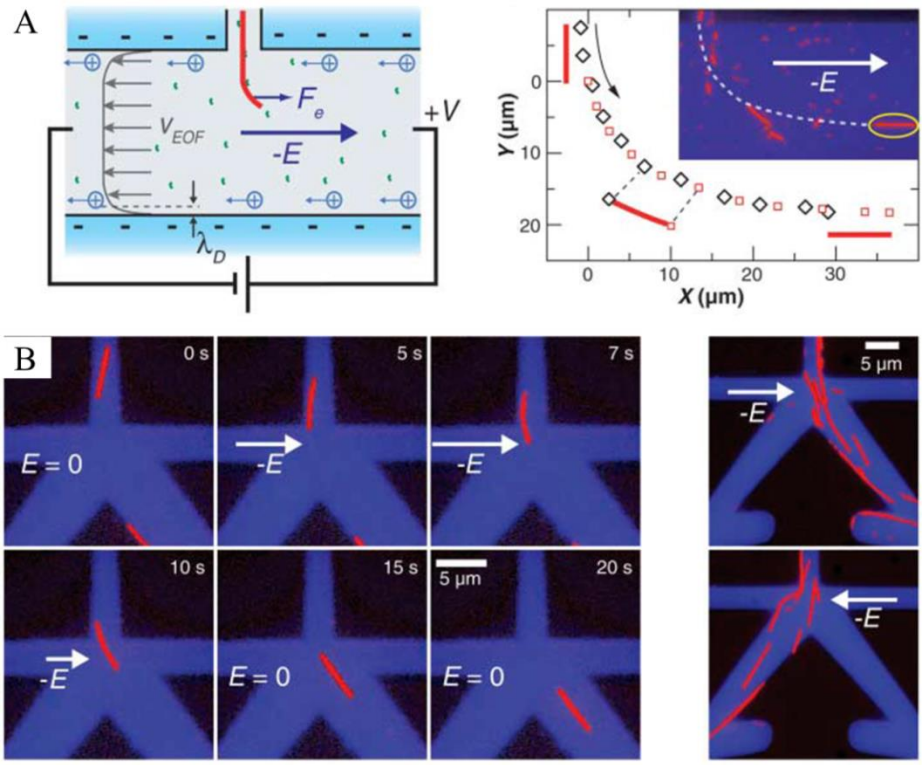

Figure 2.13 Electrical steering of individual microtubules in enclosed microfluidic channels. (A) A perpendicular electric field to the gliding microtubule on kinesin-coated surface. The direction of microtubule motion was gradually changed and moved toward the positive electrode. (B) Demonstration of molecular sorting of microtubules. The electric field was used to selectively steer individual microtubules into a desired channel at the Y junction [86].

2.6.2 Driven flow

R. Stracke *et al.*, (2000) demonstrated large-scale isopolar alignment of gliding microtubules on kinesin-coated surfaces by means of mechanically induced flow fields. A flow field forced the tip of a microtubule (which otherwise randomly moved on kiensin-coated surfaces) to turn in the flow direction. As a result, the whole microtubule moved along the flow direction.

The alignment of gliding microtubules was dependent on the mean velocity of the flow field. As the mean velocity of the flow field increased, the number of microtubules gliding along the flow direction increased, and all microtubules moved in the flow direction at 60 mm/s of the flow field, as shown in Figure 2.14. However, the gliding velocity of microtubules in the flow field was the same as the velocity in the absence of the flow field.

In Stracke's study, the flow field forced microtubules to glide along the flow field. The directional movement of microtubules returned to random movement after removing the flow field [5].

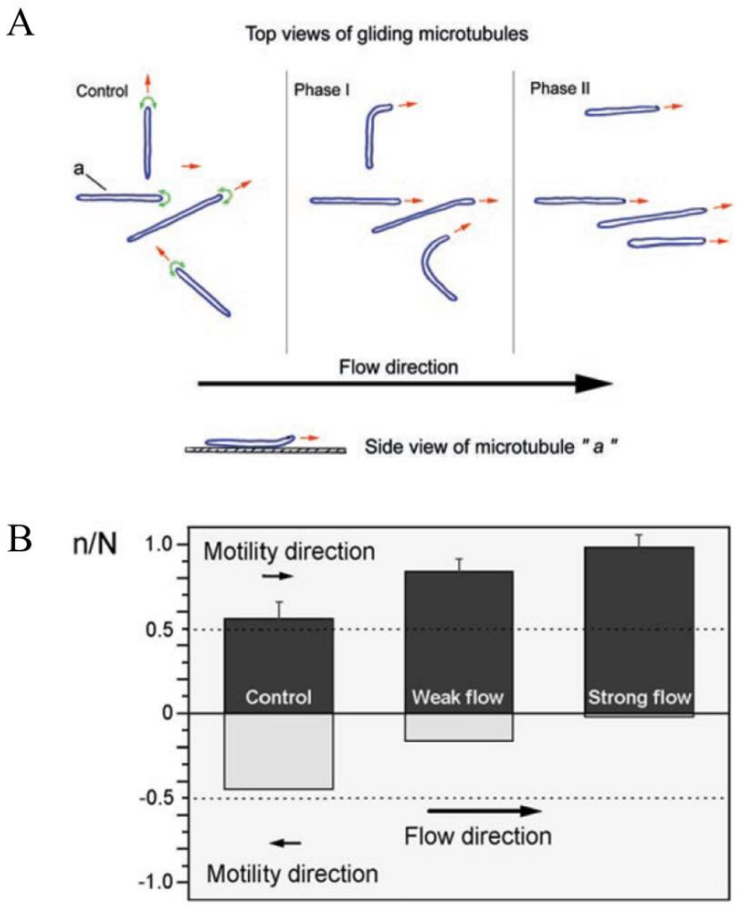

Figure 2.14 Flow-induced orientation of gliding microtubules. (A) Proposed mechanism illustrating how microtubules move along flow field direction. The tips of microtubules turn toward the flow direction. As a result, microtubules move along the flow direction. (B) The relative number (n/N) of gliding microtubules in the flow field. The diagram shows the alignment of gliding microtubules is proportional to the mean velocity of the flow field.

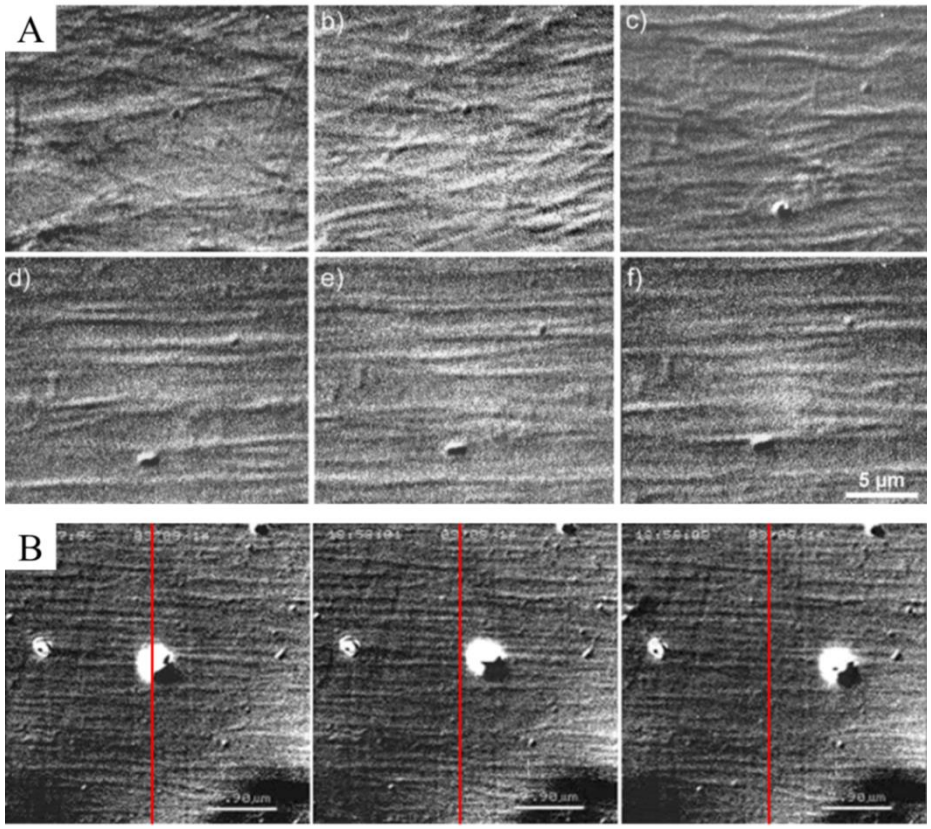

Figure 2.15 The unidirectional transport of kinesin-coated particles on flow-induced isopolar microtubule arrays. (A) Flow-induced isopolar microtubule arrays. Microtubules gliding on kinesin-coated surface were gradually aligned in flow direction. Once aligned, glutaraldehyde was introduced in order to maintain the alignment of microtubules under flow-free conditions. (B) The transport of kinesin-coated particles on microtubule arrays [87].

It is necessary to maintain the isopolar alignment of microtubules under flow-free conditions in order to utilize aligned microtubules as stable tracks for kinesin-driven transport to the desired destination. K. J. Bohm *et al.*, solved the issue and demonstrated unidirectional transport of kinesin-coated particles on the isopolar microtubule arrays. Turner *et al.*, found that glutaraldehyde-treated microtubules support kinesin motility without significant loss of activity [88]. Based on this finding, kinesin molecules were chemically inactivated using 0.1% of glutaraldehyde in phosphate-buffered saline, after which all microtubules oriented and moved along the flow direction. As a result, stable isopolar microtubule arrays were formed on kinesin-coated surfaces.

Since the leading end of gliding microtubules on kinesin-coated surfaces is a minus end, all minus ends of microtubules in the arrays should head toward the flow direction. On the arrays, kinesin-coated

particles showed the unidirectional movement toward the opposite direction of the flow in the presence of ATP, as shown in Figure 2.15. Thus, the movement of kinesin-coated particles proved the polarity of the arrays [87, 89].

2.6.3 Electric fields

When pH > pI, a protein has net negative charge, and the suspended protein in the medium moves toward the positive electrode in the presence of a DC electric field. This phenomenon is called electrophoresis. The electrical force can also have an effect on the gliding motion of filaments including actin filaments and microtubules.

M. van den Heuvel's group demonstrated the electrophoretic motion of suspending microtubules in buffer solution, as well as changing the course of microtubule movement gliding on the kinesin-coated surfaces using the DC electric field [86].

For actin-myosin, D. Riveline *et al.* controlled the direction of gliding actin filaments on myosin-coated surfaces, applying a DC electric field [3]. The actin-myosin motility was performed in the observation cell, where the motion of actin filaments was observed either on a flat surface or a patterned grating of 1 μm wide grooves using PMMA. Two separated reservoirs filled with buffer solutions were connected through the observation cell whose edge was sealed with 1% agarose in buffer solutions to prevent buffer drift and loss of actin filaments in the cell. By applying the DC electric field through platinum electrodes inserted in two reservoirs, the motion of actin filaments gliding across myosin-coated surfaces was altered. Actin filaments which were previously gliding in a random manner started to show visible orientation in the electric field of around 5×10^2 V/m. D. Riveline *et al.* demonstrated that actin filaments oriented and moved toward the positive electrode in higher electric fields. During actin-myosin motility along grooves which prevent U-turn of actin filaments, the velocity of actin filaments increased or decreased depending on filament motion direction with respect to the field direction. For instance, the velocity of actin filaments which moved toward the positive electrode was increased in the presence of the electric field, while the velocity of actin filaments which moved in the opposite direction was decreased, as shown in Figure 2.16.

However, the successful demonstration of filament motion control utilizing DC electric fields poses several associated problems. DC electric fields can generate heat and produce electrolysis causing bubbles and pH changes, especially in buffer solutions. The temperature rise and chemical reactions easily cause damage to proteins, suppressing their normal functions. The damage becomes more severe when scaled down.

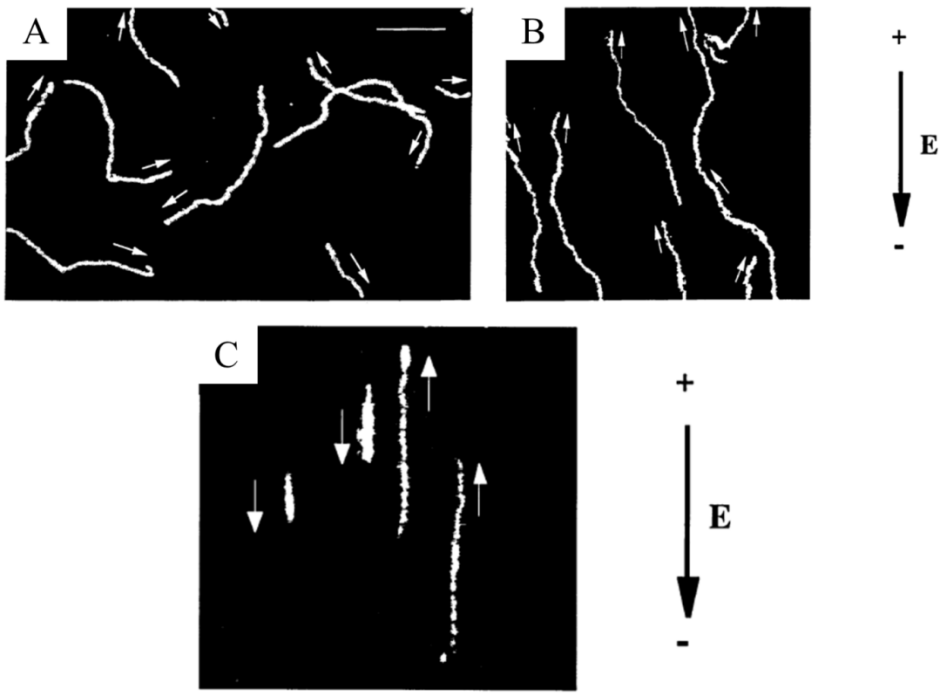

Figure 2.16 The motion of actin filaments on myosin-coated surfaces under DC electric fields. (A) The motion of gliding actin filaments on a flat surface in the absence of an electric field. Actin filaments randomly moved across myosin-coated surface. (B) The motion of gliding actin filaments on the flat surface in the presence of the electric field. Actin filaments oriented and moved toward the positive electrode. (C) The motion of gliding actin filaments on grooves in the presence of an electric field. The grooves prevented U-turn of actin filaments. As a result, the velocity of actin filaments gliding toward the positive electrode increased while the velocity of actin filaments gliding in the opposite direction decreased [3].

An AC electric field can replace the DC electric field to manipulate motility motion. When particles are subjected to a non-uniform electric field, a dipole moment is induced, causing a response to the electric field. Under the AC electric field, particles endure dielectrophoretic (DEP) force. This force moves particles to a high or low electric field, depending on particle polarizability, as compared to the surrounding medium, which is termed positive and negative DEP, respectively [90]. In addition, particles experience electro-orientation (EO), which affects the alignment of a dipole along the field [91].

S. B. Askoan's group investigated the influence of AC electric fields on actin-myosin motility. In the experiments, actin filaments were suspended in a medium with positive DEP from 100 kHz to 30 MHz.

Experiment findings were consistent with simulation data indicating positive DEP of actin filaments up to 100 MHz. Actin filaments suffering positive DEP were attracted to a high electric field region, the edges of electrodes. The torque by EO can force the longest axis of rod-shaped particles like actin filaments to align with the electric field. In the presence of AC electric fields, actin filaments gliding across myosin-coated surfaces between electrodes showed aligned movement along the electric fields because of the torque by EO, as shown in Figure 2.17 [4]. Such aligned movement was proportional to the strength of applied electric fields. Although AC electric fields oriented the motion of actin filaments, no regulation in the polarity of actin filaments occurred. As a result, aligned actin filaments between electrodes showed bidirectional movement, which was perpendicular to electrodes. In addition, high electric fields were required to demonstrate significant oriented movement.

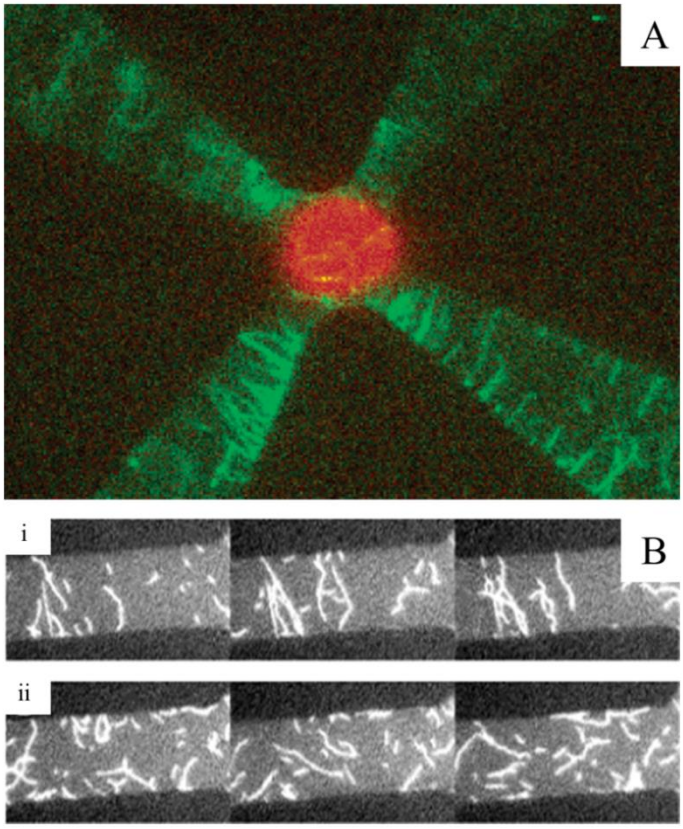

Figure 2.17 Actin-myosin under AC electric fields. (A) Dielectrophoretic forces on actin filaments. In the presence of AC electric fields, actin filaments were attracted to a high electric field region (positive DEP), while beads were collected in a low electric field region (negative DEP). (B) Torque by electro-orientation on actin filaments. Random movement of actin filaments on myosin-coated surfaces changed to aligned movement perpendicular to electrodes in the presence of AC electric fields [79].

2.6.4 Biological approaches

Cytoskeletal filaments, actin filaments and microtubules, have a structural polarity. Motor proteins recognize this polarity and move along filaments toward the plus or minus end. For example, kinesin and myosin II moves along filaments toward the plus end, while myosin VI moves in the opposite direction.

Controlling the polarity of filaments is a key in realizing directional transport. Actin-capping proteins, capping either the plus or minus end of filaments, exist in cells to promote the depolymerization of filaments or to stabilize filaments in cytoskeletal structures. Using such proteins, it is possible to control the polarity of filaments and create unipolar tracks. These tracks are analogous to cytoskeletal pathways in cells. The tracks can carry out the unidirectional transport of motor protein-coated particles.

The first successful creation of unipolar filament tracks was reported by J. A. Spudich's group in 1985 [7]. The polarity of actin filaments was controlled using severin, which capped the plus end of actin filaments. Using biotinlyated severin, the plus end of actin filaments was bound to the avidin-coated surface. In the presence of proper flow fields, actin filaments lay down on the surface with the minus end toward the downstream direction, as shown in Figure 2.18. Myosin-coated particles moved on the actin array, showing unidirectional movement. The direction of the movement was in the upstream direction, which confirmed the polarity of the actin array.

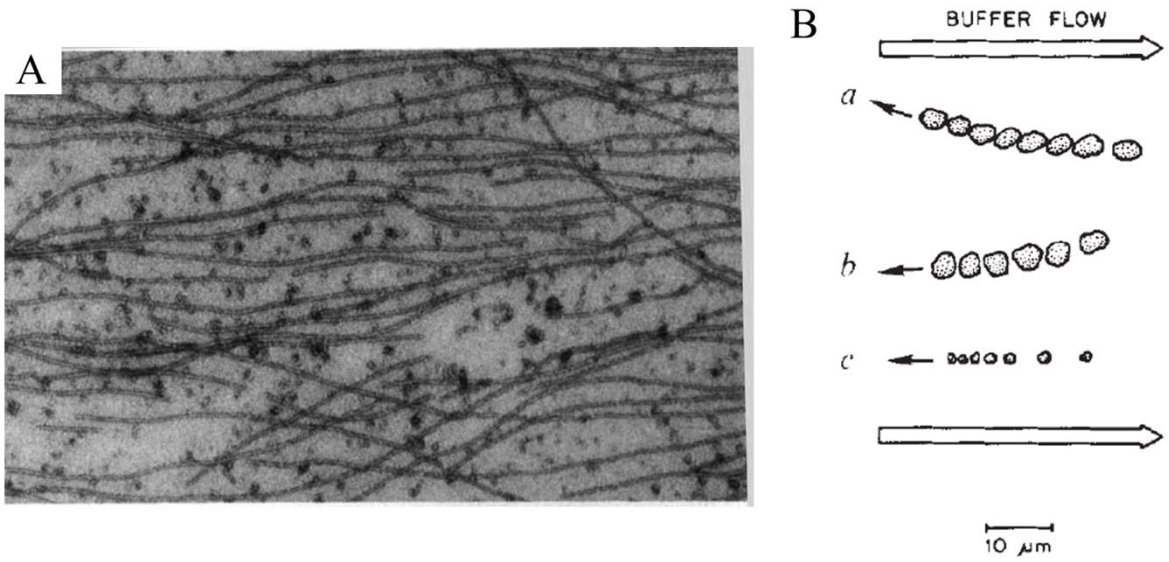

Figure 2.18 Unipolar actin array using biological approaches. (A) A TEM image of the actin array. The plus end of actin filaments was fixed on the avidin-coated surface using biotinylated severin. The actin filaments were oriented along the flow field with the minus end of actin filaments toward the downstream direction with respect to the flow.

(B) Movement of myosin-coated particles. Myosin-coated particles showed the directional movement toward the upstream direction, which proved the polarity of the actin array [7].

2.6.5 Summary

Previous reported methods of controlling direction of motility movement were reviewed in the aspect of advantages and limitations. Engineered tracks do not allow U-turn of gliding filaments in submicron channels, which causes unidirectional motion in channels. Specific geometric patterns like arrowhead patterns act as mechanical rectifiers to correct the direction of gliding filaments. However, the motion of gliding filaments in engineered tracks depends on Brownian motion. As a result, directional control of motility is difficult. Electric fields enable directional control of motility. Negatively charged filaments respond to DC electric fields and move toward the positive electrode. In addition, gliding motions of rod-shaped filaments are oriented along AC electric fields by the torque generated by EO. However, DC electric fields usually generate heat and electrolysis in solutions, which can damage on proteins, and the aligned movement of filaments under AC electric fields is bidirectional movement. Review of the scientific literature indicates inferior result on the directional control of actin-myosin based motility as compared to kinesin-microtubule based motility. J. A. Spudich's group [7] is the only one who demonstrated the directional control of actin-myosin in nanoscale. However, even the study done by his group has several critical problems. Most myosin-coated particles binding to oriented actin arrays did not move. Few particles moved short distances [56], although unidirectional transport of myosin-coated particles was demonstrated in natural actin cables [55]. This may imply that poor transport of myosin-coated particles on the actin arrays is due to incomplete orientation of the arrays. A continuous flow field had to be present during the assay in order to maintain the alignment of the arrays. Reinvestigation of the methodology introduced by J. A. Spudich's group is required to improve protocols and the directional transport of actin-myosin based motility.

CHAPTER 3 – EXPERIMENTAL METHODS

This chapter presents experimental methods including microscopy and recording system, the process of protein purification including actin and myosin II, preparation of solutions, the process of biotinylation, data analysis methods, and protocols used for experiments.

3.1 Microscopy and recording system

Small materials such as proteins are often too tiny to be observed using conventional optical microscopes. When various small materials are mixed, they are even more difficult to be distinguished. For such cases, fluorescent dyes serve as markers to visualize the location or pattern of such small materials. Generally, the fluorescence microscope provides the observation of biological molecules stained with fluorescent dyes. Figure 3.1 shows an illustration of microscopy and recording system. The observed scenes by the fluorescence microscope are captured and converted into digital images by CCD camera and the digital images are recorded onto a computer.

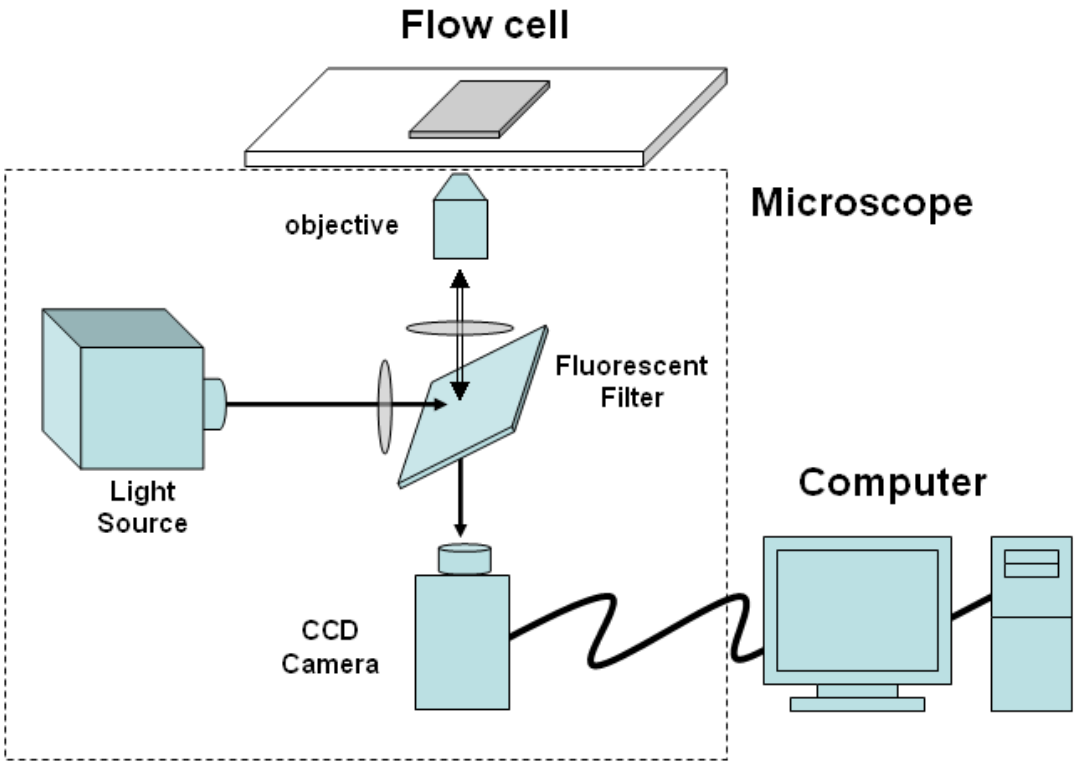

Figure 3.1 The illustration of microscopy and recording system. The location or pattern of fluorescent-dyed molecules is observed by a fluorescence microscope. The scenes are captured by CCD camera and recorded onto a computer.

3.1.1 Fluorescence microscopy

A Nikon Eclipse TE-200 inverted fluorescence microscope was used to observe fluorescent-dyed biomolecules including actin filaments and streptavidin molecules. In fluorescence microscopy, fluorescent objects are observed only when they fluoresce by excitation of light of a specific wavelength. Usually, the wavelength of fluorescing light is longer than the wavelength of light that excites the molecules. Any unnecessary external light source has to be off in the course of operating the microscope because it interferes with observation of fluorescence by passing through the objectives. Following description shows how to observe fluorescent objects through the microscope. The multispectral light source from a lamp house is illuminated toward a fluorescent filter. The fluorescent filter consists of an excitation filter, a dichromatic beamsplitter and an emission filter. First, illuminated multispectral light is filtered through the excitation filter according to a desired wavelength such as ultraviolet, blue or green in the fluorescent filter. Filtered light is reflected by a dichromatic beamsplitter toward the microscope objective or the specimen. The dichromatic beamsplitter is a specialized interference filter that reflects longer wavelength lights while shorter wavelength lights pass through it. It is titled at 45 °with respect to incoming light from the excitation filter, so that it reflects the light from the excitation filter toward the microscope objective. When a light reaches fluorescent objects in the specimen through the microscope objective, the fluorescent objects start to fluoresce with a specific wavelength. The fluorescent light is gathered by the objective and passes back to the fluorescent filter. As the light passes through the emission filter, undesired light is filtered. The light filtered by the emission filter passes through the dichromatic beamsplitter toward the observation system without reflection.

Three fluorescent filters and four microscope objectives are equipped in the microscope and the specifications of them are described in Table 3.1 and 3.2.

Model	**Wavelengths of excitation filter (nm)**	**Cut-on wavelength of dichromatic mirror (nm)**	**Wavelengths of emission filter (nm)**
UV-2E/C	340-380nm	400nm	435-485nm

B-2E/C	465-495nm	505nm	515-555nm
G-2E/C	528-553nm	565nm	590-650nm

Table 3.1 Specification of fluorescent filters

Manufacture	**Optical correction**	**Magnification and Numerical Aperture**	**Specialized Optical Properties**	**Tube Length & Cover glass thickness**	**Working Distance (mm)**
Nikon		10x/0.25	Ph1 ADL	∞/1.2	5.2
Nikon	Plan Fluor	ELWD 40x/0.60	Ph2 DM	∞/0-2	3.7-2.7
Nikon	Plan Apo	60x/1.40 oil	DIC H	∞/0.17	0.21
Nikon	Plan Fluor	100x/1.30 oil	DIC H	∞/0.17	0.20

Table 3.2 Specification of fluorescent filters

In experiments, actin filaments are labeled with a red-orange fluorescent dye, tetramethylrhodamine (TRITC, excitation/emission: 540/565 nm). As a result, 60/100× objectives and G-2E/C fluorescent filter are used to observe actin filaments. Streptavidin molecules (Thermo Fisher Scientific Inc.) are labeled with DyLight 488 fluor (excitation/emission: 493/518 nm), which is similar to fluorescein isothiocyanate (FITC). For the observation of streptavidin patterns on surfaces, 10/40/60/100× objectives and B-2E/C fluorescent filter are used. When actin filaments and streptavidin molecules exist in the same scene, the observation of actin filaments and streptavidin molecules is not interfered because dyes conjugating to them have different excitation/emission wavelengths. Immersion oil serves to help high resolution of microscope in use of 60/100× objectives.

ORCA-AG deep cooled digital camera (C4742-80-12AG, Hamamatsu) is equipped to capture scenes observed by the fluorescence microscope, as shown in Figure 3.2. It communicates with the computer

through IEEE 1394 interface, and it is remotely controlled by software, called Wasabi (Hamamatsu). It provides 12-bit images, and is capable of a maximum 1344 × 1024 pixel resolution. For the maximum resolution, the pixel size is 64.5 × 64.5 nm, and the maximum frame per second (fps) is 8.8 without noise reduction function. When 2 × 2, 4 × 4, and 8 × 8 binning is applied, the maximum fps can be 16, 27, and 4

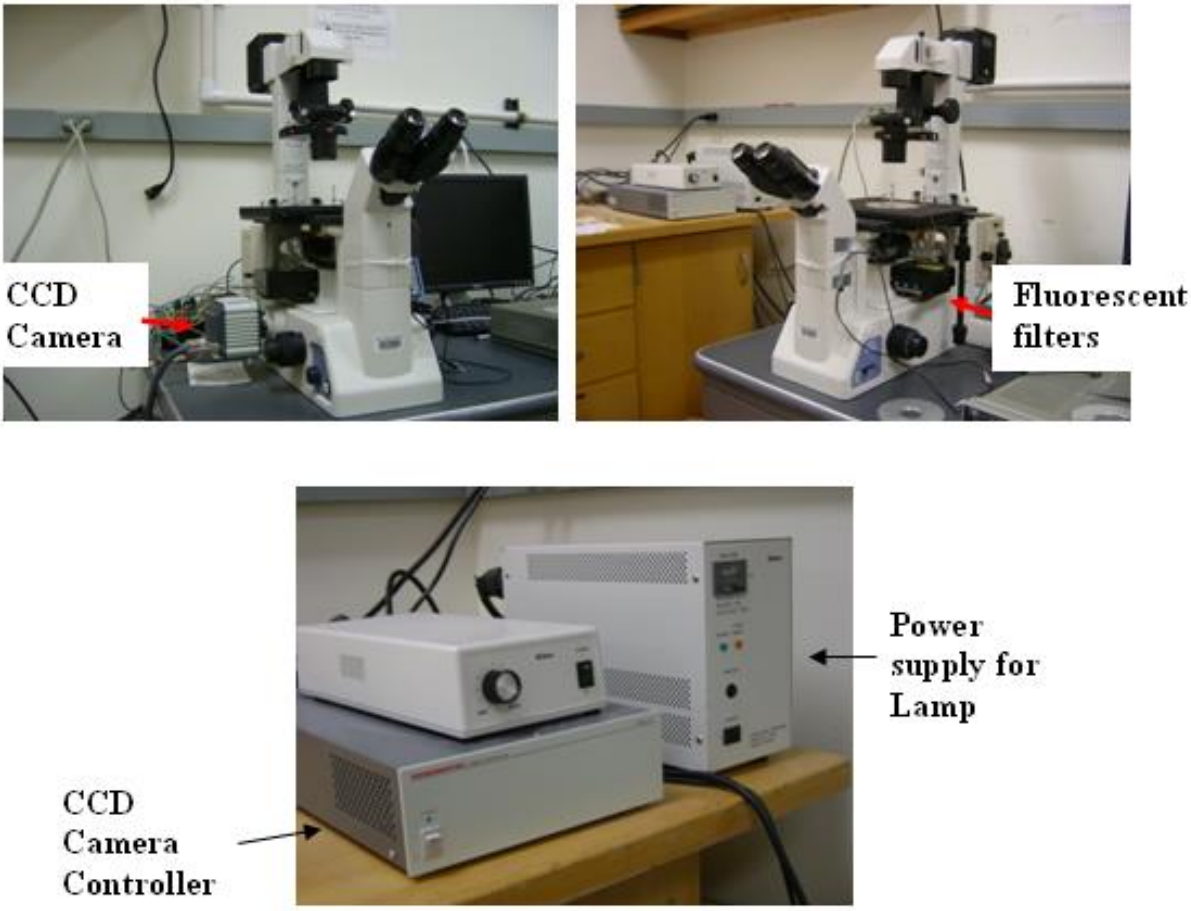

Figure 3.2 A Nikon Eclipse TE-200 inverted fluorescence microscope. The microscope is equipped with ORCA-AG deep cooled digital camera.

3.1.2 Recording System

Fluorescence images obtained from the CCD camera are displayed on a 17" LCD monitor and controlled by Wasabi software, as shown in Figure 3.3. The software provides interfaces not only to control the parameters of the CCD camera like exposure times, frame rates and screen sizes but also save captured image data as pictures or image sequences in real time. Image sequences can be converted to

AVI video files and played by other AVI video players. Usually, the image size of our experiments is 1344 × 1024 pixel at 8.8 fps. Frame rates can increase as reducing the image size. AVI video files are edited by VirtualDub, After Effects 6.5, and ImageJ. Images are edited by ImageJ and IrFanView, and image analysis is performed using ImageJ and Matlab.

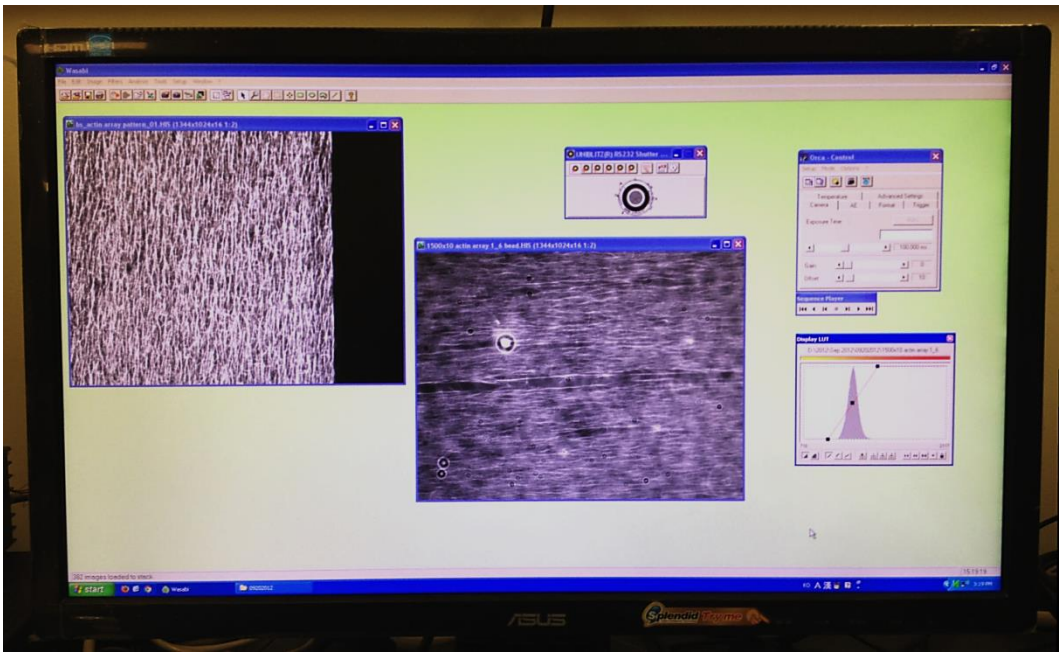

Figure 3.3 Wasabi program for image acquisition and analysis.

3.2 Preparation of Actin

3.2.1 Purification of actin filaments

The purification of actin filaments is performed in Dr. Peter M. Gannett's research lab at the School of Pharmacy at WVU. Actin is obtained from a rabbit muscle acetone powder (Pel-freez Arkansas, LLC) by repeated filtration and ultracentrifugation [92]. The concentration of purified F-actin was determined using specrophotometry at 290 nm wavelength (BioMate 3, Thermo electron Corp.) using the extinction coefficient of 0.633 mL/mg/cm or 26,600 $M^{-1}cm^{-1}$. The process flow of the purification is described below.

The process flow of purification of F-actin

1. Weigh and grind rabbit muscle acetone powder (ca. 1 g) at room temperature for 10 min.

2. Mix with cold extracting buffer (ca. 20 mL/g-acetone powder) in a conical tube, and gently stir on ice for 30 min. The extractin buffer consists of 2 mM Tris-HCl, 0.2 mM ATP, 0.2 mM $CaCl_2$, 0.5 mM DTT and 1 mM NaN_3 at pH 8.

3. Centrifuge it in Sorvall legend RT at 4,000 rpm for 10 min at 4 ℃. It will bring the separation of a solution containing G-actin (supernatant) from the muscle residue (pellet).

4. Decant the supernatant (supernatant #1) into an empty conical tube, and keep it on ice.

5. Resuspend the pellet collected in Step 3 in the same volume used in Step 2 of cold extracting buffer (ca. 20 mL), and gently stir on ice for 30 min.

6. Centrifuge it in Sorvall legend RT at 4,000 rpm for 10 min at 4 ℃.

7. Decant the supernatant (supernatant #2) into the tube containing supernatant #1 in Step 4.

8. Centrifuge the combined supernatant in Step 7 in Sorvall legend RT at 4,000 rpm for 10 min at 4 ℃ to clarify it.

9. Decant the supernatant in Step 8 into an ultra-centrifuge container, and centrifuge it in Beckmann 70.1 Ti rotor at 40,000 rpm for 30 min at 4 ℃ to clarify it again.

10. Decant the supernatant in Step 9 into an empty conical tube, and add 3M KCl to a final concentration of 50 mM KCl, 1M $MgCl_2$ to a final concentration of 2 mM $MgCl_2$, and 1 M ATP to a final concentration of 1 mM ATP. Let G-actin polymerize into F-actin on ice for 1 hour with gentle stirring.

11. Slowly add solid KCl with gentle stirring to give a final concentration of 0.8 M. High salt will remove tropomyosin binding to F-actin. Continuously stir on ice for 30 min.

12. Centrifuge it in Beckmann 70.1 Ti rotor at 45,000 rpm for 1.5 h at 4 ℃.

13. Carefully discard the supernatant. A gelatinous pellet should be found on the bottom of the ultra-centrifuge container. The pellet is F-actin.

14. Carefully add 1 mL of cold extracting buffer to gently rinse F-actin pellet. After the rinse, the solution is pipetted off.

15. Resuspend the F-actin by gentle homogenization in cold extracting buffer (ca. 3 mL/g-acetone powder).

16. Dialyze against the extracting buffer (ca. 500 mL) for overnight at 4 ℃.

17. Add 3M KCl to a final concentration of 50 mM KCl, 1M $MgCl_2$ to a final concentration of 2 mM $MgCl_2$, 1 M ATP to a final concentration of 1 mM ATP and 1 M NaN_3 to a final concentration of 4 mM NaN_3. It will make G-actin polymerize into F-actin.

18. Measure the concentration of purified F-actin using the spectrophotometer, and dilute F-actin to be desired concentrations (ca. 0.25 mg/mL of F-actin).

3.2.2 Labeling of F-actin

Labeling process with fluorescent dyes is necessary to observe F-actin. As mentioned earlier, phalloidin is the actin binding protein and forms conjugates with other proteins or chemicals to perform specific functions. In this study, rhodamine-phalloidin (R415, Invitrogen or P1951, Sigma-Aldrich) is used to label F-actin. Rhodamine, a fluorescent dye, allows observation of F-actin by the formation of rhodamine-phalloidin conjugates under a fluorescence microscope. Rhodamine-phalloidin was dissolved in methanol, and the solvent was evaporated immediately before use. 0.25 mg/mL of F-actin was labeled with rhodamine-phalloidin with a molar ratio of 1:1 in M-buffer for 12 h.

3.3 Preparation of skeletal myosin II

The purification of skeletal myosin II is performed in Dr. Peter M. Gannett's research lab at the School of Pharmacy at WVU. Freshly frozen rabbit muscle tissues were obtained from Pel-freez Arkansas, LLC, and the purification of myosin are prepared according to a published procedure with modification [51]. The concentration of purified myosin was determined using the Bradford protein assay (23236, Thermo Fisher Scientific Inc.). The process flow of the purification is briefly described below.

The process flow of purification of skeletal myosin II

1. Prepare freshly frozen rabbit muscle tissues. Thaw it partially, and cut into small pieces (**ca. 2 cm^3-size cubes**) on foil.

2. Mince the muscle tissues twice in meat grinder, and collect them (**ca. 50 g**) on a beaker as shown Figure 3.4. Use the fine mesh at least for the second mincing.

Figure 3.4 Ground rabbit muscle tissues.

3. Mix with 3 vol. of cold myosin extracting buffer (**ca. 150 mL / 50 g-rabbit muscle**) in beaker on ice as shown in Figure 3.5, and gently stir for exactly 10 min, which is to minimize actin extraction. The myosin extracting buffer contains 0.3 M KCl, 0.1 M KH_2PO_4, 0.05 M K_2HPO_4, 20 mM EDTA, and 1 mM DTT at pH 6.7

Figure 3.5 Extract skeletal myosin molecules from ground rabbit muscle tissues.

4. Centrifuge it in Sorvall legend RT at 3,000 rpm for 10 min at 4 ℃. 4 of 50 mL conical tubes will be necessary.

5. Decant the supernatants into an empty conical tube, and keep them (**ca. 100 mL**) on ice. Pellets can be used for actin purification.

6. Slowly add 14 vol. of cold water (**ca. 1,400 mL**) while gently stirring. It will give a final ionic strength of approx. 30 mM where myosin molecules are polymerized as shown in Figure 3.6. Gently stir for 1 h in cold room.

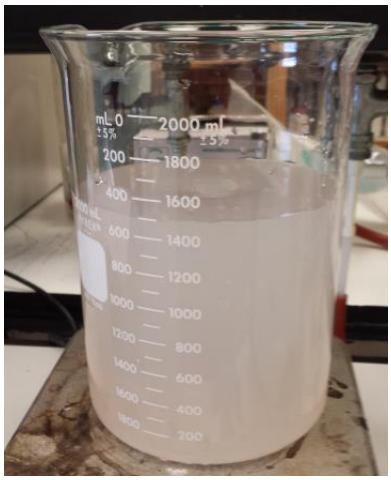

Figure 3.6 White turbidity caused by the polymerization of myosin.

7. Centrifuge it in Sorvall legend RT at 3,000 rpm for 10 min at 4 ℃. 30 of 50 mL conical tubes will be necessary.

8. Carefully discard the supernatants from each tube. A gelatinous pellet should be found on the bottom of the conical tube as shown Figure 3.7. The pellet contains polymerized myosin.

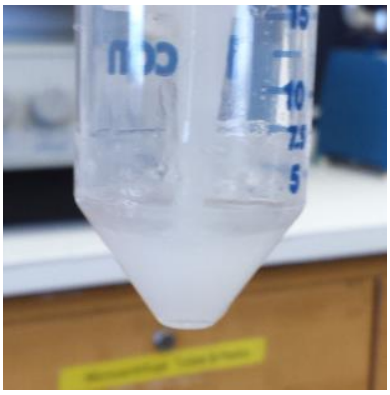

Figure 3.7 A white pellet containing polymerized myosin.

9. Add minimum amount (**ca. 30 mL**) of cold high salt buffer A (0.5 M KCl, 10 mM KPO_4, 5 mM EDTA and 1 mM DTT at pH 6.7) into each tube to resuspend the pellets. Collect all pellets (**ca. 65.5 mL**) and add 3 M KCl (**ca. 6.5 mL**) to give a final ionic strength of 0.5 M. Polymerized myosin is soluble in high ionic strength.

10. Add 0.67 vol. of cold water (**ca. 48 mL**) to give a final ionic strength of 0.3 M while stirring as shown in Figure 3.8. It will precipitate the actomyosin. Be careful not to lower the ionic strength below 0.3 M, which will precipitate myosin as well. Gently stir for 40 min on ice.

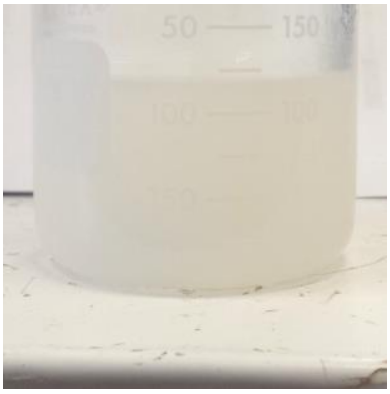

Figure 3.8 Depolymerization of myosin. The ionic strength of 0.3 M will precipitate the actomyosin while myosin is soluble.

11. Centrifuge the solution in Step 10 in Beckmann 70.1 Ti rotor at 23,000 rpm for 1 h at 4 ℃.

12. Decant the supernatants into an empty conical tube, and keep them (**ca. 100 mL**) on ice.

13. Slowly add 6.5 vol. of cold water (**ca. 650 mL**) as shown if Figure 3.9. It will give a final ionic strength of 40 mM. Let myosin polymerize for 10 min in cold room.

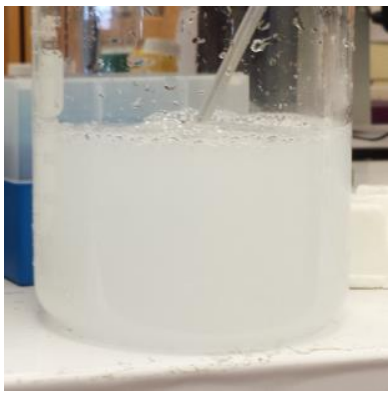

Figure 3.9 Polymerization of myosin. The ionic strength of 40 mM will cause the polymerization of myosin molecules.

14. Centrifuge it in Sorvall legend RT at 4,000 rpm for 10 min at 4 ℃.

15. Carefully discard the supernatants. A gelatinous pellet should be found on the bottom of the conical tube as shown Figure 3.10. The pellet is polymerized myosin.

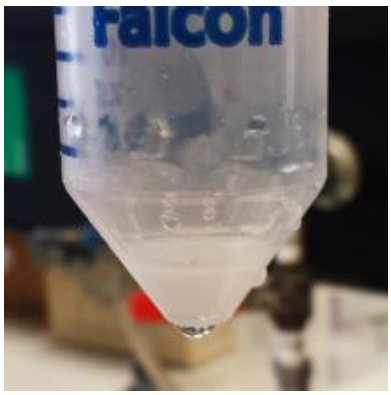

Figure 3.10 A white pellet of polymerized myosin.

16. Add minimum amount (**ca. 5 mL**) of cold high salt buffer B (0.5 M KCl and 10 mM KPO_4 at pH 6.7) into each tube to resuspend the pellets. Collect all pellets (**ca. 20 mL**) and add 3 M KCl (**ca. 2.76 mL**) to give a final ionic strength of 0.5 M. Polymerized myosin is soluble in high ionic strength as shown in Figure 3.11.

Figure 3.11 Second depolymerization of myosin. Myosin is soluble in the high ionic strength.

17. Centrifuge the solution in Step 16 in Beckmann 70.1 Ti rotor at 30,000 rpm for 1 h at 4 ℃.

18. Decant the supernatant into an empty conical tube, and keep them (**ca. 20 mL**) on ice. The supernatant is purified full-length of myosin. It will be 10 – 20 mg/mL of 20 mL per 50 g rabbit skeletal muscle. It can be stored with 50% glycerol at –20 ℃ and must not be frozen.

The process flow for the preparation of heavy meromyosin (HMM)

1. Prepare freshly purified skeletal myosin II (ca. **10 – 20 mg/mL of 20 mL**) in 0.5 M KCl and 10 mM KPO_4 at pH 6.7. Add 0.001 vol. of 1 M DTT (ca. 20 μL) to give a final concentration of 1 mM DTT and 0.001 vol. of 1 M $MgCl_2$ (ca. 20 μL) to give a final concentration of 1 mM $MgCl_2$.

2. Add 0.05 vol. (**ca. 1 mL/20mL-myosin solution**) of 1 mg/mL α-chymotrypsin to give a final concentration of 0.05 mg/mL α-chymotrypsin, and gently stir for exactly 10 min at room temperature. The tail of the myosin molecule will be cleaved by α-chymotrypsin, which yields HMM. Also, carefully add α-chymotrypsin since the acidic solution may cause local precipitation and denaturation of myosin during adding.

3. Add 0.0025 vol. (**ca. 52.5 µL**) of 200 mM PMSF (phenylmethylsulfonyl fluoride) in anhydrous ethanol. It will give a final concentration of 0.5 mM PMSF and inactive α-chymotrypsin to stop the digestion of the myosin molecule.

4. Dialyze the solution of Step 3 in 1 L of HMM storage buffer (40 mM KCl, 5 mM KPO_4 and 1 mM DTT at pH 6.5) with several buffer changes for overnight at 4 ℃. The exchange to a low ionic strength will cause the polymerization of LMM (light meromyosin) and undigested myosin while HMM is soluble in the low ionic strength buffer as shown in Figure 3.12.

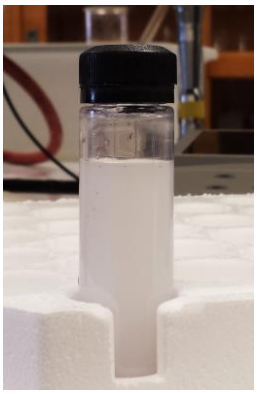

Figure 3.12 Second polymerization of myosin. The solution becomes cloudy because of the polymerization of LMM and undigested myosin after dialysis.

5. Centrifuge the dialyzed solution in Step 4 in Beckmann 70.1 Ti rotor at 40,000 rpm for 1 h at 4 ℃.

6. Decant the supernatant into an empty conical tube, and keep them (**ca. 18 mL**) on ice. The pellet containing polymerized LMM and undigested myosin can be found on the bottom of the centrifuge container as shown in Figure 3.13. The supernatant is purified HMM, and it will be 4 – 9 mg/mL of 18 mL HMM. It can be stored with adding 50% glycerol and 1 mM EDTA at final concentration at –80 ℃ after quickly freezing by nitrogen liquid.

Figure 3.13 The pellet containing polymerized LMM and undigested myosin. The white pellet on the bottom of the centrifuge container is a mixture of polymerized LMM and undigested myosin.

3.4 Biotinylation of gelsolin

Gelsolin was purchased from Sigma-Aldrich Inc. (G8032, from bovine plasma) Biotinylation was executed using NHS-PEG_4-Biotin (Thermo Fisher Scientific Inc.) with the following conjugation protocol. Gelsolin was dialyzed against a crosslinking phosphate buffer (B-PBS buffer, 150 mM NaCl and 100 mM sodium phosphate at pH 7.2) for 12 h. NHS-PEG_4-Biotin was dissolved in deionized water immediately before use at a concentration of 2 mg/mL. The two solutions were mixed together with a molar ratio of 60:1 for 2 h on ice. Unattached biotins were removed by dialysis in a gelsolin storage buffer (75 mM NaCl, 20 mM Tris, 0.2 mM EGTA and 10 mM Imidazole at pH 7.4) for 12 h. Gelsolin concentration was measured using Bradford protein assay (Thermo Fisher Scientific Inc.) and biotinylated gelsolin was stored at -80 ℃ until use. The quantitation of biotin per gelsolin was performed using Pierce Biotin Quatitation Kit (28005, Thermo Fisher Scientific), and the result indicated approx. 1.4 biotin molecules per gelsolin molecule. The accuracy of the kit was low in the low concentration of biotinylated proteins, so a high concentration of biotinylated gelsolin was applied. Before measuring the quantity of biotin in biotinylated gelsolin, a control test was performed using biotinylated horseradish peroxidase at the same concentration.

Calculation of Moles of biotin per Mole of gelsolin

A_{500}_H\A: 1.082 (absorbance at 500 nm for reference)

A_{500}_H\A\Gelsolin: 0.951 (absorbance at 500 nm for sample)

Moles of gelsolin per mL = Gelsolin concentration/MW of gelsolin = (0.43 mg/mL)/(91,000 MW) = 4.725 μM

The change in absorbance at 500 nm (ΔA_{500}) = (0.9 × A_{500}_H\A) – (A_{500}_H\A\Gelsolin) = (0.9 × 1.082) – 0.951 = 0.0228

*{0.9 is a dilution factor for the dilution of the H\A mixture by the biotinylated gelsolin}

Moles of biotin per mL = ΔA_{500}/34,000 = 0.0228/34,000 = 0.6706 μM

*{34,000 is an extinction coefficient at 500 nm}

The quantity of biotin per gelsolin = (Moles of biotin × 10)/Molese of gelsolin = {(6.706 × 10^{-7}) × 10}/(4.725 × 10^{-6}) = 1.420

*{10 is a correction factor for the biotin concentration in the original biotinylated gelsolin}

3.5 Fabrication of streptavidin-coated surfaces

Cover slips (no.1, 18 × 18 mm, Corning) were sonicated in acetone and methanol solutions for 5 min, respectively. Dried cover slips using a N_2 gas gun were cleaned using Summa solution at 55 ℃ for 30 min. Cleaned cover slips were immersed for overnight in (3-Aminopropyl)triethoxysilane (APTES, Sigma-Aldrich Inc.) solution (5 % APTES in anhydrous ethanol). As a result, the primary amine groups were covalently formed on the cover slip that was confirmed using X–ray photoelectron spectroscopy (XPS, PHI 5000 VersaProbe X-Ray Photoelectron Spectroscopy). APTES-coated cover slips were rinsed with anhydrous ethanol before use. The APTES-coated surface was biotinylated with 2 h incubation of 2 mg/mL of NHS-PEG_4-biotin (Thermo Fisher Scientific Inc.) in dimethylformamide (DMF, Sigma-Aldrich Inc.). After biotinylated cover slips were rinsed with DI water, a flow cell was built from the biotinylated cover slip (top) and a clean glass slide (bottom), separated by two double sided tapes. To block non-specific binding sites on the biotinylated cover glass, 5 % bovine serum albumin (BSA, Sigma-Aldrich Inc.) with 0.05 % Tween-20 (T-20, sigma-Aldrich Inc.) in B-PBS buffer, containing 150 mM NaCl and 100 mM sodium phosphate at pH 7.2, was incubated in the flow cell for 2 h. The streptavidin coating was performed with incubation of 0.1 mg/mL of DyLight 488 conjugated streptavidin (Thermo Fisher Scientific Inc.) in the flow cell for 1 h. Another blocking solution was incubated for 1 h before introducing biotinylated gelsolin-actin complexes.

3.6 Optimal streptavidin concentrations

Optimal streptavidin concentration was determined prior to fabricating streptavidin-coated surfaces. A PDMS chip with 6 holes was prepared and placed on a biotinylated cover slip as shown in Figure 3.14.

The PDMS chip was stuck well to the biotinylated cover slip so that there was no leak of solutions when holes were filled. Each hole in the PDMS chip was filled with 0, 0.1, 1, 10, 100, and 200 μg/mL of streptavidin solutions, respectively. Streptavidin solutions were incubated for 30 min at room temperature. Unbound streptavidin was washed away with B-PBS buffer. The fluorescence intensity of streptavidin on the biotinylated surface was measured using area analysis in Wasabi software, which provides mean grey value and its standard deviation of selected areas.

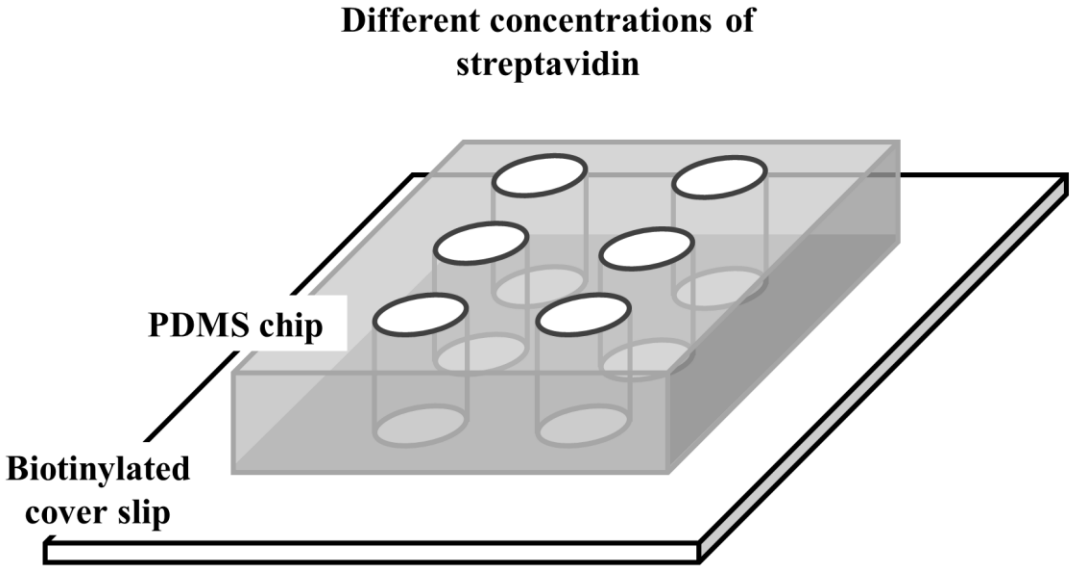

Figure 3.14 An illustration of an experimental setup. A PDMS chip with 6 holes was placed on biotinylated cover slip to compare fluorescence intensities for different concentrations of streptavidin.

3.7 Gelsolin activity in various free Ca^{2+} ions

After blocking non-specific binding sites on streptavidin-coated surfaces, 5 μg/mL of biotinylated gelsolin was incubated for 30 min in 25 mM KCl, 2 mM EGTA, 2 mM $MgCl_2$ and 25 mM Imidazole at pH 7.0. After washing away unattached biotinylated gelsolin, 0.25 μg/mL of F-actin was incubated for 30 min in 25 mM KCl, 2mM EGTA, 2 mM $MgCl_2$, 25 mM Imidazole with desired free Ca^{2+} concentrations at pH 7.0. The buffer composed of 25 mM KCl, 2mM EGTA, 2 mM $MgCl_2$, and 25 mM Imidazole was considered a zero free Ca^{2+} buffer. After F-actin incubation, unnecessary F-actin was washed away for observation. All experiments were performed at 24 ± 1 ℃.

3.8 Calculation of free Ca^{2+} concentrations

To investigate interactions of F-actin with gelsolin as a function of free Ca^{2+} concentrations, the accurate measurement of free Ca^{2+} concentrations in buffer solutions is important. Even a high purified chemical can have a trace of Ca^{2+}, which is critical for experiments necessary to control nanomolar concentrations of Ca^{2+}. Since ethylene glycol tetraacetic acid (EGTA) is a chelating agent for Ca^{2+}, using EGAT minimizes errors caused by such traces and provides the accurate control of the concentration of free Ca^{2+} in solutions. Since it is technically difficult to measure low concentrations of Ca^{2+}, a program estimating free Ca^{2+} concentration in buffer solutions in the presence of EGTA is utilized in this study. The program can be found at www.stanford.edu/~cpatton/maxc.html. The website provides two different Ca chelator programs, and Theo Schoenmakers' Chelator program is used to estimate free Ca^{2+} concentrations as shown in Figure 3.15.

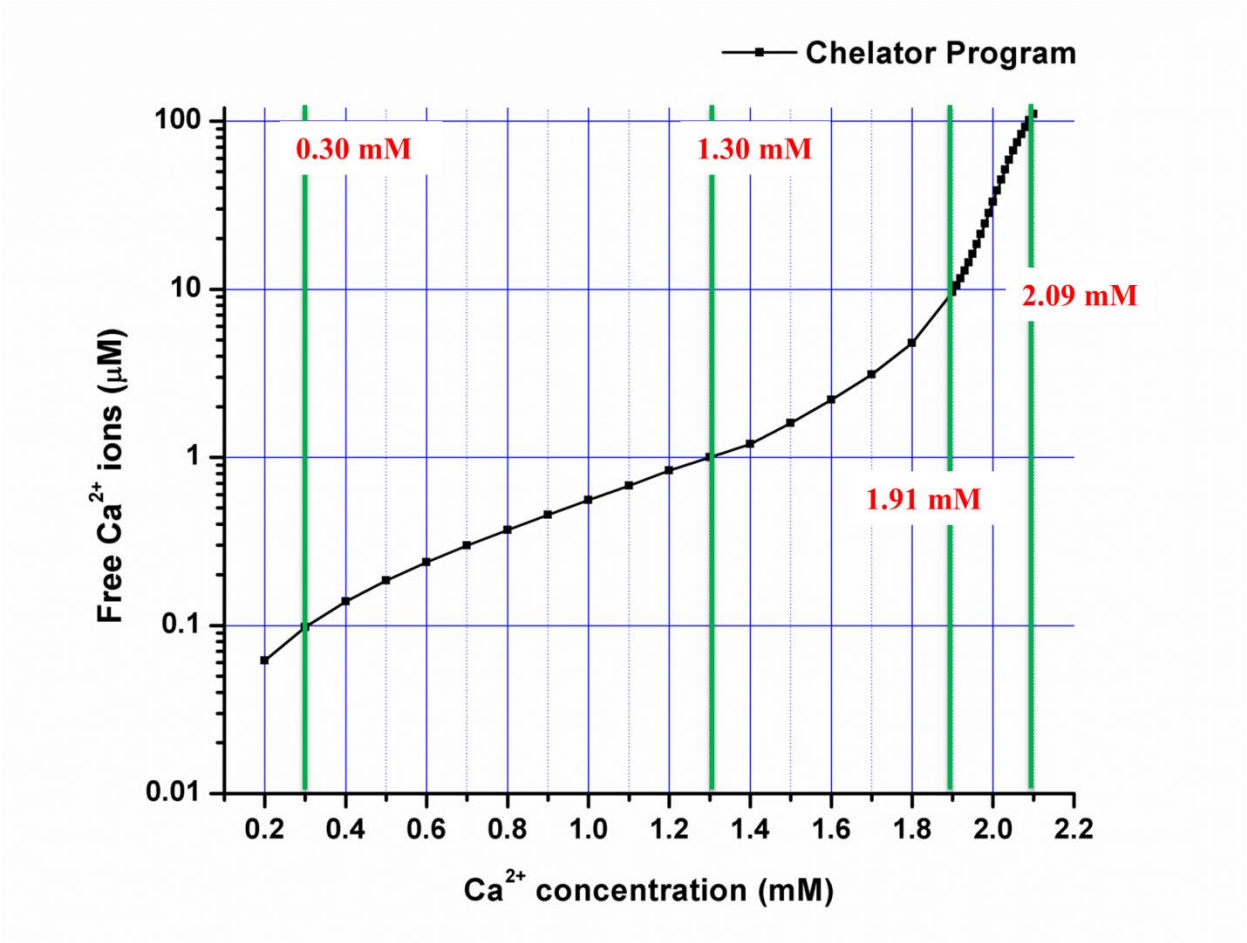

Figure 3.15 Free Ca^{2+} concentrations in the presence of 2 mM EGTA. This are calculated using Theo Schoenmakers' Chelator program.

3.9 Preparation of PLL-coated bead layer

In order to confirm actin-myosin motility on the surface of beads, bead layers were formed on the glass substrate. The general protocol to prepare bead layers is described below.

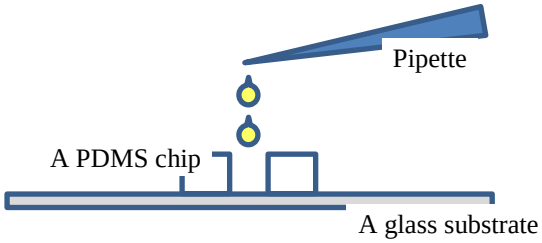

- Place a PDMS chip on a glass substrate
- Drop bead solution

- Incubation for 10–30 min

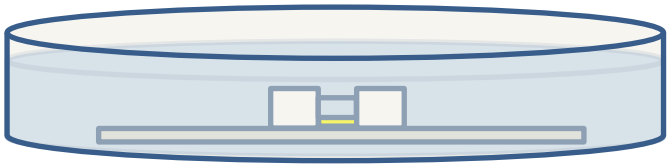

- Place it in DI-water bath
- Take off the PDMS chip carefully

- Remove DI-water using N_2 gas

3.10 Preparation of HMM-coated beads

For HMM-coated beads, the surface of beads was coated with poly-L-lysine (PLL, P4707, Sigma-Aldrich). In order to aid the adsorption of PLL, carboxyl-functionalized polystyrene beads (Spherotech Inc.) of various sizes (0.5, 1.3, 2.1, 4.5, and 6.7 μm in diameter) were used. When beads were incubated in 0.01 % PLL solution, all beads were diluted with PLL solution such that they had the same surface area (approx. 8.5 cm^2 for 200 μL). After exchanging PLL solution with M-buffer using centrifuge, 0.2 mg/mL of HMM incubated with PLL-coated beads for 30 min. Then 1 mg/mL of BSA at final concentration was followed for 10 min. Once HMM-coated beads were ready, they were mixed with motility assay solution, containing 1.5 mM ATP (A3377, Sigma-Aldrich), 10 mM dithothreitol (D0632, Sigma-Aldrich), 0.22 mg/mL glucose oxidase (49182, Sigma-Aldrich), 3.6 mg/mL catalase (C40, Sigma-Aldrich) and 450 mg/mL glucose (G7528, Sigma-Aldrich) in M-buffer, immediately before bead motility assay.

3.11 Chemical fixation of F-actin

The structures of single F-actin or the polarity of actin arrays were investigated using atomic force microscope (AFM, VEECO MultiMode Scanning Probe Microscope) or scanning electron microscope (SEM, JEOL JSM 7600F). The procedure of sample preparation for images was according to the published procedure with modification [93]. The freshness of each chemical is essential for successful imaging so chemicals were prepared immediately before use. The substrate was often modified with 0.001% (v/v) PLL solution for better adsorption of F-actin, and conductive substrates like ITO-coated glasses (SPI supplies Inc.) were also used in order to avoid surface charge effect during SEM.

Chemical fixation was followed at room temperature:

1. Incubate the sample with 2 % glutaraldehyde (GA, G7526, Sigma-Aldrich) in 0.1 M sodium phosphate buffer, pH 7.0, for 20 min

2. Incubate the sample with 0.1 % tannic acid (21700, Electron Microscopy Sciences) in 0.1 M sodium phosphate buffer, pH 7.0, for 20 min

3. Incubate the sample with aqueous 0.1 % uranyl acetate (19481, Ted Pella) for 20 min after deionized (DI) water rinse

4. Dehydrate the sample with a graded series of ethanol (25, 50, 75, and 100 %, 5 min each; 459836, Sigma-Aldrich)

5. Incubate the sample with 0.1 % uranyl acetate in anhydrous ethanol for 10 min

6. Before critical point drying, several rinses with anhydrous ethanol were followed

7. Critical point drying was performed using Autosamdri-815B, Series B (Tousimis Research)

8. After critical point drying, 1-3 nm of platinum was deposited on dried samples using sputtering system (CVC 610 DC Magnetron Sputtering Station) or e-beam evaporator (TEMESCAL BJD-2000, Ferrotec).

Before chemical fixation, F-actin samples were incubated with HMM solution at 1:1 molar ratio at room temperature, if necessary [17]. Unbound HMM was washed away using M-buffer.

3.12 Measurement of F-actin length

50 µg/mL of F-actin was incubated with gelsolin in desired molar ratios for 30 min at room temperature. Then, gelsolin-actin complexes were adsorbed electrostatically on 0.0001 % PLL coated cover slips for 10 min. The measurement of F-actin length adsorbed on PLL-coated surfaces was performed using a plug-in program called manual tracking in ImageJ software as shown in Figure 3.16. Manual tracking allows tracking moving particles in image sequences and provides valuable information such as XY coordinates, distances, and velocities. These features can be applied to measure the length of curved objects such as F-actin in still images. For this, an image sequence is made with 6 copies of a sample image, and it is assumed that the curved line of F-actin consists of straight line segments. The measurement starts from an end of selected F-actin, and each endpoint of straight line segments is followed in order to measure the total length. The data is analyzed using Matlab.

(A)

Results from 1620_1_01 in µm per sec

File Edit Font

# of Straight line segments

	Track n°	Slice n°			Distance
1	1.000	1.000	476.000	212.000	-1.000
2	1.000	2.000	482.000	290.000	5.046
3	1.000	3.000	528.000	318.000	3.473
4	2.000	1.000	950.000	342.000	-1.000
5	2.000	2.000	986.000	336.000	2.354
6	2.000	3.000	1108.000	290.000	8.410
7	3.000	1.000	780.000	348.000	-1.000
8	3.000	2.000	918.000	334.000	8.947
9	3.000	3.000	1004.000	322.000	5.601
10	3.000	4.000	1030.000	332.000	1.797

# of F-actin

8.519 µm

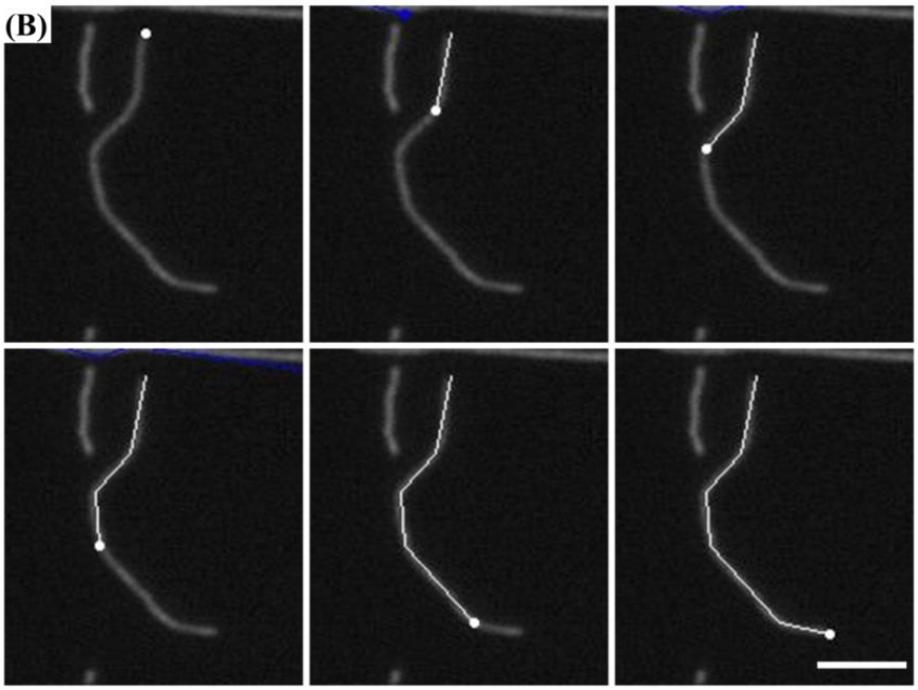

Figure 3.16 Length measurement of F-actin adsorbed on PLL-coated surface. (A) Measured data using manual tracking. The total distances of each F-actin are summed using Matlab. (B) An image sequence of the measurement. The measurement starts from an end of F-actin, and each endpoint of straight line segments is followed in order to measure the total length. (Bar size is 3 μm)

3.13 Measurement of actin coverage

To investigate the effect of blocking agents that prevent non-specific binding of F-actin and interactions of F-actin with gelsolin immobilized surfaces as a function of free Ca^{2+} concentrations, the area covered by fluorescent F-actin on surfaces was measured, as shown in Figure 3.17. For the measurement, each image was converted to a binary image, black and white image, using ImageJ (Image –> Adjust –> Threshold in menu). Pixels of black color indicated the fluorescence of F-actin. They were counted for the area occupied by F-actin using Matlab software.

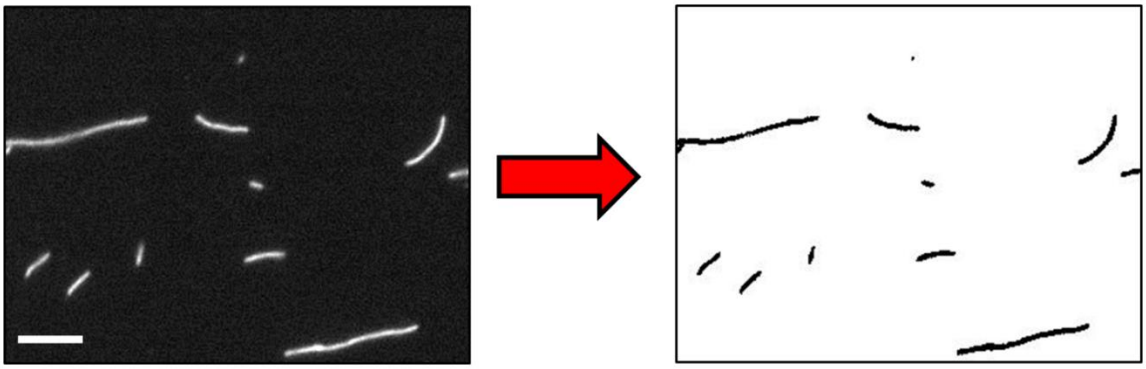

Figure 3.17 The measurement of F-actin coverage on the surface. The image showing the surface covered by F-actin was converted into the black and white (BW) image. The black pixels in the BW image were counted using Matlab, which represented the coverage of F-actin on the surface. (Bar size is 5 μm)

CHAPTER 4 – RESULTS AND DISCUSSIONS

4.1 Actin filament images

The structural properties of actin filaments are often studied using electron microscopy (EM) or atomic force microscopy (AFM) because of their high resolution. This study examines how the structural polarity of actin filaments in the actin arrays is oriented. When myosin S1 or HMM incubates with actin filaments in the absence of ATP, myosin S1 or HMM rigidly binds to actin filaments and forms arrowhead patterns along actin filaments [94]. The barbed end of the arrowhead patterns is the plus end of actin filaments, while the pointed end of arrowhead patterns is the minus end of actin filaments. To acquire such structural patterns of biological samples using EM or AFM, however, the sample preparation is very critical since samples are required to be completely dried before examination. During air drying, biological samples can suffer severe collapse, deformation, and shrinkage primarily due to the effects of surface tension. Therefore, various methods such as chemical fixation, freeze drying, hexamethyldisilizane (HMDS), or critical point drying are introduced to preserve and stabilize their structures.

In this study, chemical fixation and critical point drying are used to prepare actin filament samples. Chemical fixation is a chemical process by which structures of biological samples are preserved as they naturally occur in living cells for microscopy or other analysis. Chemicals used for chemical fixation are often called fixatives. The purpose of fixatives is to stabilize structures of biological samples as forming covalent crosslinks between molecules or to provide better electron contrast for electron microscopy. There are numerous different sequences and combinations of fixatives to fix samples, but T. M. Svitkina's method was employed with minor modifications after investigation [93]. The chemical fixation was performed with the combination of glutaraldehyde, tannic acid, and uranyl acetate as described in Chapter 3. Glutaraldehyde and uranyl acetate can be used alone as primary fixatives, but it is reported that combining these chemicals significantly improves the quality of electron microscopic images of cytoskeleton [93].

As mentioned above, the effect of surface tension is a main factor of deformation or collapse of biological samples in the process of drying. Most biological samples are in aqueous solutions, and water has a high surface tension against air, compared to ethanol or methanol. To reduce the surface tension, aqueous solutions can be exchanged with a different medium which has lower surface tension. The most popular method to minimize surface tension is the technique of critical point drying since almost zero

surface tension is possible during the drying process. Each material has its own critical temperature and pressure where liquid and gas phases can coexist as shown in Figure 4.1. When achieving the critical point, the liquid phase can be converted to the gas phase without crossing the liquid-gas boundary. As a result, no surface tension occurs.

For critical point drying of biological samples, liquid carbon dioxide (CO_2) is popularly used. Compared to the critical point of water, around 374 ℃ and 229 bar, where any biological sample would be destroyed, the critical point of CO_2, around 31 ℃ and 74 bar, is more appropriate for biological samples.

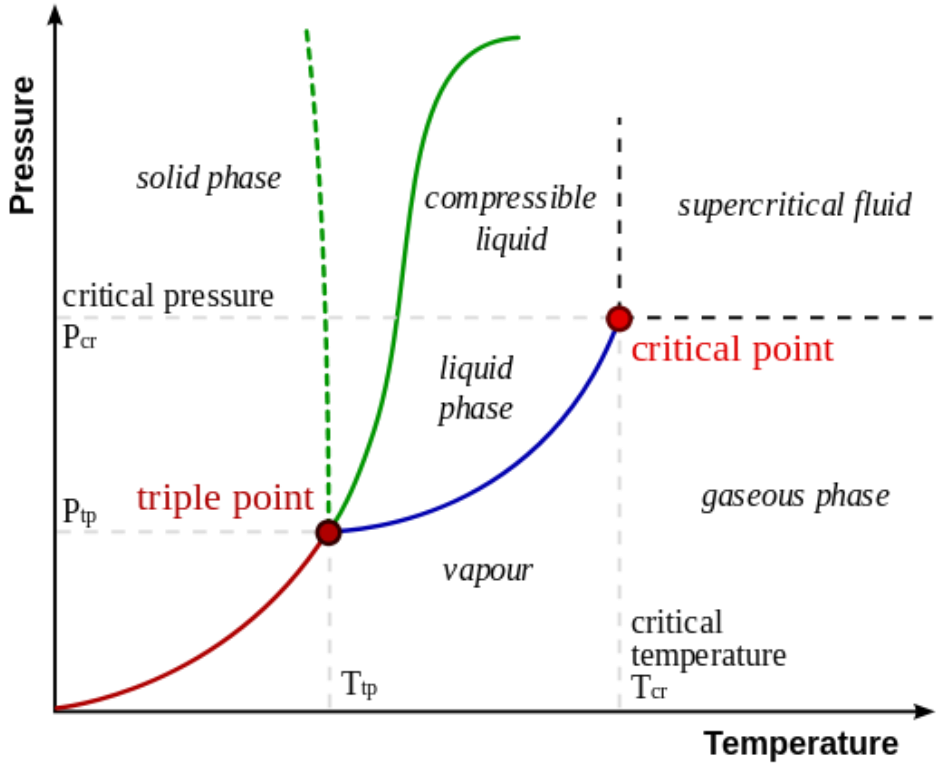

Figure 4.1 Phase diagram showing pressure to temperature ranges where solid, liquid and vapor exist. It is possible that liquid and gas phases can coexist at a particular temperature and corresponding pressure. This is called the critical temperature and pressure, or critical point. When achieving the critical point, the liquid phase can be converted to the gas phase without crossing the liquid-gas boundary. As a result, no surface tension occurs during the process of drying.

Ethanol dehydration and critical point drying were carefully performed since even small traces of water or ethanol during critical point drying can cause distortion of samples. Since liquid CO_2 is not miscible with water, it is necessary to replace water with an intermediate fluid like methanol, ethanol, or acetone, which is miscible with both water and liquid CO_2. In this study, anhydrous ethanol was used as the intermediate fluid. Samples were dehydrated through a graded series of 25, 50, 75, and 100% ethanol for 5 min at each step after chemical fixation. Dehydration was performed with caution to minimize the residue of water. In addition, a water-absorbing filter was attached to the liquid CO_2 tank to prevent any trace of water from liquid CO_2 during critical point drying [95].

During operation of the critical point dryer, ethanol was completely exchanged by liquid CO_2 by refreshing the camber for 10 min. In addition, samples were loaded horizontally, and liquid-permeable spacers were placed between samples to minimize possible surface tension during critical point drying [93].

4.1.1 AFM images of actin filaments

Atomic force microscopy (AFM) uses a cantilever with a tip at its end to probe the specimen surface. The resolution of AFM depends on the radius of the tip, and AFM can image specimens at nanometer resolution. In principle, AFM measures a deflection of the cantilever due to forces between the tip and the sample. The forces can be physical contact forces, van der Waals forces, electrostatic forces, and magnetic forces.

The operation of AFM has three different modes: contact mode, non-contact mode, and tapping mode. In contact mode, the tip drags across the surface of samples, and repulsive forces between the tip and the surface are measured to image the surface. In non-contact mode, the tip does not contact the surface. Instead, the cantilever is oscillated above the surface with amplitude of oscillation of a few nanometers (< 10 nm) at near the intrinsic resonance frequency of the cantilever. As the tip approaches the surface of samples, the attractive van der Waals forces between the tip and the surface are measured to image the surface. The operation of tapping mode is similar to non-contact mode. However, the difference between tapping mode and non-contact mode is that tapping mode has large amplitude of oscillation (typically greater than 20 nm) and intermittent contacts to the surface. AFM images in tapping mode are produced by measuring the forces between the tip and the surface during intermittent contacts. Tapping mode has benefits over contact mode and non-contact mode. It can minimize damage to both sample and tip, which occurs in contact mode. In addition, tapping mode can prevent the tip from sticking to the surface and

stopping the oscillation which occurs in non-contact mode. Those problems occurring with non-contact mode can create artifacts in AFM images.

In this study, AFM images for single actin filaments were investigated using tapping mode. As mentioned above, contact mode can cause substantial damage on soft samples like biological samples, so tapping mode is more suitable for images of actin filaments. The samples were prepared on glass cover slips with the procedure described in Chapter 3 with the exception of Pt thin film deposition. AFM was equipped with an "E" scanner, whose scan size is 10 μm × 10 μm. Approx. 4 μm thick, 125 μm long Si probes (PPP-NCHR, Nanosensors) with a tip radius less than approx. 10 nm were employed to probe the samples. During scanning, the force constant and resonance frequency were 42 N/m and 338 kHz, respectively.

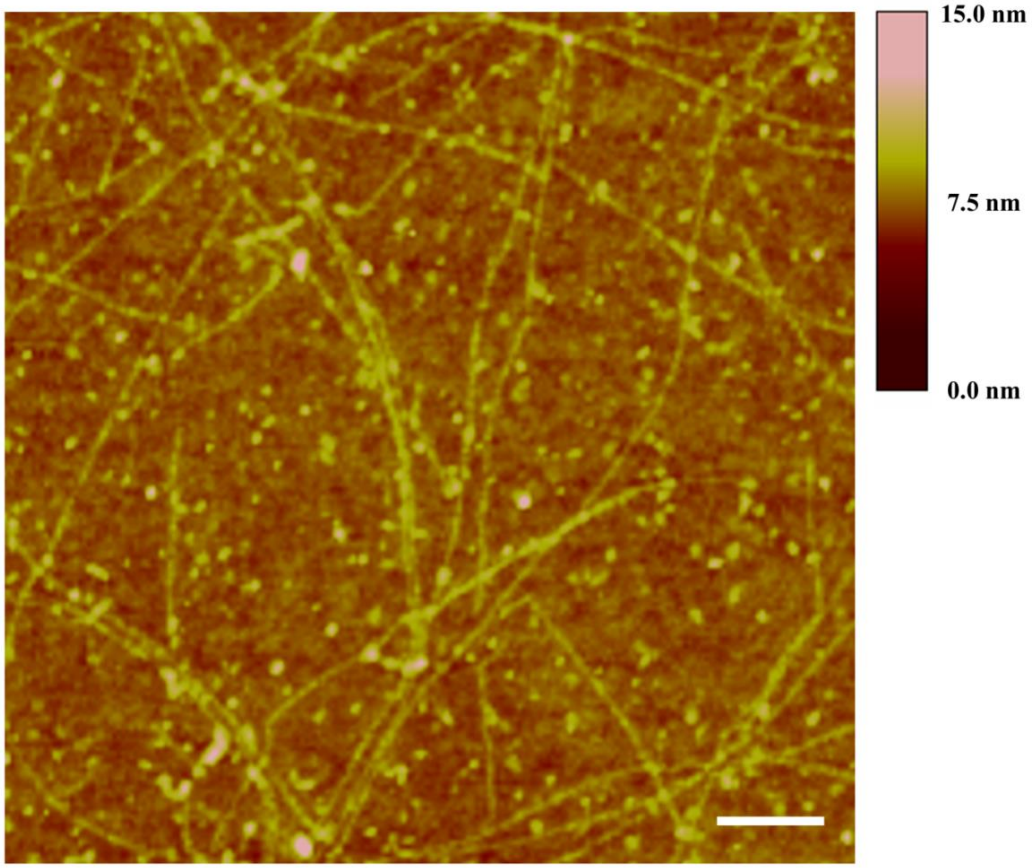

Figure 4.2 An AFM image of single actin filaments on the glass substrate. Actin filaments were randomly distributed on the glass substrate. The AFM image showed clear images of single actin filaments. The scan size was 2 μm × 2 μm with a scan rate of 1 Hz. The bar size is 200 nm.

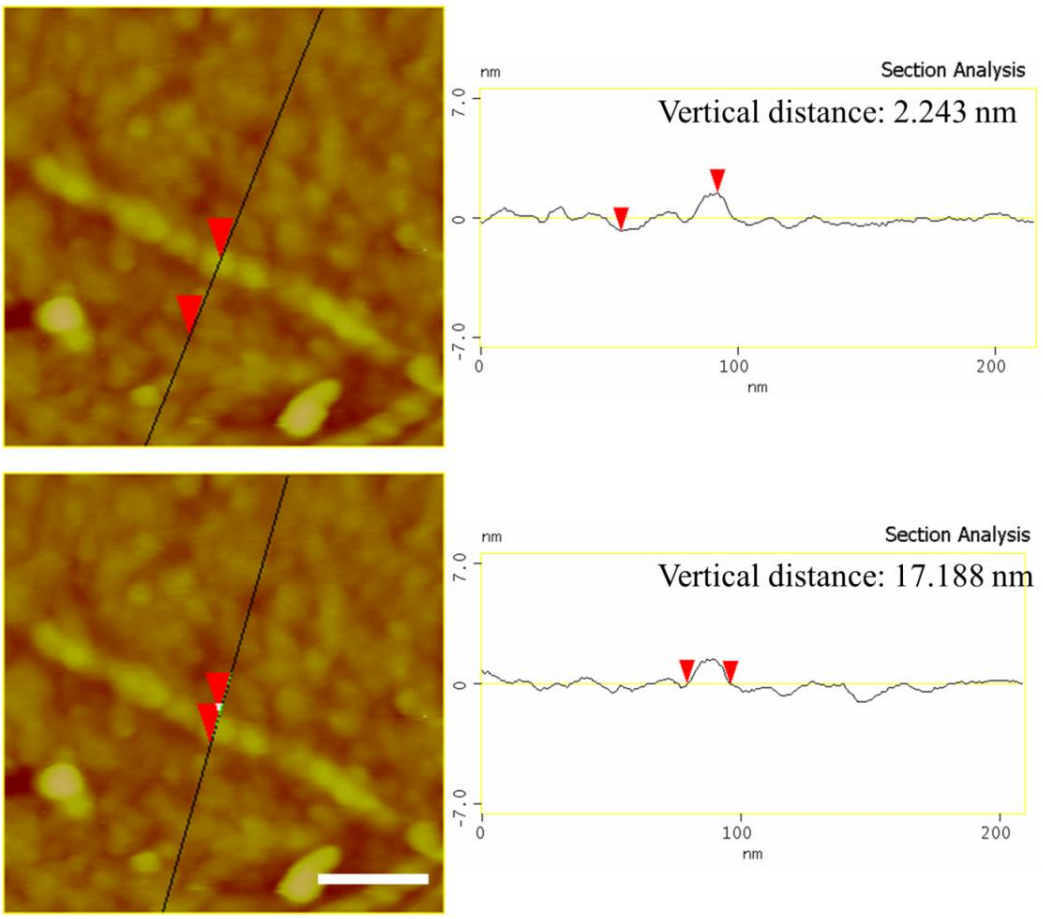

Figure 4.3 The height and width of a single actin filament measured by AFM. The average height and full width of the filaments in AFM images were 2.4 ± 0.2 nm and 18 ± 2 nm, respectively (n=3). The scan size was 200 nm × 200 nm with a scan rate of 0.5 Hz. The bar size is 50 nm.

Images of single actin filaments were successfully acquired using AFM as shown in Figure 4.2 and 4.3. The images showed that the shape of actin filaments was like a long rod, and the average height and full width of the filaments in AFM images were 2.4 ± 0.2 nm and 18 ± 2 nm, respectively. These values are consistent with other reports, in which the height and width of actin filaments are 2.1 ± 0.3 nm and 20 ± 3 nm, respectively [96].

From electron microscopic images, it is known that a single actin filament is 7-8 nm in diameter. Compared to EM studies, the shape of actin filaments in AFM images seems to be flattened. Unlike non-contact mode, the tip of AFM in tapping mode makes intermittent contacts with the sample. Although the

forces encountered by the tip on the sample are less compared to contact mode, these forces can cause elastic deformation of the sample. This effect is called “height lowering”. Height lowering is often observed in the soft samples. As a result, the height of actin filaments in AFM images may be reduced compared to their original structure. In addition to the height lowering effect, one of the major AFM artifacts is tip-sample convolution. Due to the sharpness of the tip, AFM demonstrates high resolution below 1 nm. However, any AFM image is a result of a convolution of the tip’s shape and the sample’s geometry. Convolution effects can induce image artifacts, especially when the radius of the tip is comparable or greater than the surface features. One of the well-known convolution effects is known as “profile broadening” effect. Since the features of actin filaments are generally similar or smaller than the radius of the tip, an image showing a large width of actin filaments can be explained by this effect. Unlike other reports, the helical structure of actin filaments was not observed in this study. Higher resolutions of actin filaments in AFM imaging may be achieved by using a scanner of smaller scan size like an “A” scanner of 0.4 μm × 0.4 μm scan size and an extremely sharp tip like carbon nanotube tips [97].

4.1.2 SEM images of actin filaments

A scanning electron microscope (SEM) produces high resolution images using an electron beam. While the maximum resolution of an optical microscope is limited around 200 – 250 nm due to the Abbe diffraction limit, the resolution of the SEM can be up to 1 nm. In addition to higher resolution, the use of electrons induces a variety of signals providing information about the specimen including surface morphology and chemical composition due to electron-sample interactions.

The signals derived from electron-specimen interactions contain secondary electrons (SE), backscattered electrons (BSE), characteristic X-rays, Auger electrons, and cathodoluminescence (CL) as shown in Figure 4.4 [98]. Secondary electrons are generated by inelastic scattering interactions between incident electrons and specimen electrons. These electrons have energies of less than 50 eV, which means only secondary electrons generated near the surface are detected. As a result, secondary electrons provide good topographic information of specimens. In contrast, backscattered electrons are generated by elastic scattering interactions between incident electrons and specimen electrons. Since these electrons possess higher energies than secondary electrons, backscattered electrons contain information of deeper regions from the surface. Backscattered electrons can be used for elemental analysis of the specimen with characteristic X-rays since the higher atomic number of the specimen atoms yield a greater number of backscattered electrons. Another useful signal generated from electron-specimen interactions is characteristic X-ray. The incident electron beam may eject an electron in an inner shell. To fill the

vacancy, an electron from an outer shell moves to the inner shell, releasing energy in the form of an X-ray. The energies of X-rays are characteristic of the atomic structure of the element, which allows for determination of the elemental analysis or chemical characterization of the specimen.

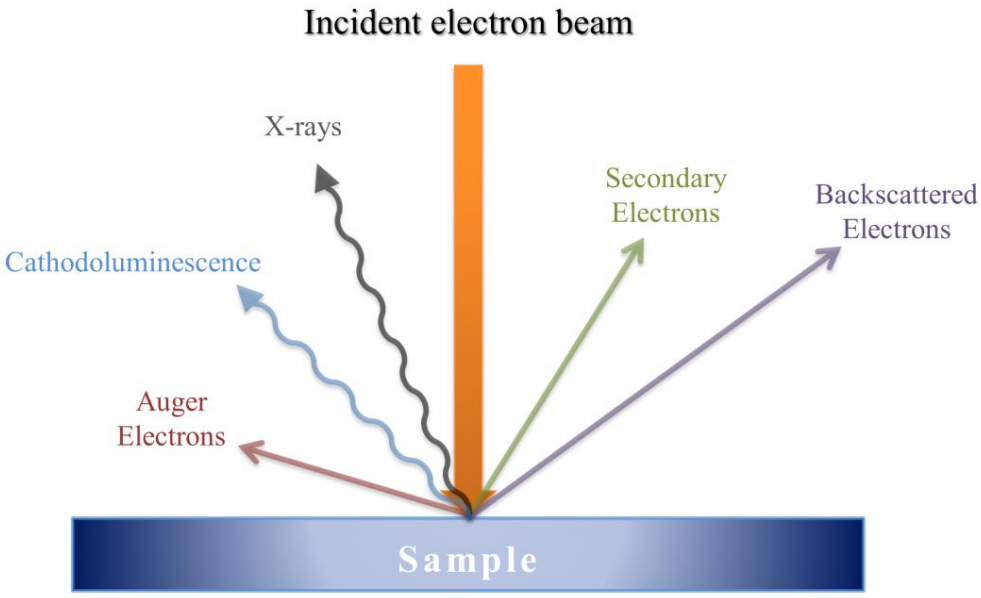

Figure 4.4 A variety of signals derived from electron-specimen interactions. When an electron beam strikes a specimen, the signals derived from electron-specimen interactions contain secondary electrons (SE), backscattered electrons (BSE), characteristic X-rays, Auger electrons, and cathodoluminescence (CL).

For SEM imaging of actin filaments, gentle beam (GB) mode was attempted at 2 kV with an approx. 3 mm working distance (WD) to minimize effects of surface charge and damages on the samples. However, the size of actin filament is only a few nanometers, which prevents clear observation with gentle beam mode. Typically, higher accelerating voltages provide better resolution as shown in Figure 4.5, and it was found that SEM mode at 15kV with approx. 5 mm WD provided the best images of actin filament samples. Using this setting, SEM images for single actin filament and HMM decorated actin filament were investigated. The images successfully showed structural features of actin filaments which has been reported elsewhere [2].

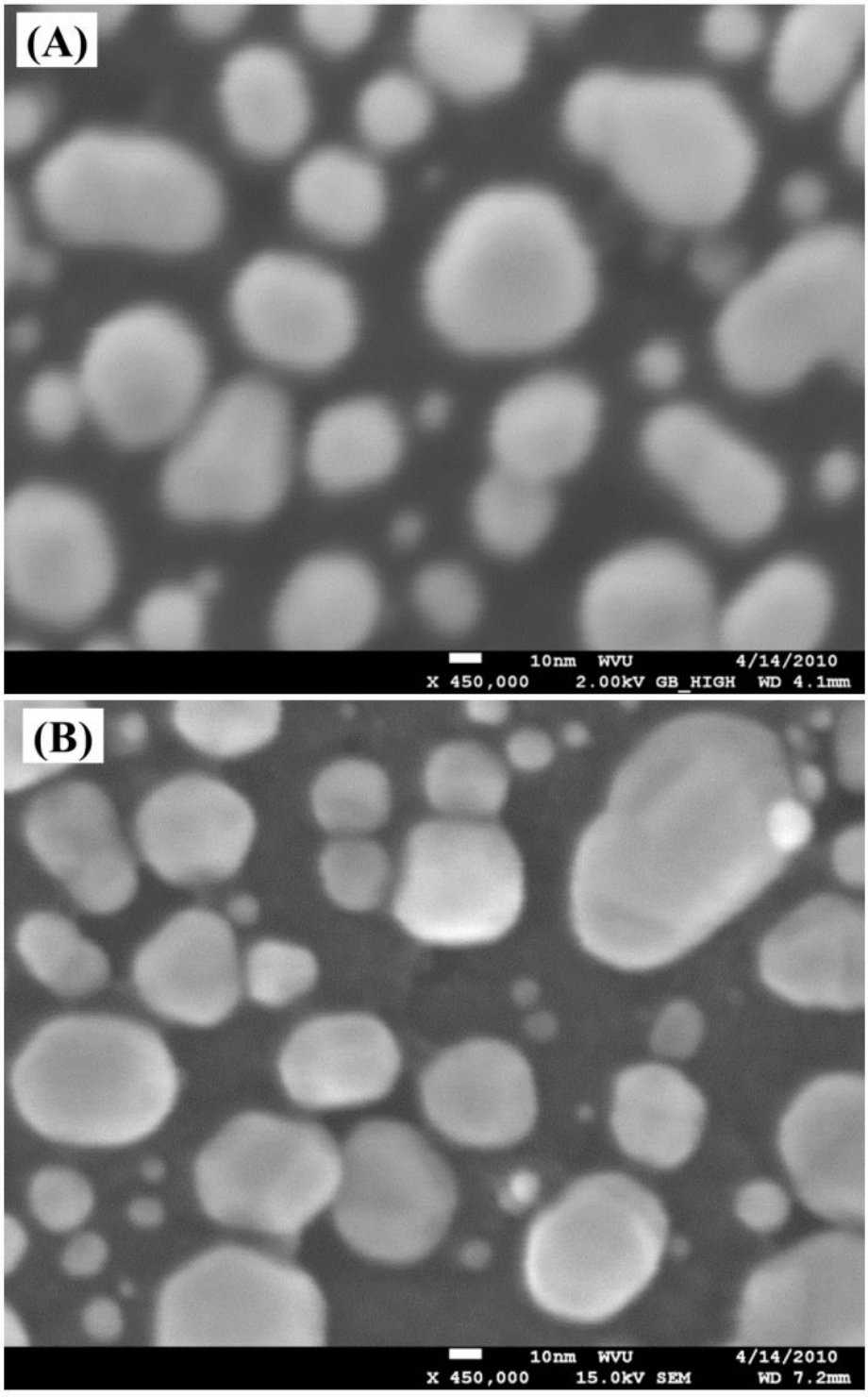

Figure 4.5 The difference of the resolution between GB mode and SEM mode in observing a sample of gold particles. (A) GB mode. The accelerating voltages were 2.0 kV. (B) SEM mode. The accelerating voltages were 15.0 kV.

Like AFM images, SEM images also enabled observation of the structure of actin filaments. As shown in Figure 4.6, the shape of actin filaments is similar to a long rod, and the size of the filaments is approx. 9 nm in diameter. It is known that a single actin filament is 7-8 nm in diameter. The larger diameter in our SEM images may be due to the deposition of Pt film. With HMM decoration, right handed helical structures of actin filaments were observed as shown in Figure 4.7. Furthermore, arrowhead patterns along actin filaments appeared so that the polarities of actin filaments were determined, as shown in Figure 4.8.

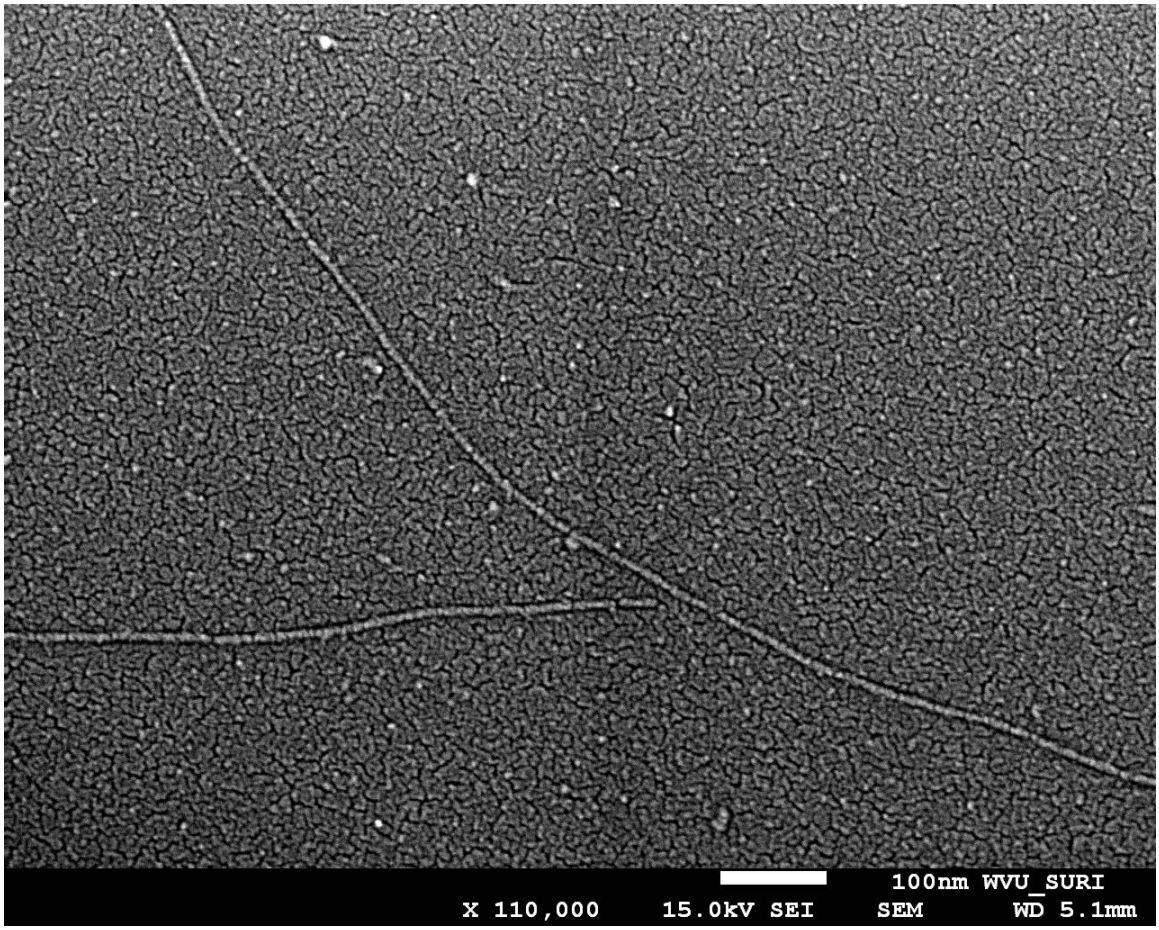

Figure 4.6 SEM image of a single actin filament. The measured diameter was approx. 9 nm. It was thicker than 7 nm, the diameter of actin filament. The increased thickness is probably due to thin Pt film.

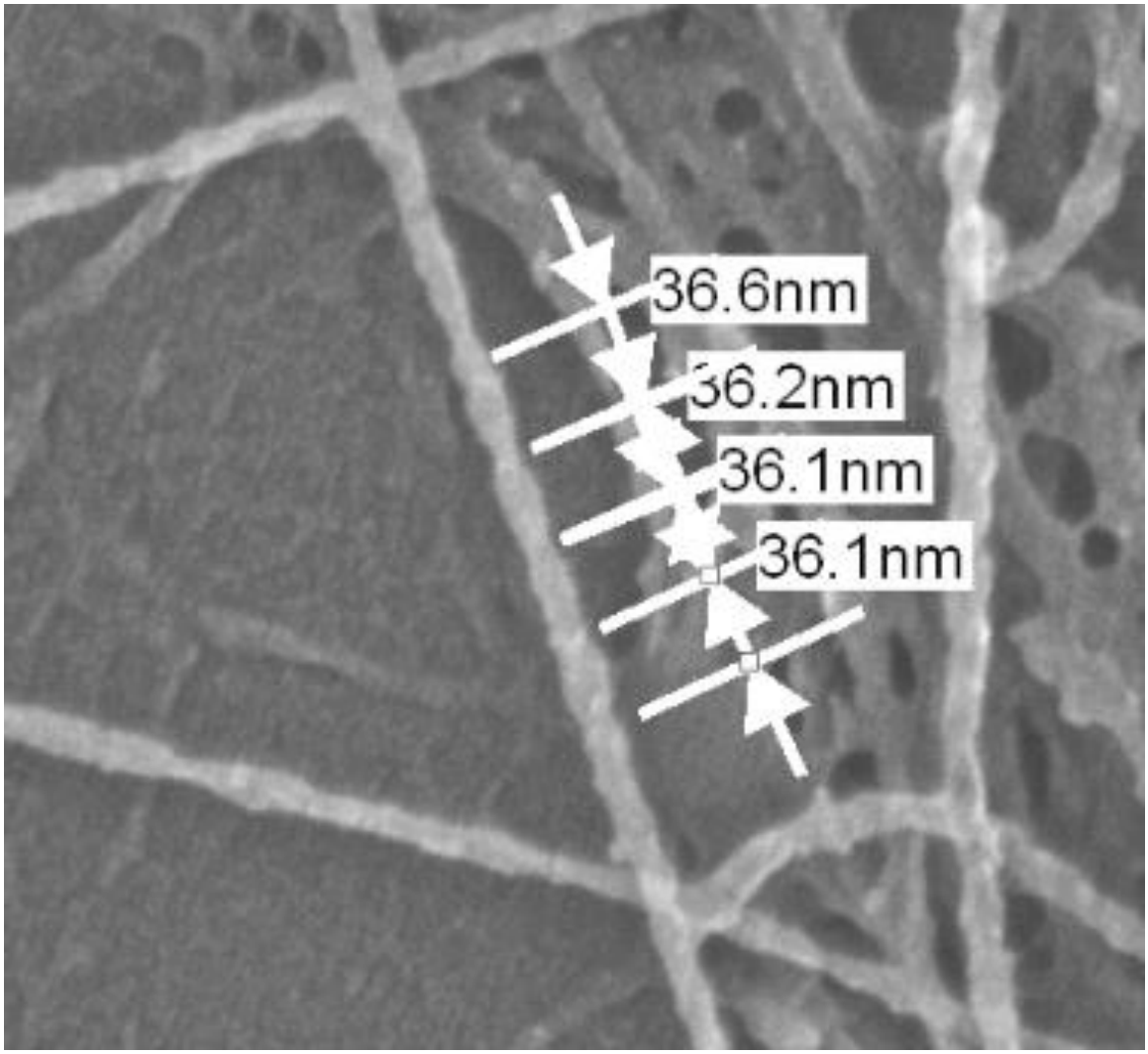

Figure 4.7 SEM image of HMM decorated F-actin. Helical structures which are repeated every 36nm were observed.

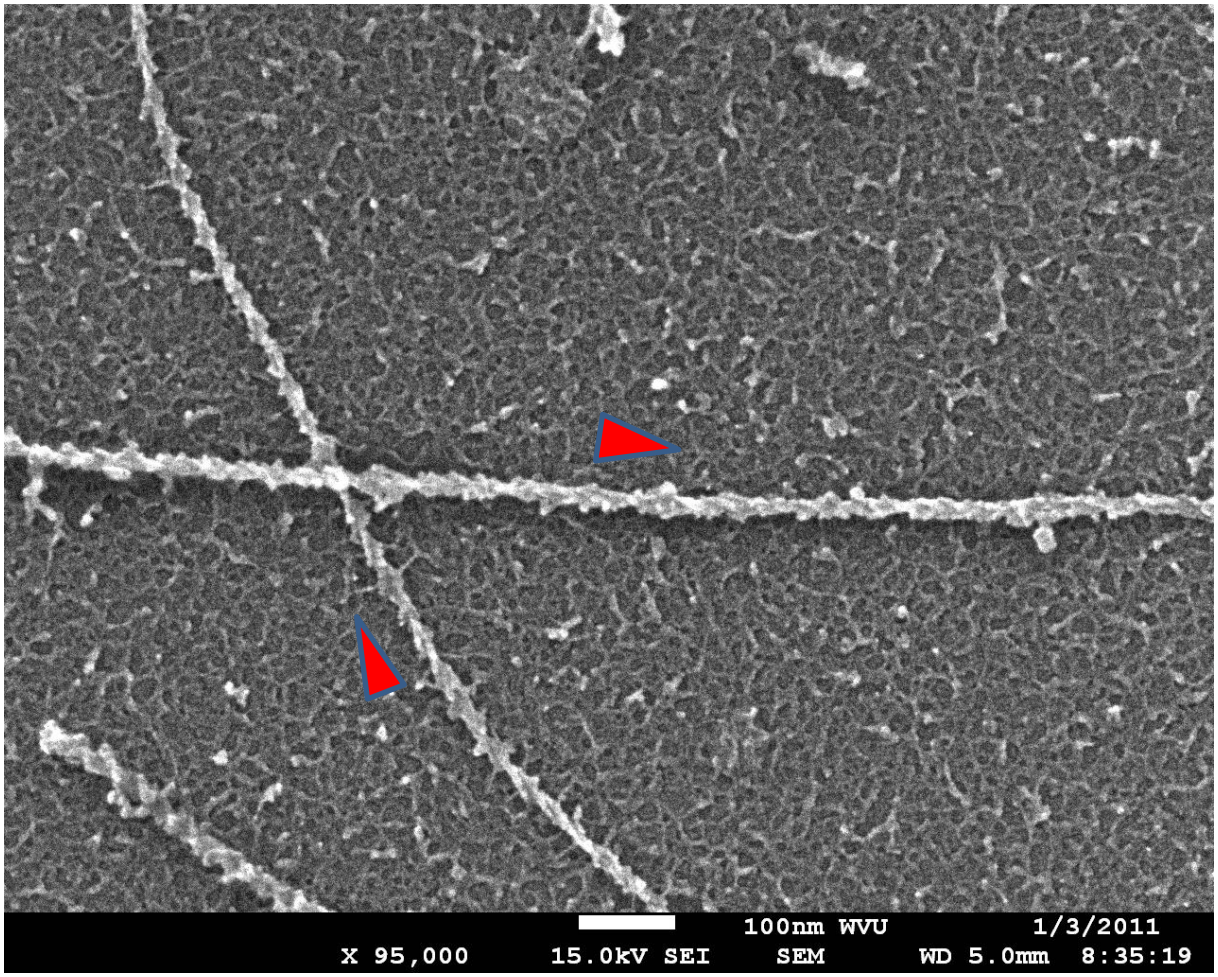

Figure 4.8 Structural polarity of HMM decorated F-actin. Arrowhead patterns were observed on HMM decorated F-actin.

Increasing the resolution of F-actin images requires exploration of other technical approaches. Myosin S1 is a common material to decorate F-actin for arrowhead patterns. Unlike HMM, myosin S1 lacks a tail domain, so it can provide clearer arrowhead patterns. Higher accelerating voltages available in STEM mode of transmission electron microscopy (TEM) may give higher resolution.

To conclude, we successfully obtained actin filament images using SEM and AFM. These images showed structural features of the filament such as shape, diameter, the loop of helix and polarity. Using these high resolution microscopies, we can identify the polarity of oriented F-actin arrays.

4.2 A Visualized Observation of Ca^{2+}-dependent Gelsolin Activation

Gelsolin, an actin binding protein, regulates assembly and disassembly of actin in eukaryotes by severing an actin filament (F-actin) and subsequently remaining capped at the barbed end [99-102]. As a result, it plays a role in regulation of changing the shape and motility of the cell [103, 104]. It is known that gelsolin is composed of six homologous domains (G1-G6) that fold together in order to form a compact globular shape in the absence of free Ca^{2+} as shown in Figure 4.9. In this structure, the helical tail of G6 latches onto the G2 subdomain, thereby burying the actin binding domains, G1, G2 and G4 so they are not accessible to F-actin [105]. However, in the presence of free Ca^{2+}, gelsolin undergoes conformational changes, in turn, affecting its interactions with actin. Free Ca^{2+} ion binding to G4-G6 disrupts the contact of G2 with G6, and it causes exposing the F-actin binding site on G2 [106-108].

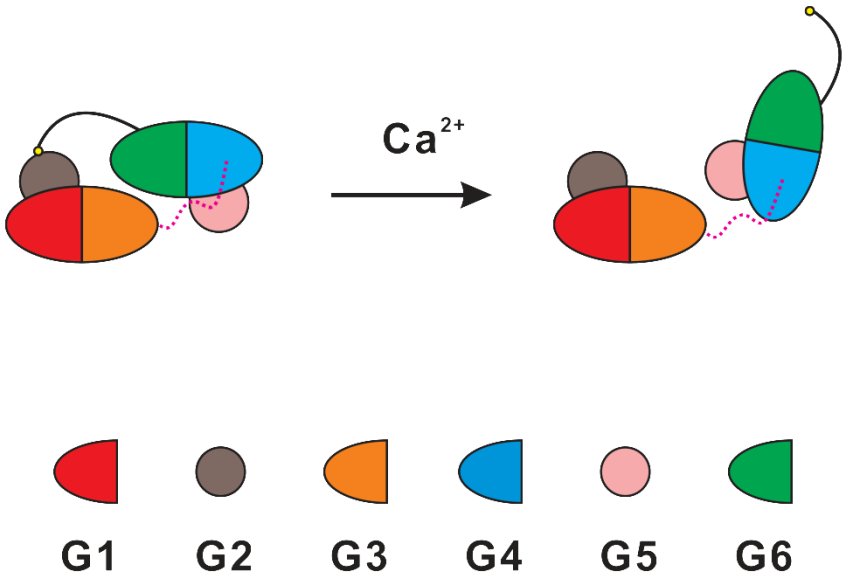

Figure 4.9 The activation of gelsolin by free Ca^{2+} ions [105].

Gelsolin activities related to free Ca^{2+} have been investigated in a number of different studies involving fluorescence [109-114] and x-ray crystallography [105, 108, 115-117] but there is an inconsistency in the literature. Lamb *et al.* reported that half-maximal activation of gelsolin severing and nucleating activities occurred at 10 μM free Ca^{2+} and free Ca^{2+} requirement for gelsolin activity was affected by pH [114]. Kinosian *et al.* reported that half maximum binding of gelsolin to F-actin occurred

at ~0.1 μM free Ca^{2+} while half maximum severing and barbed end capping of F-actin by gelsolin occurred at ~0.4 μM free Ca^{2+} [111]. Pope *et al.* suggested that Ca^{2+} increased the hydrodynamic radius of gelsolin with half-maximum at ~30 nM free Ca^{2+}, which appeared to open the gelsolin molecule due to release of the helical tail of G6 from G2 [118]. Small-angle x-ray scattering (SAXS) analysis of full length human plasma gelsolin elucidates three states of conformational change of gelsolin in relation to free Ca^{2+} concentrations. The initial state, in which the compact structure dominates, occurs from 0 to ~10 nM Ca^{2+}. The intermediate state, in which opening of gelsolin is proportional to free Ca^{2+} concentration, occurs at ~0.1 – ~10 μM Ca^{2+}. Finally, the fully activated state, in which opening of gelsolin is at a maximum, occurs at ~100 μM – 1 mM Ca^{2+} [119].

Although Bearer *et al.* had observed fluorescent actin filaments severed by gelsolin bound to the surface [120], it is necessary to develop an approach for direct observation of actin filament interacting with gelsolin to clearly understand gelsolin activity in relation to F-actin in various free Ca^{2+} concentrations as shown in Figure 4.10. In this heterogeneous approach, gelsolin was immobilized on streptavidin-coated surface using biotinylation. As a result, the interaction between gelsolin and F-actin was visualized.

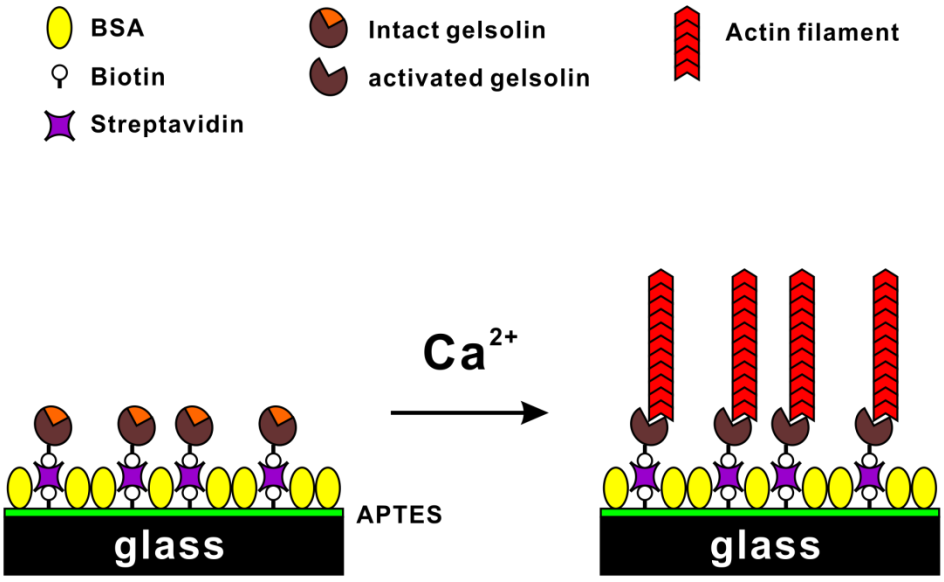

Figure 4.10 Illustration of observation of F-actin coverage on a gelsolin-immobilized surface.

4.2.1 Biotinylation of Gelsolin

To immobilize gelsolin on the surface, gelsolin was biotinylated using NHS-PEG_4-Biotin. The detailed procedure of gelsolin biotinylation is described in Chapter 3. Once gelsolin was biotinylated, the number of biotin molecules per gelsolin molecule was measured using the Pierce Biotin Quatitation Kit. Measurement indicated a gelsolin molecule contains approx. 1.4 biotin molecules. Biotinylation of gelsolin was also verified using streptavidin-coated particles (0.5 μm in diameter, Spherotech Inc.). When streptavidin-coated particles were incubated with the complexes of biotinylated gelsolin and F-actin (1:500, w/w), it was found that several F-actins were bound to streptavidin-coated particles, as shown in Figure 4.11. This result suggested that biotinylated gelsolin connected between F-actin and streptavidin-coated particles. It was hypothesized that the barbed end of F-actin was anchored on the surface of streptavidin-coated particles because biotinlyated gelsolin capped the barbed end of F-actin.

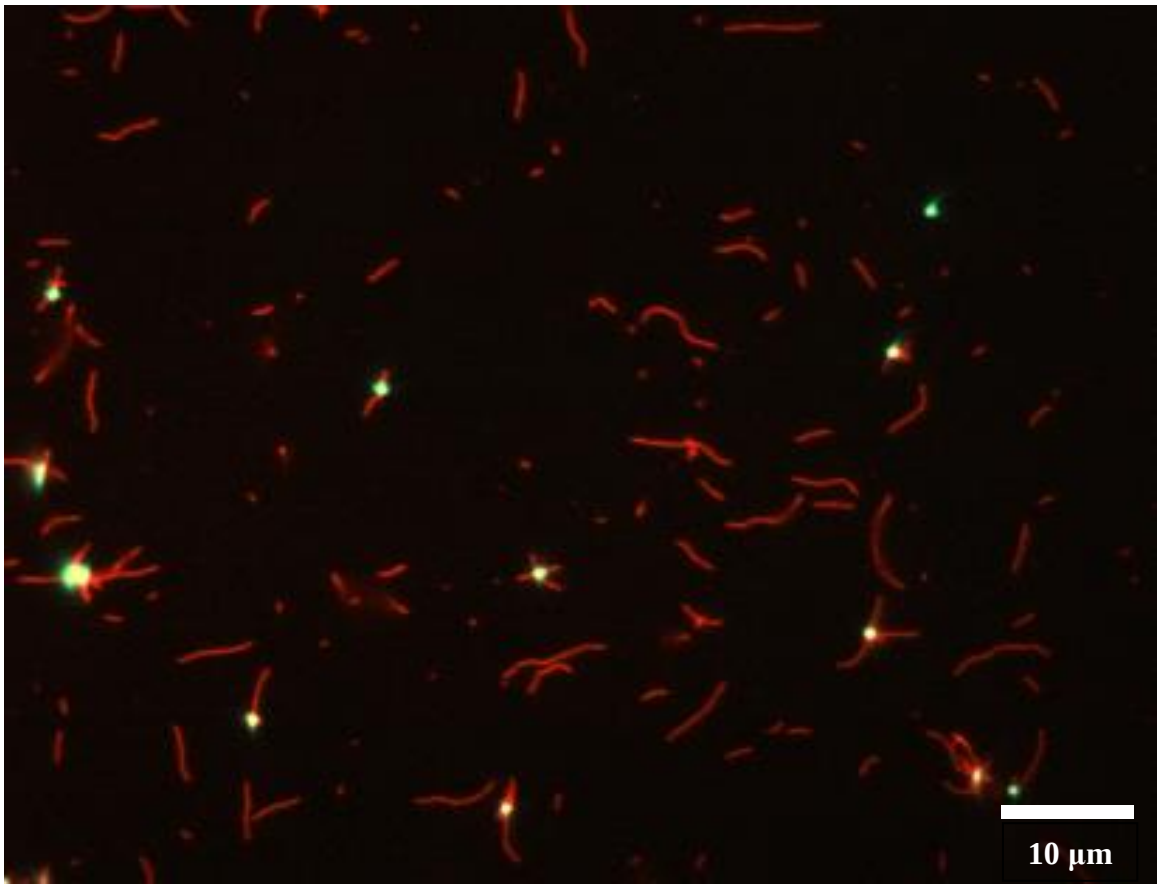

Figure 4.11 An image of streptavidin particles with the complexes of biotinylated gelsolin and F-actin. Several F-actins were bound to streptavidin-coated particles due to biotin-streptavidin interactions. Green particles were

streptavidin-coated particles and red rods were the complexes of gelsolin and F-actin. The barbed end of F-actin was bound to streptavidin-coated particles because gelsolin capping the barbed end of F-actin was biotinylated.

4.2.2 Gelsolin activity after biotinylation

Phalloidin binds between two actin subunits on polymerized actin in noncovalent manner, preventing the depolymerization of F-actin [21]. However, it is known that attachment of phalloidin to F-actin does not significantly influence the rate of severing F-actin by gelsolin [109]. Therefore, these suggest that although phalloidin labeled F-actin is shortened and its barbed end is capped by gelsolin, there is no depolymerization of F-actin and severed F-actin maintains its length [110, 121]. As a result, gelsolin activity that provokes the severing of F-actin can be confirmed by measuring the length of F-actin after incubation of gelsolin and F-actin in various concentration ratios.

The length of F-actin as a function of the molar ratio of gelsolin and F-actin is measured using the ImageJ program described in Chapter 3 and the results are shown in Figure 4.12 and 4.13. In order to verify if gelsolin activity was altered by biotinylation, the length of F-actin interacting with biotinylated gelsolin was compared to the length of F-actin interacting with untreated gelsolin. The data indicates that the average length of F-actin incubated with gelsolin is reduced as gelsolin concentration increased. Data also indicates that there is no difference in the activity between biotinylated gelsolin and untreated gelsolin. The average length of F-actin incubated with gelsolin at 1620:1 (w/w) ratio (50:0.0309 μg/mL, F-actin:gelsolin) was ~10 μm, which is similar to the average length of normal F-actin. There was a large size of the error bar in the measurement because of the variety of the length of polymerized F-actin. However, the difference in the length between 486:1 and 1620:1 (w/w) ratios (F-actin:gelsolin) was distinguishable. The difference was more obvious at higher concentrations of gelsolin. No fluorescent F-actin was found at 1:1 (w/w) ratio (50:50 μg/mL, F-actin:gelsolin), perhaps due to the displacement of most rhodamine-conjugated phalloidin on F-actin by gelsolin [109]. Comparison with the theoretical length of F-actin suggests that the severing efficiency of gelsolin appears to be reduced at high ratios of gelsolin:F-actin, which is consistent with the previous study reported in [106]. It is assumed that gelsolin caps the barbed end of F-actin after severing while direct capping of gelsolin to existing barbed ends is negligible [106]. Thus, the theoretical length of F-actin is simply calculated based on molar ratio between F-actin and gelsolin using Ken Holmes's actin filament model, in which 13 actin subunits form ~ 36 nm long helical structure [14].

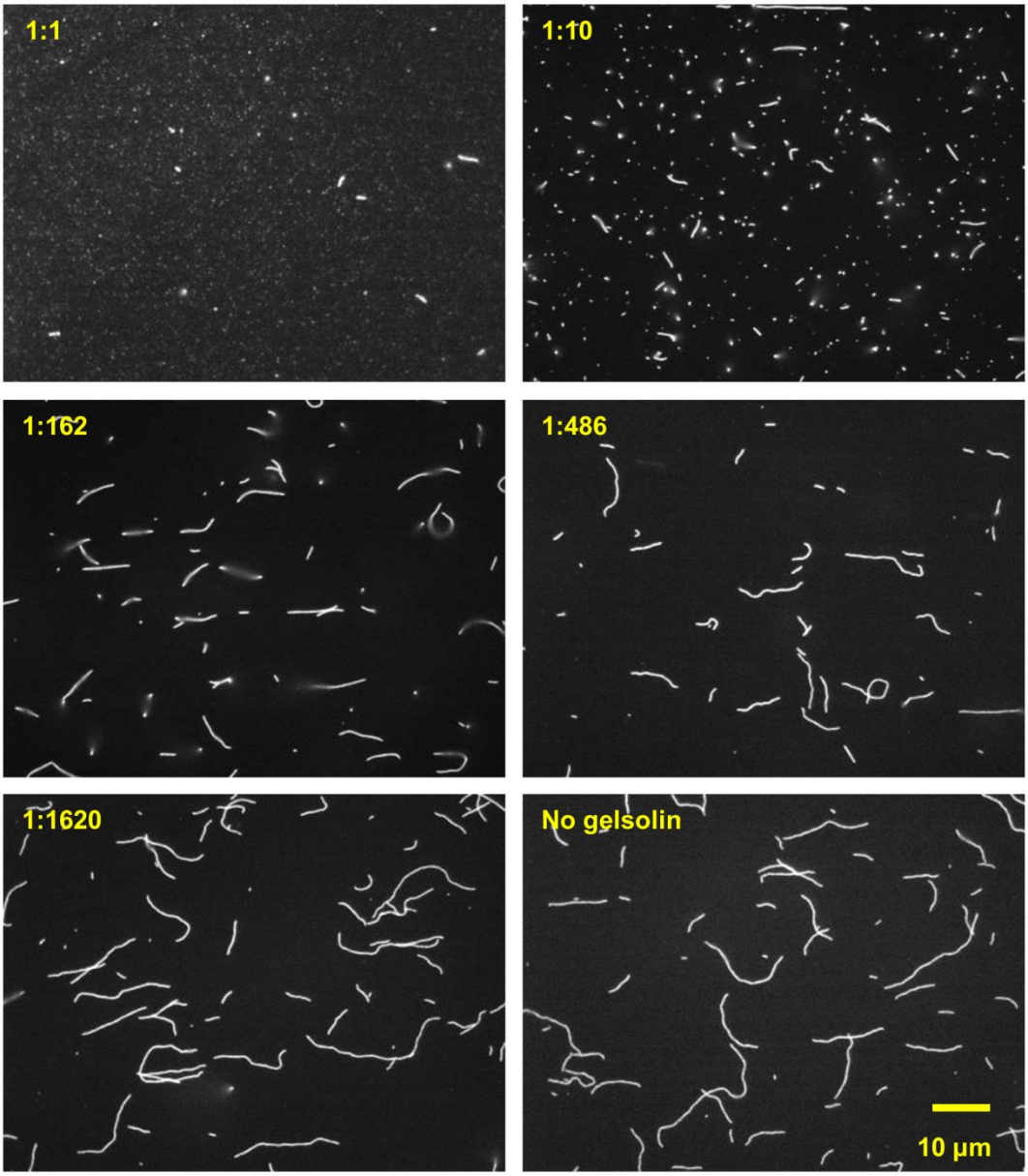

Figure 4.12 Fluorescent images showing the length of F-actin incubated with varying gelsolin concentrations. 50 µg/mL of F-actin was incubated with gelsolin in desired molar ratios for 30 min at room temperature. Then, gelsolin-actin complexes were adsorbed electrostatically on 0.0001 % PLL-coated cover slips for 10 min.

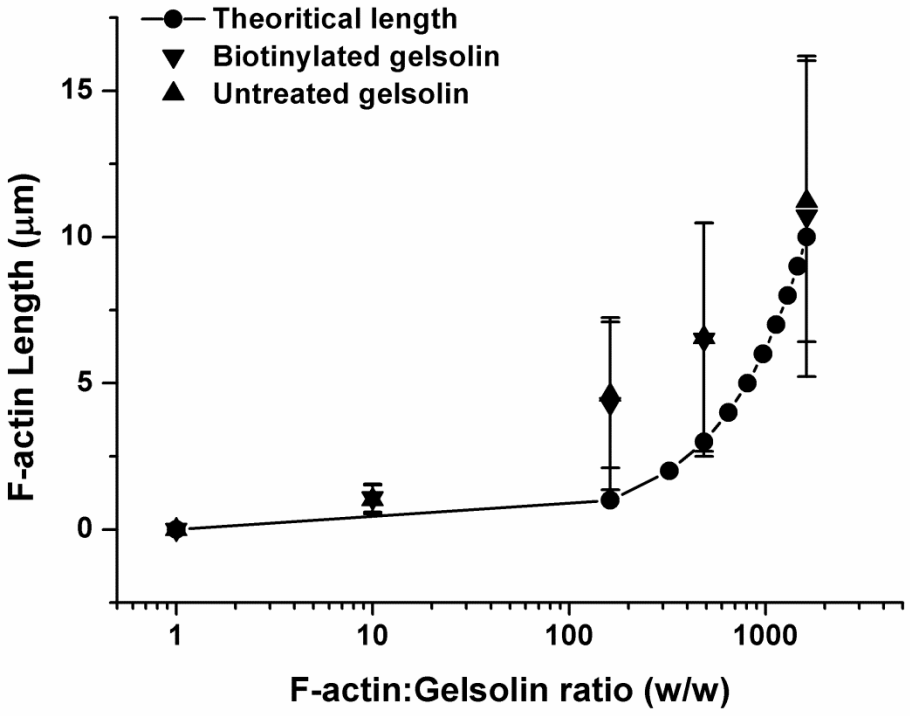

Figure 4.13 The average length of F-actin incubated with varying gelsolin concentrations. The length of F-actin incubated with 1620:1 (w/w) ratio (50:0.0309 μg/mL, F-actin:gelsolin) was similar to the length of normal F-actin. The length of F-actin decreased as gelsolin concentration increased. No fluorescent F-actin was observed at 1:1 (w/w) ratio (50:50 μg/mL, F-actin:gelsolin). For each point, 30 filaments were measured from 2 parallel experiments (n=30).

The activity of biotinylated gelsolin could also be confirmed in SEM images, as can be seen by comparison of Figure 4.14 and 4.15. After F-actin was incubated on 0.001% PLL-coated surface for 5 min, biotinylated gelsolin was followed and incubated for 30 min. As a result, shortened single actin filaments were observed. No clear observation of the presence of gelsolin at the end of F-actin occurred. This is probably due to the fact that the diameters of both gelsolin and F-actin are similar [122].

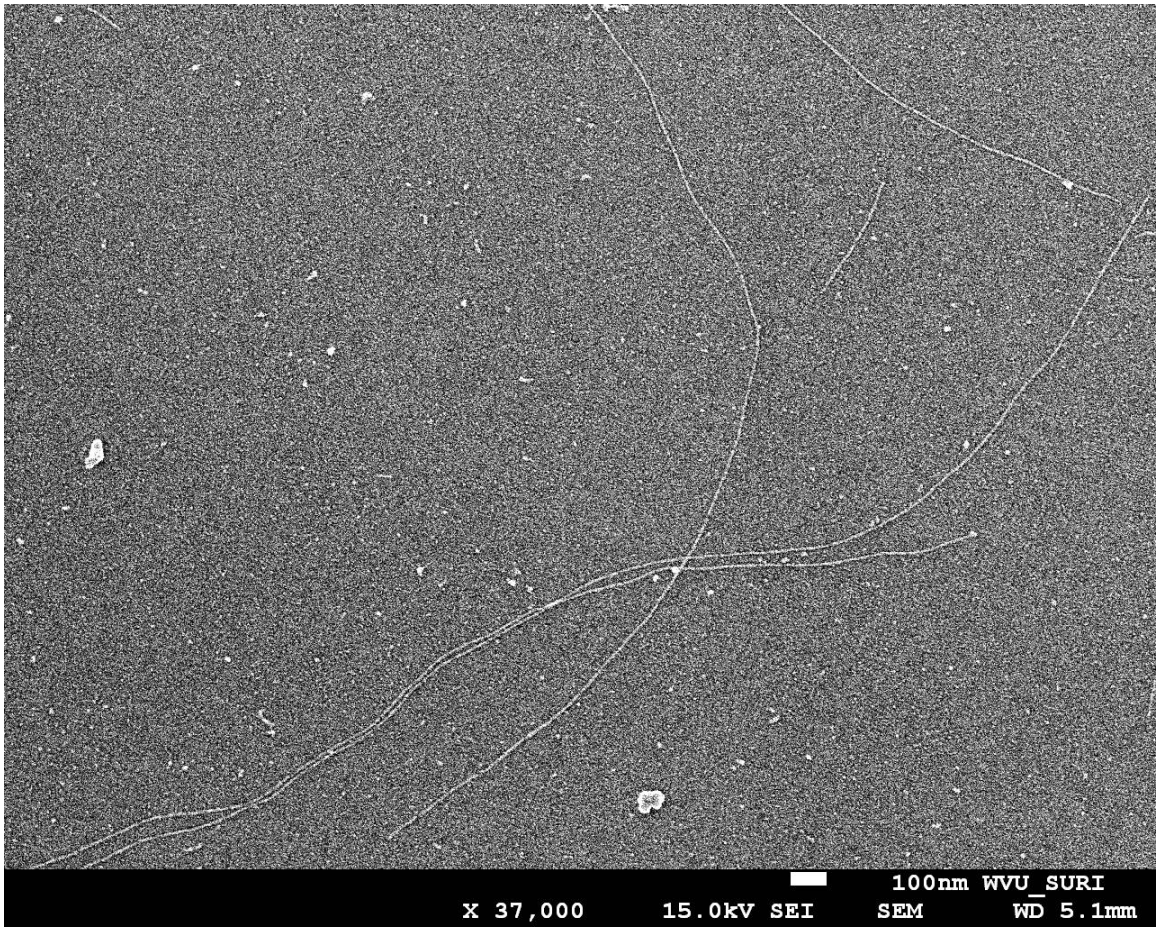

Figure 4.14 An image of single actin filaments without gelsolin. The image showed long single actin filaments.

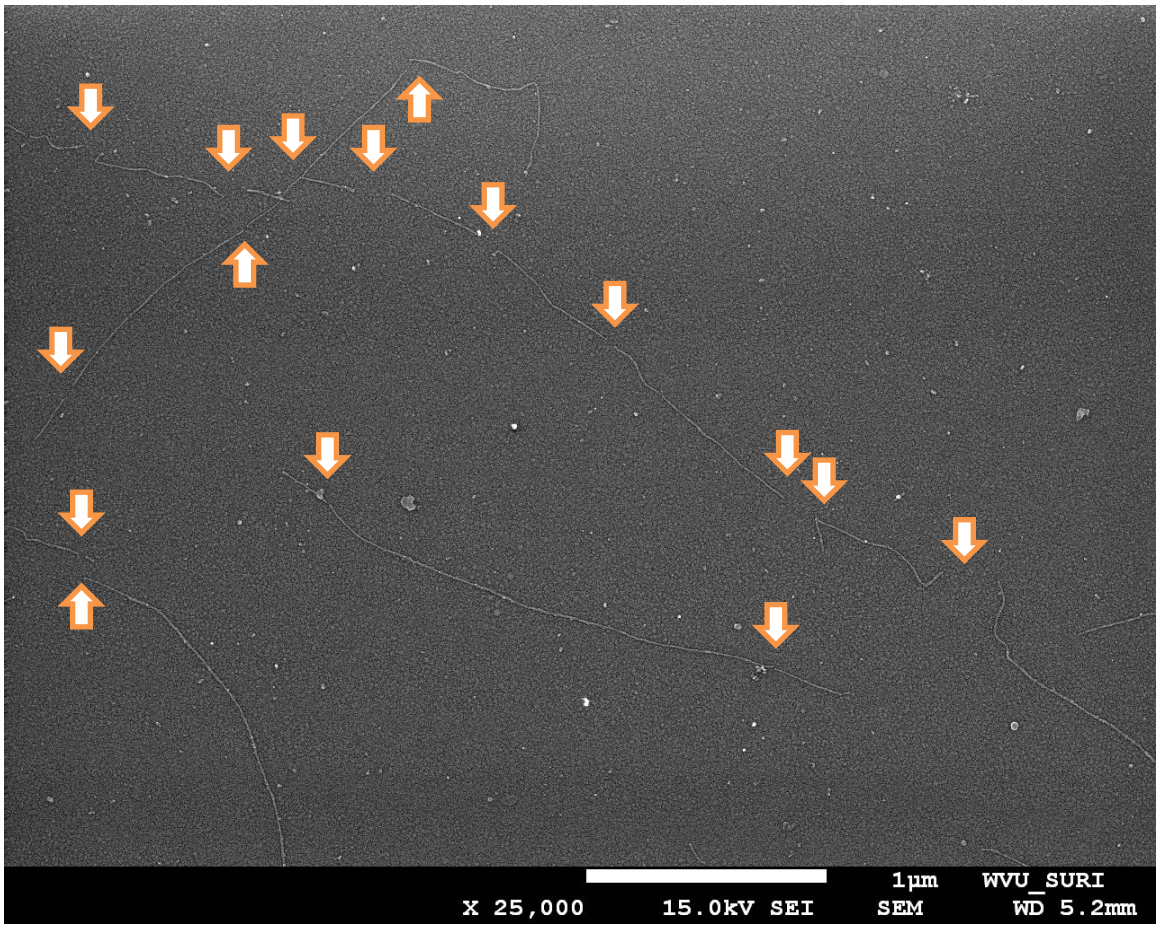

Figure 4.15 An image of gelsolin-treated single actin filaments. The image showed single actin filaments were shortened by gelsolin

4.2.3 Streptavidin-coated surface to immobilize gelsolin molecules

In order to immobilize gelsolin molecules on a surface for observation of gelsolin activity in relation to F-actin in various free Ca^{2+} concentrations, the surface was coated with streptavidin molecules. In this way, biotinlyated gelsolin molecules could bind to the surface using biotin-streptavidin interactions. The fabrication of streptavidin-coated surface is described in Chapter 3. After clean cover slips were immersed for overnight at 5% APTES in anhydrous ethanol, the primary amine groups were covalently formed on the cover slip that was confirmed using X–ray photoelectron spectroscopy (XPS). In the XPS spectra, intensities on N1s and C1s peaks of APTES-modified cover slips were dramatically increased, as

compared to ones of unmodified clean cover slips, shown in Figure 4.16. This result indicates that APTES is covalently bound to the surface of the cover slips.

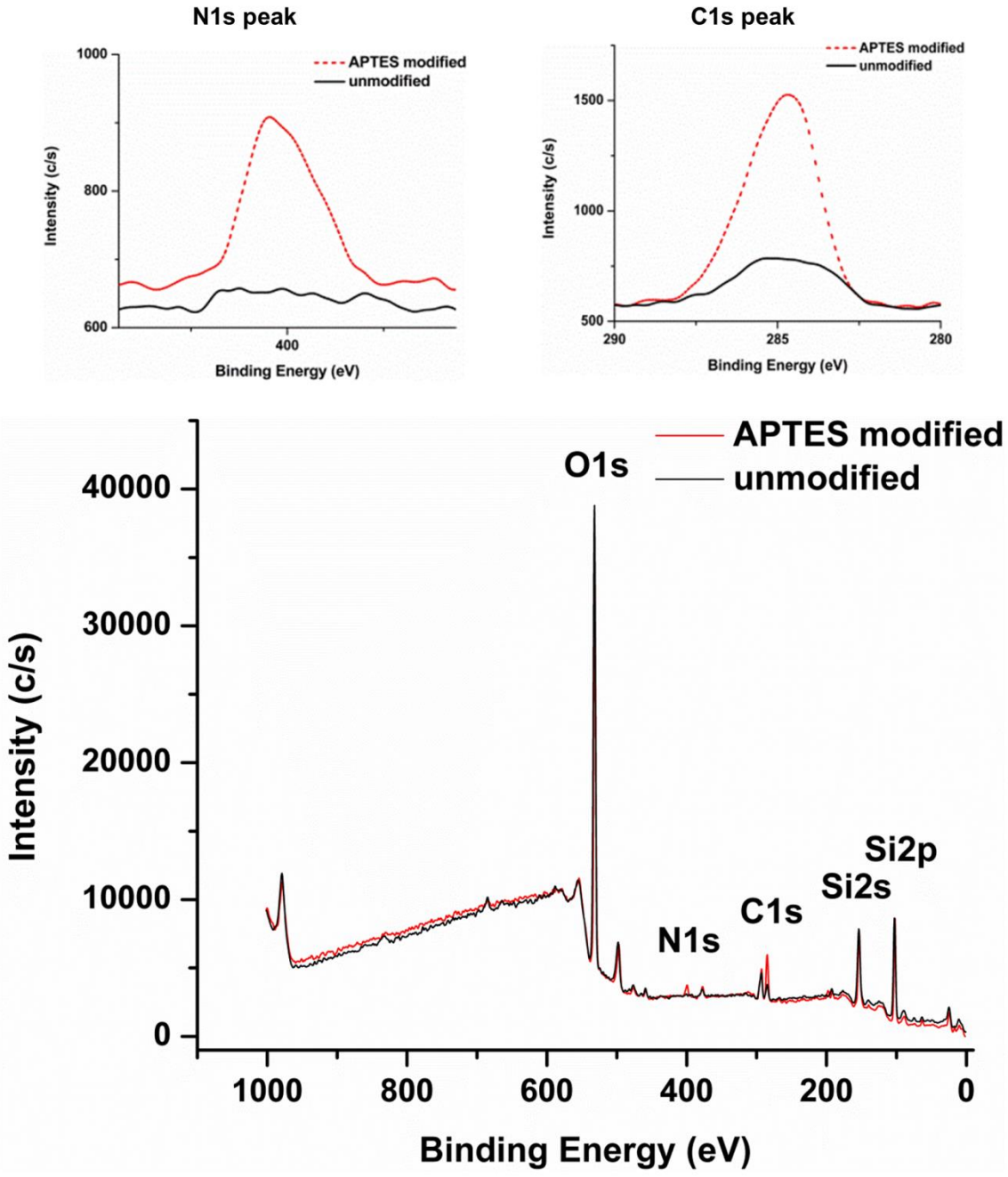

Figure 4.16 Full XPS spectra of the bare and APTES-modified cover slips. A dramatic increase of both N1s and C1s peaks on the APTES-modified cover slips were observed, as compared to peaks on unmodified clean cover slips.

The intensity increase on N1s and C1s peaks indicates that APTES is covalently bound to the surface of the glass slide. After the survey scan, narrow scans for N1s and C1s were recorded.

The APTES-coated surface was biotinylated using 1 mg/mL of NHS-PEG_4-biotin in DMF. Subsequently, DyLight 488 conjugated streptavidin in B-PBS buffer was incubated for 1 h. As a result, streptavidin molecules were immobilized on the surface as shown in Figure 4.17.

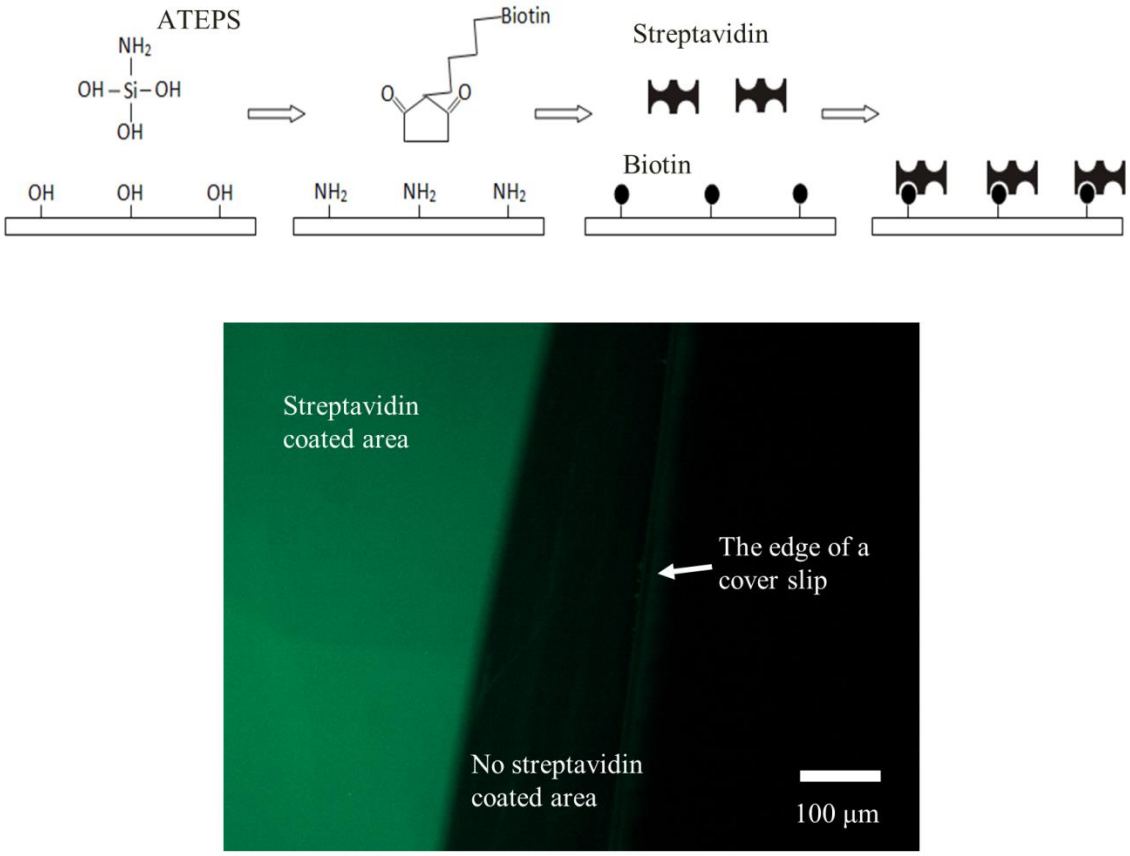

Figure 4.17 Fluorescent image of streptavidin-coated surface. Fluorescent-dyed streptavidin solution was washed away after 1 hour of incubation in flow cell. Fluorescent light was found on biotinylated surface while no fluorescent light was emitted on non-biotinylated surface. (Bar size is 100 μm)

Optimal streptavidin concentration was investigated prior to fabricating streptavidin-coated surfaces. 0, 0.1, 1, 10, 100, and 200 μg/mL of streptavidin in B-PBS buffer were incubated on biotinylated surface, and their fluorescence intensities were measured. As shown in Figure 4.18, the fluorescence intensity was

already saturated at 10 μg/mL of streptavidin. To ensure the saturation of streptavidin molecules on the surface, 100 μg/mL of streptavidin was used through all experiments unless otherwise specified.

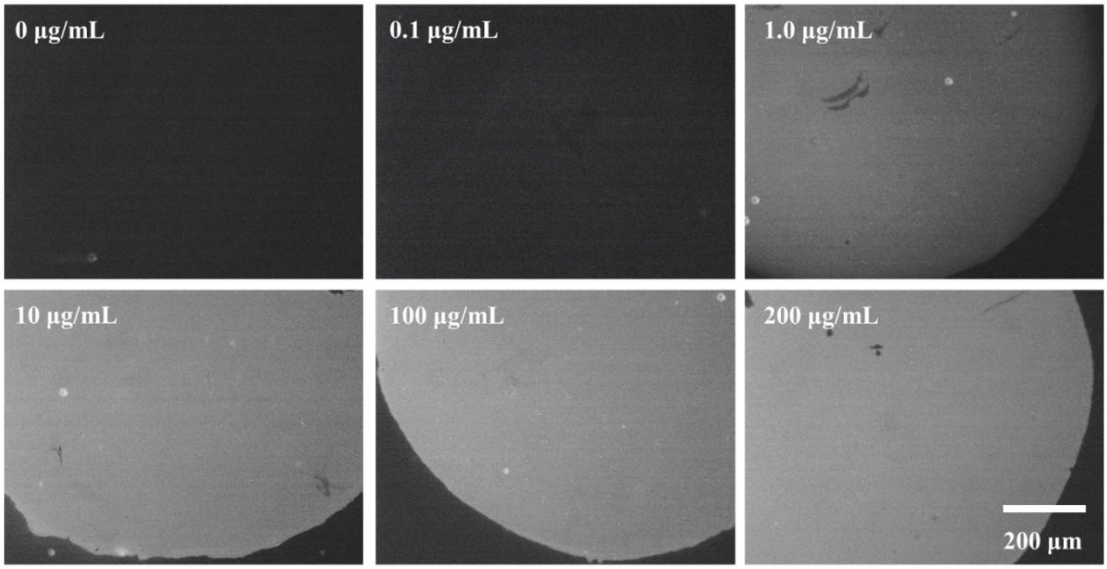

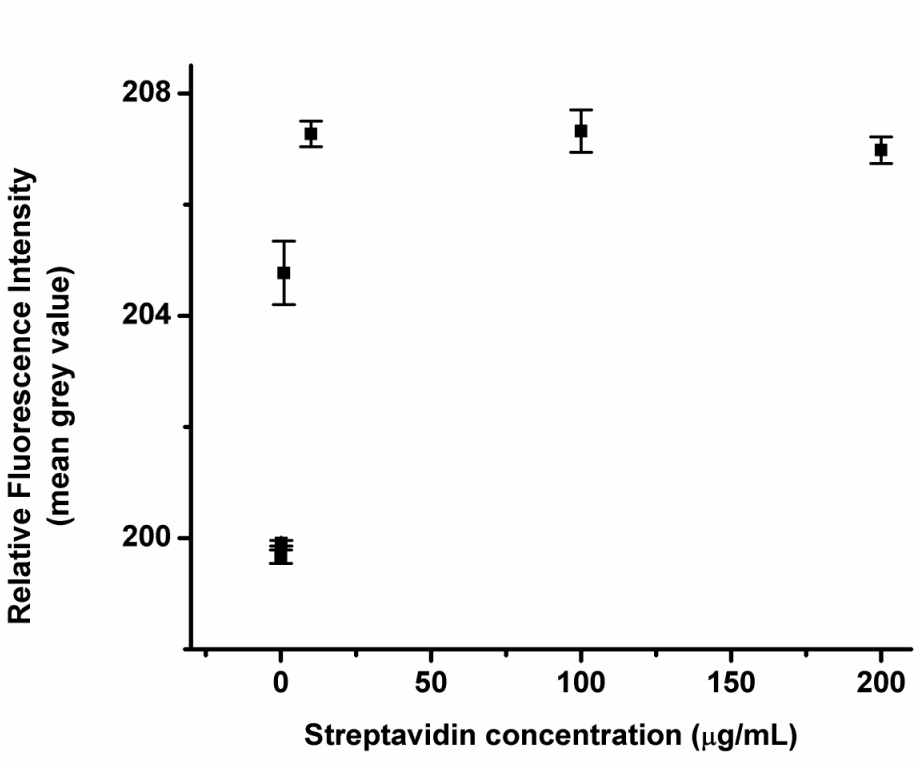

Figure 4.18 Fluorescence intensities of various streptavidin concentrations. 0, 0.1, 1.0, 10, 100 and 200 μg/mL of streptavidin in B-PBS buffer were incubated on biotinylated surfaces using homemade PDMS chips. After 30 min incubation, streptavidin solutions were rinsed away with B-PBS buffer, and the fluorescence intensities of each streptavidin concentration were measured using area analysis in Wasabi software. The fluorescence intensity was saturated after 10 μg/mL of streptavidin (n=3).

4.2.4 Blocking of non-specific binding of F-actin

Before building up a system for observation of F-actin interacting with gelsolin, it is necessary to ensure that non-specific binding sites on the surface are sufficiently blocked using blocking agents. Milk protein based blocking agents that include nonfat powered milk or casein may contain some endogenous biotin. Thus, bovine serum albumin (BSA) is preferred for an assay using a biotin-streptavidin system [123]. Tween-20 (T-20) is often used alone or with other proteins as a blocking agent in enzyme-linked immunosorbent assay (ELISA) or Western blots [124]. Therefore, T-20 and combinations of BSA and T-20 were investigated as blocking agents to find the most effective method to block non-specific binding sites.

Various combinations of BSA and T-20 were incubated on biotinylated surface for 2 hours with one time refreshment of blocking agents after 1 hour. After incubation, 0.25 μg/mL of F-actin solution was added and incubated for 30 min to facilitate the display of non-specific binding of F-actin on the surface. The rate of non-specific binding of F-actin is plotted with respect to different blocking agents as shown Figure 4.19. Our results indicated no significant blocking effect with 0.05 % T-20 alone. However, T-20-containing buffer exhibited a better washing effect when unattached F-actin was removed. This may suggest that combinations of blocking agents can be more effective for our assay. Non-specific binding was decreased as BSA concentration increased. Blocking effect became saturated at more than 3 % BSA with 0.05 % T-20. Based on the results, 5 % BSA with 0.05 % T-20 was chosen for the most effective blocking of non-specific binding of F-actin.

After non-specific binding sites were blocked, 0.1 mg/mL of streptavidin was incubated on biotinylated surface to facilitate the production of the surface-biotin-streptavidin-biotin-gelsolin sequence. Another blocking agent incubation was also performed between streptavidin and biotinylated gelsolin incubation, producing an enhanced blocking effect of non-specific binding of F-actin on streptavidin-coated surface (*triangles*).

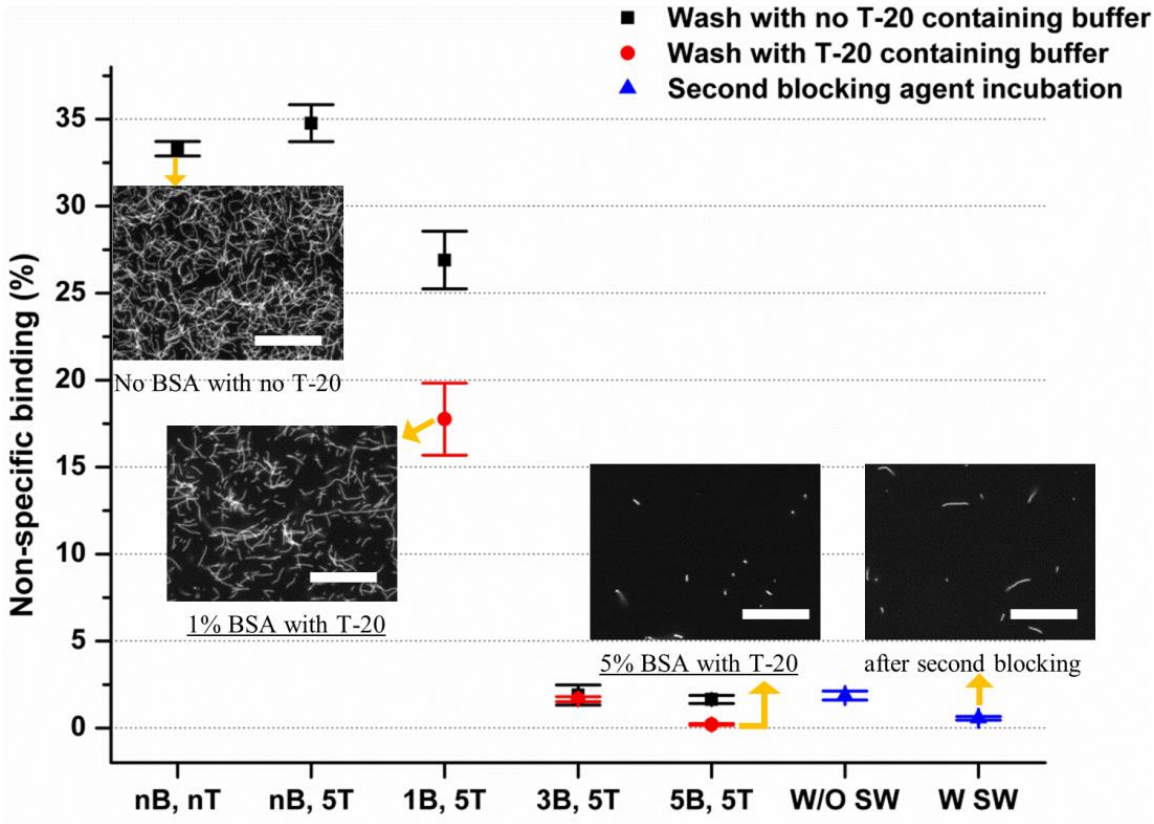

Figure 4.19 Non-specific binding of F-actin on biotinylated surface after incubation with blocking agents: no BSA with no T-20 (nB, nT), no BSA with 0.05 % T-20 (nB, 5T), 1 % BSA with 0.05 % T-20 (1B, 5T), 3 % BSA with 0.05 % T-20 (3B, 5T), and 5 % BSA with 0.05 % T-20 (5B, 5T). Squares indicate non-specific binding after washing with a buffer containing no T-20. Circles indicate non-specific binding after washing with a buffer containing T-20. Images, showing the non-specific binding of F-actin on the surface after washing with a buffer containing T-20, are distinguished with underlined text. No significant blocking effect occurred with 0.05 % T-20 alone. However, T-20-containing buffer exhibited better washing effect when unattached F-actin was removed. Non-specific binding was decreased as BSA concentration increased and blocking effect was saturated at more than 3 % BSA with 0.05 % T-20. Triangles indicate the effect of the second blocking agent incubation on non-specific binding of F-actin. In the presence of the second blocking agent incubation between streptavidin and biotinylated gelsolin incubation, non-specific binding of F-actin on streptavidin-coated surface was significantly decreased. For each point, 6 fields were randomly selected and measured from 2 parallel experiments (n=6). (Bar size is 20 μm)

4.2.5 Observation of gelsolin activity in various concentrations of free Ca^{2+} ions

When suspended F-actin is in contact with gelsolin immobilized on the surface, F-actin is severed and remains bound to the surface while gelsolin caps the freshly cut barbed end of F-actin in the presence of free Ca^{2+}. Once F-actin is capped by gelsolin on the surface, it is not easily released despite the reduction of free Ca^{2+} using EGTA as a chelating agent [116]. Thus, the coverage of F-actin or the number of bound F-actin on the surface can be utilized as an indicator of activity of individual gelsolin.

Figure 4.20 and 4.21 display the coverage of F-actin as a function of free Ca^{2+} concentration. Figure 4.20 shows fluorescent images of F-actin on gelsolin-immobilized surface as the function of free Ca^{2+} concentration. Data indicates that the coverage of F-actin on the surface increases as free Ca^{2+} concentration increases. In Figure 4.21, analysis of the data with a logistic function suggests the half-maximal coverage of F-actin occurs at 2.9 μM free Ca^{2+}. Figure 4.21 indicates that there are three distinct steps of gelsolin activation in various free Ca^{2+} concentrations. No significant difference of F-actin coverage occurred between zero free Ca^{2+} and 10 nM free Ca^{2+}. It is interpreted that no gelsolin activity occurred at less than 10 nM free Ca^{2+}. This result, observed in the inactive state, is consistent with previous reports [111, 119, 125, 126]. In the intermediate state, the coverage was proportional to the increase of free Ca^{2+} concentration up to ~100 μM. Finally, the coverage was saturated at more than 200 μM of free Ca^{2+}, called the active state. This result suggests that the number of activated gelsolin is proportional to the increase of free Ca^{2+} concentrations. The result provides an insight on gelsolin activation in relation to F-actin in various free Ca^{2+} concentrations.

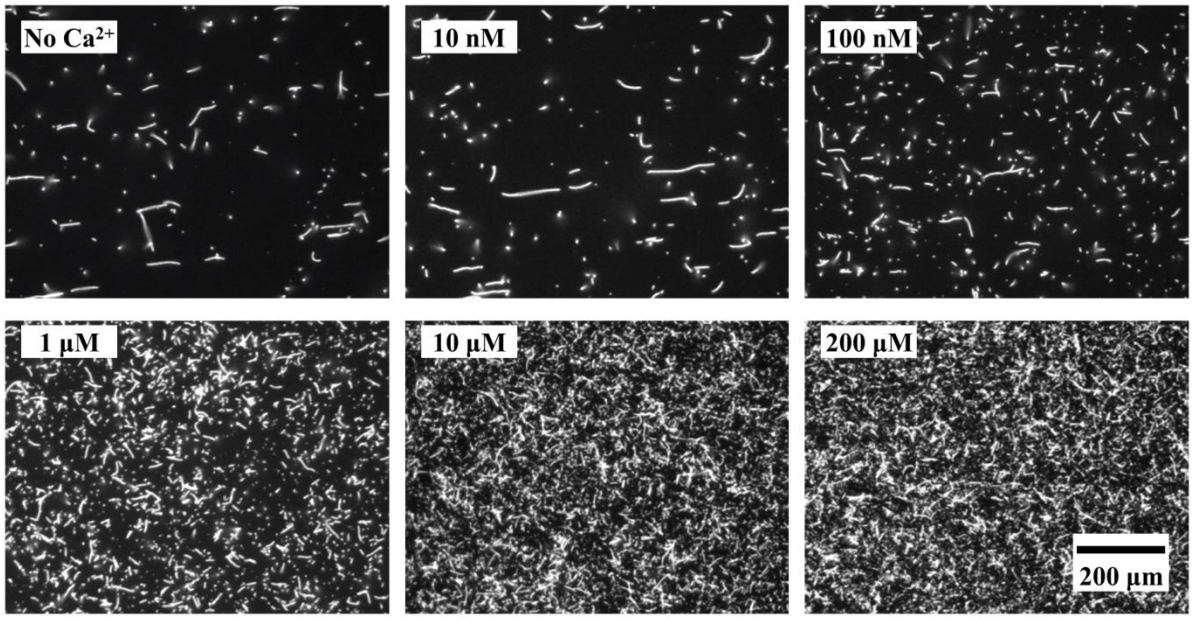

Figure 4.20 Fluorescent images of F-actin binding on gelsolin immobilized surface in various concentrations of free Ca^{2+} ions. Images show the coverage of F-actin on the surface increases as free Ca^{2+} concentration increases.

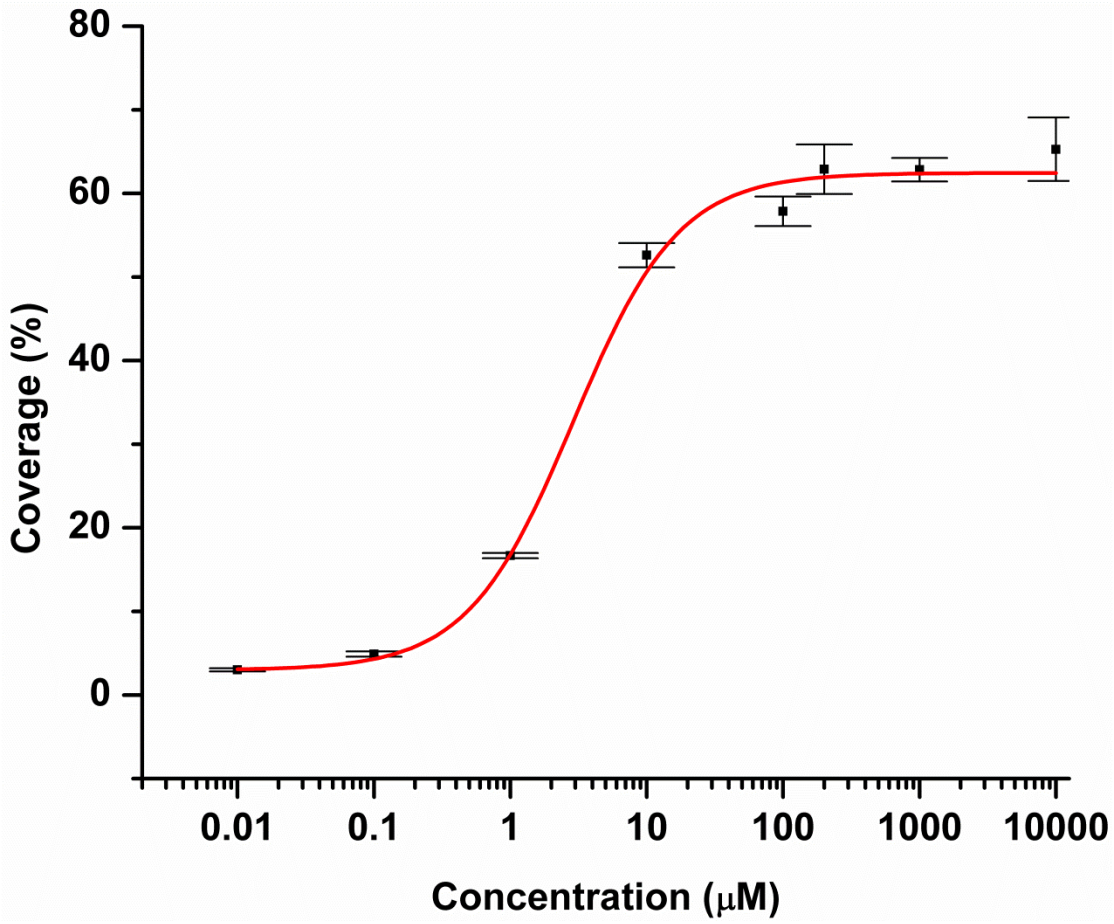

Figure 4.21 A graph showing F-actin coverage in various free Ca^{2+} concentrations. As free Ca^{2+} concentration increasing, the number of F-actin on the surface increases, and the length of F-actin decreases. A logistic equation was used to fit the data. Half-maximum of F-actin coverage occurred at 2.9 (±0.3) μM of free Ca^{2+} concentration. For each point, 6 fields were randomly selected and measured from 2 parallel experiments (n=6).

A variety of studies have found that higher Ca^{2+} concentrations are required to promote F-actin binding. Initial conformational change of gelsolin, which is thought to allow F-actin binding site in G2 to be exposed on contact with F-actin, occurs at nanomolar concentrations [106, 107, 118]. This finding is consistent with our data. No noticeable coverage of F-actin was observed in less than ~100 nM of free Ca^{2+} while significant binding of F-actin occurred at higher free Ca^{2+} concentrations. Furthermore, our data suggests that severing and capping activities of full-length gelsolin are followed without an

additional Ca^{2+} binding after gelsolin binds to the side of F-actin. The F-actin binding activity of gelsolin is thought to occur at lower Ca^{2+} concentrations than ones required for severing and capping of F-actin [111, 114]. However, no observation occurred for binding to F-actin only. Most F-actin was severed and remained bound to the surface during experiments.

If additional Ca^{2+} binding is a necessary condition for severing and capping of F-actin after gelsolin binds to the side of F-actin, then one should expect a large coverage of long F-actin held by gelsolin will be observed in certain free Ca^{2+} concentrations during the intermediate state. However, in our data few full-length F-actin were observed when gelsolin was in the inactive state only, which probably occurred due to non-specific binding. It has been reported that isolated G1-3 binds to F-actin. Severing and capping of F-actin subsequently occur, even in the absence of free Ca^{2+} [106]. In other words, G4-6 may regulate gelsolin activity in Ca^{2+}-dependent manner [101]. Thus, accumulated evidence with our data suggests that once the regulation for the activation of G1-3 is removed by binding Ca^{2+} ions on G4-6, gelsolin is activated in order to bind to F-actin and subsequently sever and cap F-actin without additional Ca^{2+} ions.

The half maximal F-actin binding of gelsolin is known to occur at ~100 nM [111]. This may imply that the full activation of gelsolin is able to occur at lower free Ca^{2+} concentrations than known. However, the activation rate of gelsolin may be slower in lower free Ca^{2+} concentrations, while high free Ca^{2+} concentrations may promote activation rate of gelsolin [100, 109].

4.2.6 Conclusion

In the present study, we adopted surface technique into the observation of gelsolin activity basing on the coverage of surface-bound F-actin. For clear observation, non-specific binding of F-actin was sufficiently resisted by the blocking agent, 5% BSA with 0.05% T-20 in B-PBS buffer. The measurement of the length of F-actin, which was performed with actin-gelsolin mixtures at varying ratios, provides verification of the activity of gelsolin after biotinylation.

In the gelsolin activation experiment, our data suggest half-maximal activation of gelsolin occurs at 2.9 μM. Moreover, the data shows three activation states of gelsolin, as illustrated in Figure 4.22. No gelsolin activity was observed at less than 10 nM free Ca^{2+} and the number of activated gelsolin increased with increasing free Ca^{2+} concentration in a range from ~10 nM to ~100 μM. Finally, the number of activated gelsolin was saturated at ~200 μM free Ca^{2+} or above.

No observation occurred of full-length F-actin covering on gelsolin immobilized surface, but F-actin became shorter as the number of F-actin increased on the surface. This may suggest that severing and

capping F-actin are followed without additional Ca^{2+} ions after binding of full-length gelsolin to the side of F-actin.

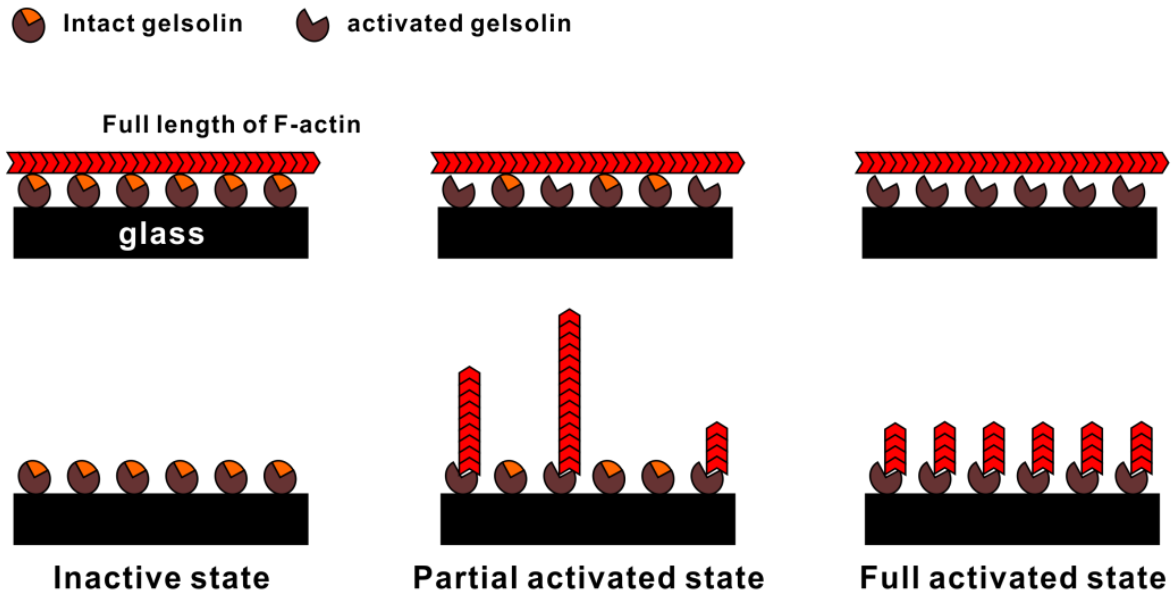

Figure 4.22 Illustration describing the interaction between F-actin and gelsolin immobilized on the surface in various free Ca^{2+} concentrations. No significant binding of F-actin occurs in less than 10 nM, where no gelsolin is activated (left). As the number of activated gelsolin increases with free Ca^{2+} ions, the number of bound F-actin increases up to ~100 μM (center). The number of activated gelsolin is saturated at more than 200 μM (right).

4.3 Motility on PLL-coated polystyrene particles

Before unipolar actin arrays were created, the observation of HMM-coated particle movement was attempted on random oriented F-actin arrays bound to PLL-coated surface. The random oriented F-actin arrays were formed as F-actin was incubated on PLL-coated surface. Due to electrostatic interactions between F-actin and PLL, F-actin was immobilized on PLL-coated surface. This earlier approach was designed to verify what functionalized particles support actomyosin motility. Various different particles such as polystyrene particles, PLL-coated particles, amino functionalized particles, tosyl-activated particles were investigated, but no movement except Brownian motion was observed.

Since the random oriented F-actin arrays could be a factor preventing the movement of HMM-coated particles, the demand for developing a new methodology was raised. Development of a new methodology will benefit the investigation of actomyosin motility on various particles which have different surface properties.

To investigate actomyosin motility on the surface of particles, a layer of particles will form on the surface of the glass slide. HMM will be adsorbed to the surface of the particles, and F-actin movement will be observed on it. For our first attempt, PLL-coated polystyrene particles were chosen because 1) PLL is a widely used material to aid protein adsorption on the surface, 2) bead assay using PLL-coated particles is already shown [127] and 3) successful gliding assay of actomyosin is demonstrated on PLL-coated glass slide. To enhance PLL coating on the particles, carboxylated particles (Spherotech Inc.) which have negative surface charges were employed. The particles were incubated in 0.01% of PLL solution for overnight and washed with DI-water using a centrifuge before use.

When the particle solution was incubated on the glass slide, a PDMS chip was used to prevent spreading the particle solution during incubation. The surface of glass was treated with oxygen plasma so that electrostatic interaction between the hydroxyl group-formed glass surface and PLL-coated particles occurred, as shown in Figure 4.23. This treatment helped prevent the detachment of particles from the surface during the process. After accumulation of particles on the surface, unnecessary PLL molecules and unbound particles were removed with DI-water. DI-water on particle layers was dried using N_2 gas. The population of particles on the surface was controlled by a function of incubation time. Avoiding a dense particle layer allowed more accurate observation of F-actin movement on the particle surface.

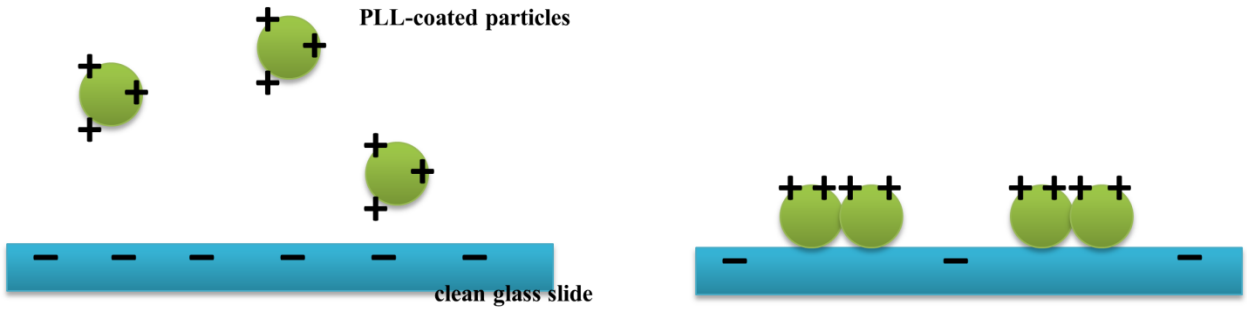

Figure 4.23 Illustration of forming the PLL-coated particle layer on a clean glass surface. PLL-coated particles were electrostatically bound to the clean glass surface.

Motility assays were conducted on PLL-coated 0.5 μm diameter carboxylated polystyrene particle layers. Motility is sensitive to temperature so room temperature was maintained at 24 ℃ (±1 ℃) for all experiments related to motility. The measurement of motility movement was conducted using the manual tracking program in ImageJ. For motility assays, a flow cell (10 mm × 18 mm × 0.156 mm) was built up of two double tapes as spacers and a cover slip (18mm × 18mm with No.1 thickness, Corning Inc.) on particle-deposited glass slide. The flow cell was incubated with 0.1 mg/mL of HMM for 5 min, and 1 mg/mL bovine serum albumin (BSA) was followed to prevent non-specific binding of F-actin on the surface. After 5 min, the flow cell was washed out by M-buffer (25 mM KCl, 2 mM $MgCl_2$, 0.2 mM $CaCl_2$ and 25 mM imidazole at pH 7.0). Actin solution, composed of 0.25 μg/mL fluorescent F-actin, 1.5 mM ATP, 10 mM dithothreitol, 0.22 mg/mL of glucose oxidase, 3.6 mg/mL of catalase and 450 mg/mL of glucose in M-buffer, was introduced into the flow cell. The movement of F-actin on the particle surface was observed using a fluorescence microscopy.

Most F-actin found near the surface was bound to the particle surfaces and showed motilities around particles. No movement of F-actin was found except on particle surfaces. Figure 4.24 shows tracking results of F-actin movement on the particle layer. The dark grey indicates the particle layer, while the light grey indicates a bare surface. F-actin moved along the particle layer. However, if the gap between particles was sufficiently narrow, F-actin could jump. This effect may have occurred because the tip of F-actin found the next available HMM molecule before F-actin was diffused into the medium. Figure 4.25

shows average velocities of F-actin measured on the particle layer. When measuring the velocity of F-actin on the particle layers, the average velocity was as slow as approx. 0.3 μm/s. This slow movement, as compared to F-actin on PLL-coated or colloidin-coated glass slides, was because F-actin showed stop-and-go movement, rather than continuous movement. This stop-and-go movement might be due to the roughness of the particle layer, which may cause a delay of seeking next HMM required for continuous movement. This hypothesis is reasonable since the average velocity of continuous movements more than 5 seconds was approx. 0.92 μm/s, which was similar to the average velocity of F-actin gliding on PLL-coated flat glass surface. This similarity means PLL-coated carboxylated particles may support actomyosin motility as much as PLL-coated glass slide does. Supporting actomyosin motility on PLL-coated particles was more apparent when using larger particles (e.g. particles more than 4 μm in diameter), where roughness of the layer can be ignored.

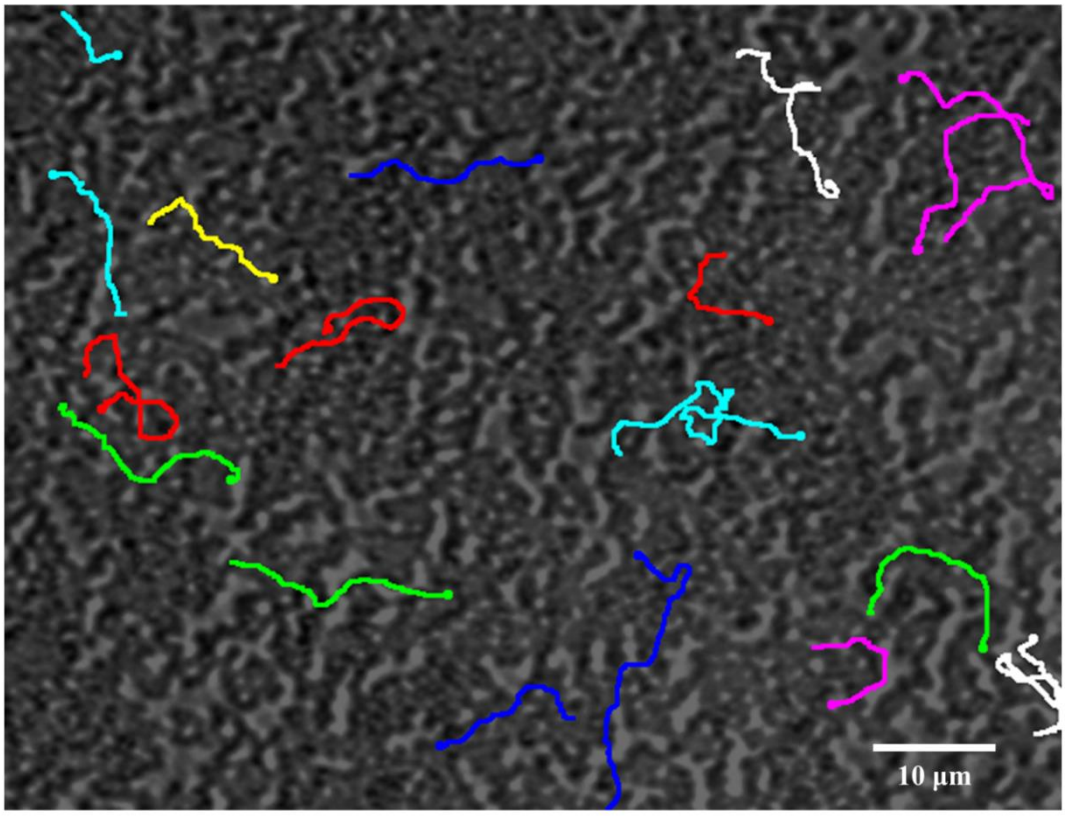

Figure 4.24 Tracking F-actin movement on the particle layer. Dark grey indicates the particle layer while light grey indicates a bare surface. No movement of F-actin was found on a bare surface.

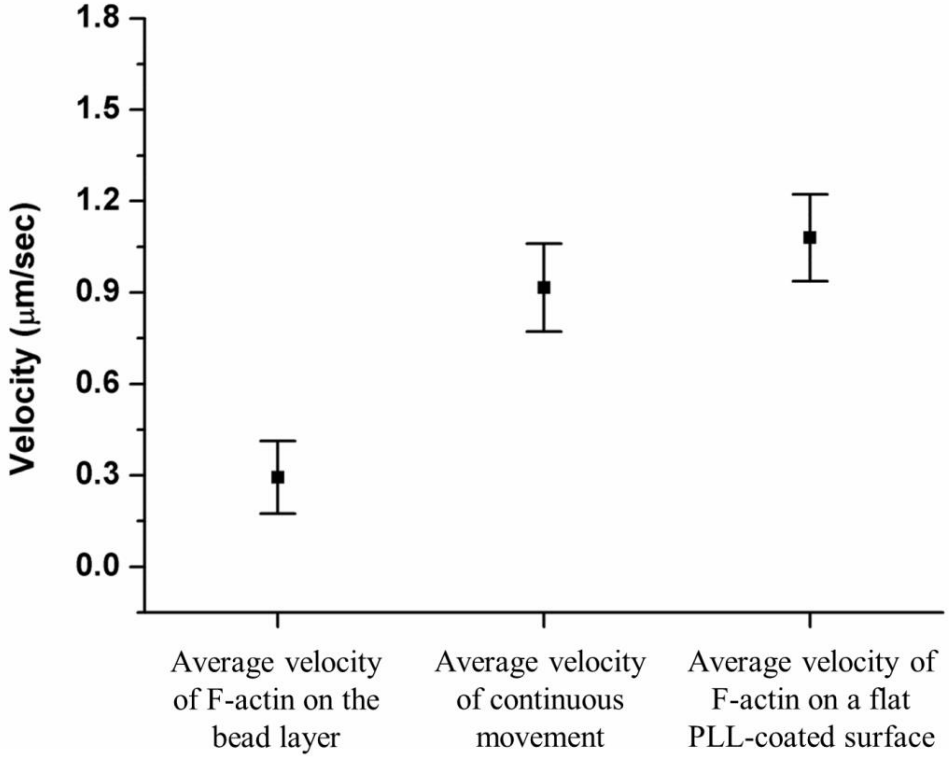

Figure 4.25 Average velocities of F-actin movement on PLL-coated particle layer. When measuring the velocity of F-actin on the particle layers, the average velocity was as slow as approx. 0.3 μm/s. The slow movement might be due to the roughness of the particle layer since the roughness might cause a delay of seeking next HMM required for continuous movement. The average velocity of continuous movements more than 5 seconds was approx. 0.92 μm/s, which was similar to the average velocity of F-actin (1.08 μm/s) gliding on PLL-coated flat glass surface.

Other particles including amino functionalized particles and tosyl-activated particles were investigated with a similar method. Tosyl-activated particles were used for bead assays somewhere else [128]. However, no F-actin movement on their surfaces was observed. On amino-functionalized particle layer, F-actin movement was found, but the results were not constant. To conclude, this experiment suggests that HMM can be adsorbed properly on PLL-coated particles to support F-actin movement. Also, the experiment suggests random oriented F-actin arrays may not be able to carry out HMM-coated particle

motility. In other words, when F-actin arrays are aligned with structural polarity, unidirectional transport of HMM-coated particles can be achieved using PLL-coated particles.

4.4 Unidirectional transport by HMM-coated particles

In eukaryotic cells, various types of motor proteins exist in order to carry out diverse biological motilities, from the transport of intracellular cargoes (e.g. vesicles, organelles, or chromosomes) [129, 130] to muscle contraction [40, 131]. Although each type of motor proteins has a different structure [2], the motor domain of motor proteins hydrolyzes adenosine triphosphate (ATP) to create mechanical energy [132, 133]. By means of this highly efficient chemomechanical transduction, motor proteins are able to perform mechanical movements along cytoskeletal tracks in a directed manner, and their mechanisms are precisely regulated. These unique mechanical characteristics of motor proteins—high efficiency, directionality, and controllability—have attracted interest in the fields exploring the development of a nanoscale transport or actuation system. Since creating such systems has been technically limited, harnessing motor proteins, especially the kinesin and myosin families, in synthetic environments has been investigated over the past decade [1, 57, 134].

In utilizing motor proteins for bionanotechnological applications, the ability to control the direction of the movement resulting from interactions between motor proteins and their associated filaments is critical. While many cellular functions are sophisticated and performed primarily at nanoscale, these functions are precisely controlled by cellular signals within cells. For instance, monomeric subunits of filaments are dynamically assembled and dissembled by such cellular signals in order to provide tracks for motor proteins. These tracks play critical roles in biological movement and transport [135-137]. Since there are technical limitations on completely mimicking cellular manipulation and mechanics *in vitro*, alternative methods have been proposed and investigated for directional control of motor proteins [3, 4, 6, 75, 77, 79-81, 83, 138-140].

There are two types of *in vitro* motility assays: the gliding assay and the bead assay [57]. In the gliding assay, cytoskeletal filaments are propelled by motor proteins bound to the surface, and the motion of cytoskeletal filaments is in a Brownian movement [56]. Therefore, external influences such as DC electric fields [3], AC electric fields [4, 138], or engineered tracks [6, 75, 77, 79-81, 83, 139, 140] are required in order to gain directional control of the cytoskeletal filaments. In contrast, the bead assay involves immobilizing cytoskeletal filaments on the surface in order to guide the motion of motor proteins. This assay is analogous to cellular systems, in which cytoskeletal filaments serve as tracks for motor proteins. Creating unipolar filament arrays is the key to directional transport in this assay. This approach is well established in kinesin-microtubule based studies, which involve chemically immobilizing the microtubules after they are oriented along flow fields [87, 89] or using proteins binding to a specific end of microtubule in order to orient the polarity [141, 142]. In actin-myosin based bead assays, the first

oriented assembly of actin filaments (F-actin) was formed on avidin-immobilized surface using severin and flow fields, where the motility of myosin-coated beads had been demonstrated [55]. However, in that study, a few of the beads moved for relatively short distances while a number of beads remained stationary. Moreover, a continuous flow field had to be present during the assay in order to maintain the alignment of the arrays [56]. A recent study has demonstrated the motility of processive myosin motor proteins on chemically immobilized, oriented F-actin [143], but currently no reports exist on artificial actin tracks, which support long-range, steady transport of myosin-bound beads.

In the present study, a method of creating unipolar actin arrays is introduced to facilitate unidirectional transport of beads coated by heavy mermomyosin (HMM). The method involves anchoring the barbed end of F-actin on a streptavidin-coated surface through biotinylated gelsolin and crosslinking F-actin aligned along a flow field using fascin. These precisely oriented F-actin arrays provide unidirectional transport of HMM-coated polystyrene beads over distances of up to several hundred micrometers. The advantages of this method are that: 1) no external regulation and influence is required to guide the HMM-coated beads or maintain the F-actin arrays, 2) a linear transport of beads to desired locations can be accomplished, and 3) patterned tracks of F-actin arrays constructed using micropatterning techniques are available for various applications.

4.4.1 Unipolar fascin crosslinked F-actin arrays

The concept of building unipolar F-actin arrays is illustrated in Figure 4.26. The procedure of streptavidin-coated surfaces is described in Chapter 3. Briefly, the surface of a cover glass is modified with 5% APTES in anhydrous ethanol for covalent coupling of NHS-PEG_4-biotin. A flow cell (2 mm (W) × 18 mm (L) × 0.18 mm (H)) was built from the biotinylated cover glass (top) and a clean glass slide (bottom), separated by two double-sided tapes. The streptavidin coating is performed with incubation of 0.1 mg/mL streptavidin in the flow cell (Figure 4.26A). The incubation of F-actin and biotinylated gelsolin solutions is performed immediately before introducing into the flow cell, which resulted in biotinylated gelsolin-actin (bGA) complexes. When bGA complex solution is introduced through the flow cell, the barbed end of F-actin is anchored onto the streptavidin-coated surface, which is a way to control the polarity of the arrays (Figure 4.26B). Once the proper population of F-actin is formed on the surface, a flow field is utilized to lay down F-actin aligned along the direction of the flow, while the flow solution contains immobilizers to prevent F-actin resuspension (Figure 4.26C).

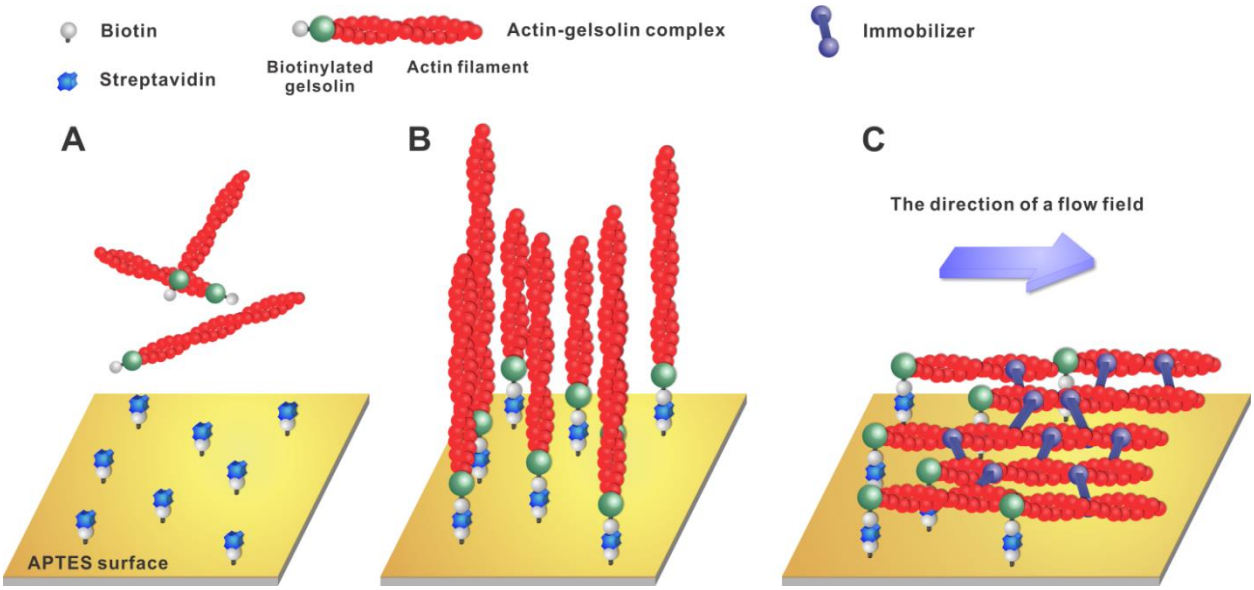

Figure 4.26 Schematic representation of building unipolar F-actin arrays on a glass substrate. (A) Streptavidin-coated surface. A clean cover slip is immersed in 5 % APTES solution. APTES-coated surface is biotinylated with NHS-biotin, and streptavidin is followed for 1 hour. (B) Biotinylated gelsolin-actin complexes. Gelsolin is biotinylated before mixing with F-actin. The average length of F-actin in biotinylated gelsolin-actin complexes can be varied according the molar ratio of gelsolin and F-actin. (C) Immobilization of F-actin with structural polarity. After the sufficient population of F-actin is formed on the streptavidin-coated surface, a flow field containing immobilizers is introduced to create unipolar actin arrays.

In building unipolar F-actin arrays, a couple of issues needed to be resolved. When bGA complexes were introduced on the streptavidin-coated surface, non-specific binding sites yielded undesired binding of F-actin. Therefore, these sites had to be blocked prior to incubating the bGA complexes. Otherwise, bipolar or disordered F-actin arrays might form causing HMM-coated beads to move only for short distances or remain stationary. For a blocking solution, 5 % BSA with 0.05 % T-20 in B-PBS buffer was applied for 1 hour before and after streptavidin incubation as described in Chapter 3. After the surface was appropriately treated with the blocking solution, bGA complexes were introduced at 0.28 mm/s for 30 m. It was found that no significant non-specific binding of F-actin occurred, as shown in Figure 4.27A. Most F-actin was suspended near the surface with fixation of their barbed end on the surface through the biotin-streptavidin-biotin-gelsolin chain, which also confirmed with the alignment of suspended F-actin along the flow field as shown in Figure 4.27B.

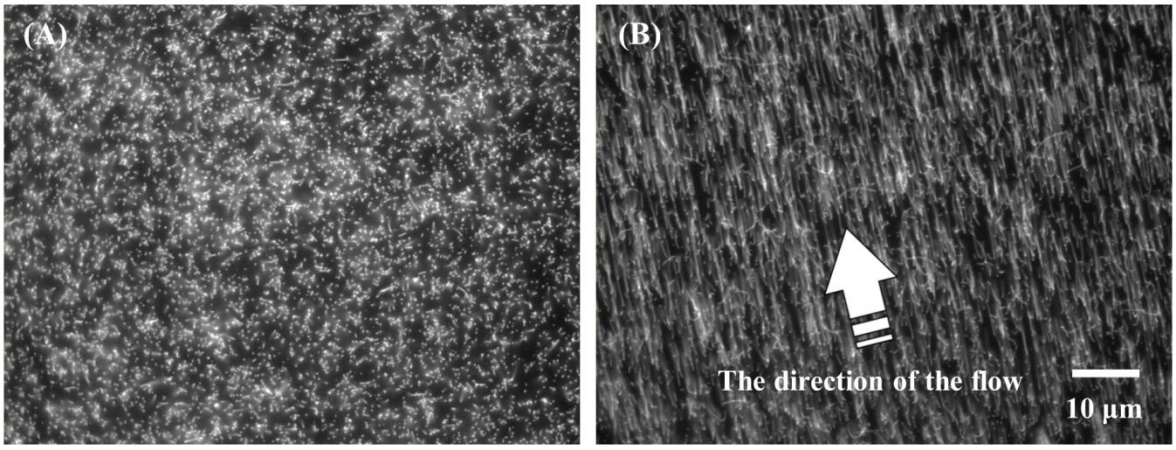

Figure 4.27 Suspended F-actin with fixation of their barbed end on the surface. (A) Most F-actin was suspended near the surface with fixation of their barbed end on the surface through the biotin-streptavidin-biotin-gelsolin chain. 25 μg/mL of bGA complexes were introduced at 0.28 mm/s for 30 m. (B) In the presence of a flow field, suspended F-actin showed their alignment along the flow field. The mean velocity of the flow field was 2 mm/s.

In a high surface population of F-actin, the suspended F-actin near the surface can be confirmed with a laser scanning confocal microscopy (Zeiss LSM 510). To get the high surface population of F-actin, 25 μg/mL of F-actin was introduced every 30 min, which helped with agitating the solution inside the flow cell and maintaining the concentration of F-actin. After three or four times introductions of F-actin solution, the desired population of F-actin was formed on the streptavidin-coated surface.

As shown in Figure 4.28, single ends of F-actin were anchored at the surface, which made the surface look as if it were covered by numerous white dots. This effect showed that no significant non-specific binding of F-actin occurred even with a high surface population of F-actin. On the other hand, a cloud of suspended F-actin was observed in the middle of the solution.

In observation of the high surface population of F-actin with the confocal microscopy, 3D imagery of the suspended F-actin near the surface was obtained. The suspended F-actin could reach up to 8 μm above the surface while most suspended F-actin existed under 6 μm above the surface. The depth of the suspended F-actin can be varied if the molar ratio between F-actin and gelsolin in bGA complexes is changed.

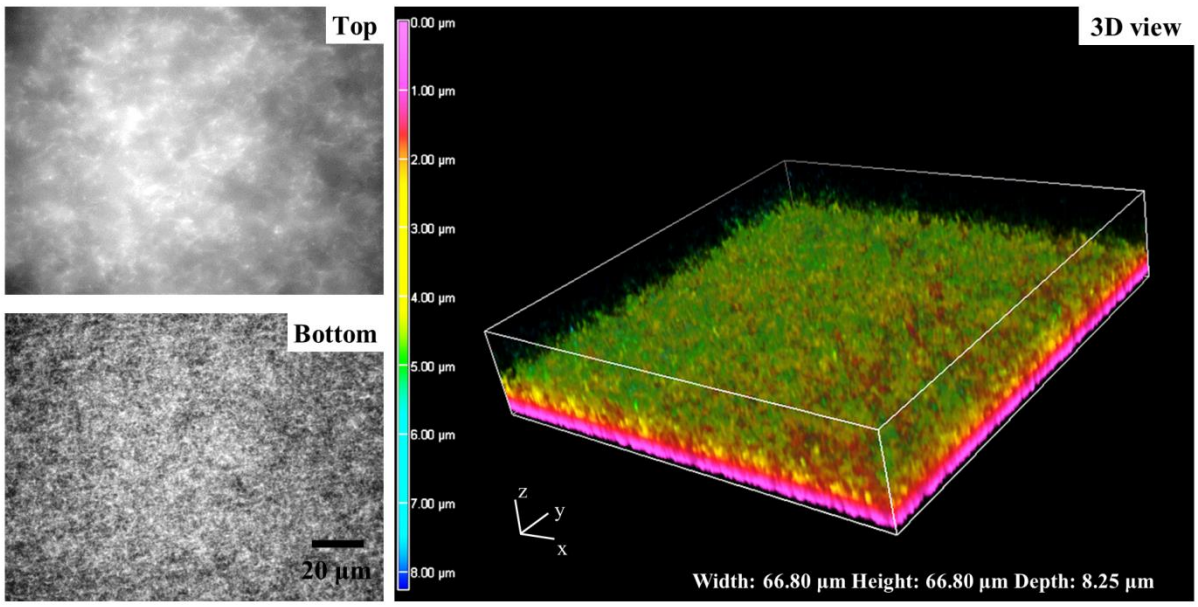

Figure 4.28 A high population of F-actin on a surface. Even with the high surface population of F-actin, no significant non-specific binding of F-actin occurred. The 3D image created by the confocal microscopy demonstrated the volume image of the suspended F-actin with fixation of their barbed end on the surface. To create the 3D image of the suspended F-actin, 1000:1 molar ratio of F-actin and gelsolin was used.

In the presence of a flow field, F-actin was forced to lie down on the surface with the alignment along the flow field as shown in Figure 4.27B. However, the removal of the flow field resulted in F-actin resuspension due to blocking of non-specific binding. To prevent this, aligned F-actin had to be immobilized before it was resuspended. Such immobilized actin arrays should support the motility of HMM-coated beads.

Possibilities for F-actin immobilization were electrostatically, chemically, and biologically investigated. For the electrostatic immobilization of F-actin, PLL, a positively charged amino acid polymer was investigated, since PLL has also been used to form bundles of F-actin which show motility on a chemically crosslinked myosin gel [144]. When a sufficient population of F-actin was formed on the surface, 0.01% of PLL in B-PBS buffer was introduced at 2 mm/s for 1 hour. In the presence of PLL in a flow field, F-actin appeared to form complexes with PLL, binding to the surface through electrostatic

interactions. Suspended bGA complexes were aligned along the direction of the flow field and stayed attached to the surface after the removal of the flow field as shown in Figure 4.29.

When HMM-coated particles were introduced, they were bound to the F-actin arrays. However, HMM-coated particles remained stationary, and no movement of HMM-coated particles was observed. The lack of movement suggests that PLL may inhibit the interaction between F-actin and HMM. For the chemical immobilization of F-actin, several water-soluble homobifunctional crosslinking reagents (GA, BS^3, and DMS) containing amine-reactive groups were investigated since they might have a possibility to crosslink F-actin and form it into a bundle. When a sufficient population of F-actin was formed on the surface, 1% of each homobifunctional crosslinking chemical was introduced at 2 mm/s for 1 hour. Results showed no significant crosslinking on F-actin occurred, so the series of homobifunctional crosslinking chemical could not prevent F-actin resuspension from the surface. It is possibly because of the chemical's preference for bridging two nearby amino groups on the actin molecule rather than crosslinking actin molecules far apart [145].

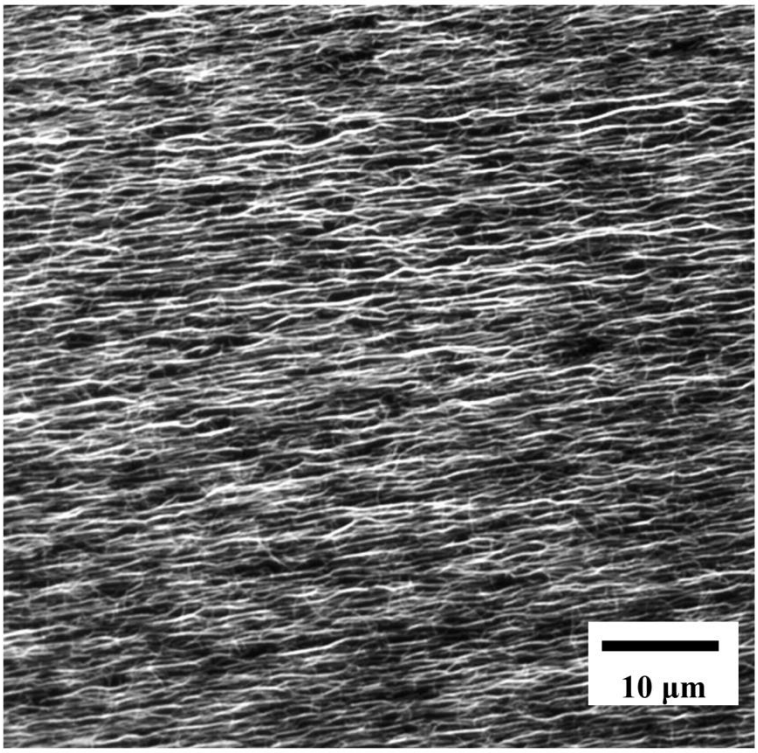

Figure 4.29 Actin arrays formed by PLL. After proper surface population of F-actin was formed on the surface, 0.1% of PLL (M.W. = 70 kDa – 150 kDa) solution was introduced for 1 hour at 2 mm/s. Suspended F-actin was laid down along the flow field and immobilized on the surface. However, no movement of HMM-coated particles was observed.

Actin bundling is observed when its mechanical properties are required to fulfill specific biological functions in cells [15, 146]. For instance, actin bundling is found in filopodia present at the leading edge of motile cells to aid cell adhesion and cell motility [147] and is also involved in the formation of microvilli found in intestinal epithelial cells to enhance nutrient absorption [148].

Fascin is one of the actin-bundling proteins [30, 149, 150]. It is reported that F-actin forms polarized bundles with fascin *in vitro*, showing motility in interactions with myosin [94]. Due to these characteristics, fascin was studied as a biological immobilizer in forming the arrays. In introducing a flow field containing 2 μg/mL of fascin (MBS203522, MyBioSource) for 1 hour at 2 mm/s, aligned F-actin formed bundles with fascin, and as a result, the resuspsension was prevented after the flow field was ceased.

The alignment of the arrays, which was affected from the average length of bGA complexes and the surface population of F-actin, was quantified with the aid of OrientationJ, ImageJ's plugin. The software uses structure tensor analysis to derive local orientations in images and facilitates characterizing orientations of sophisticated structures [151]. As shown in Figure 4.30, when an image of the arrays (Figure 4.30A) is analyzed, the software provides local orientations of the arrays, displayed according to a color scale (Figure 4.30B).

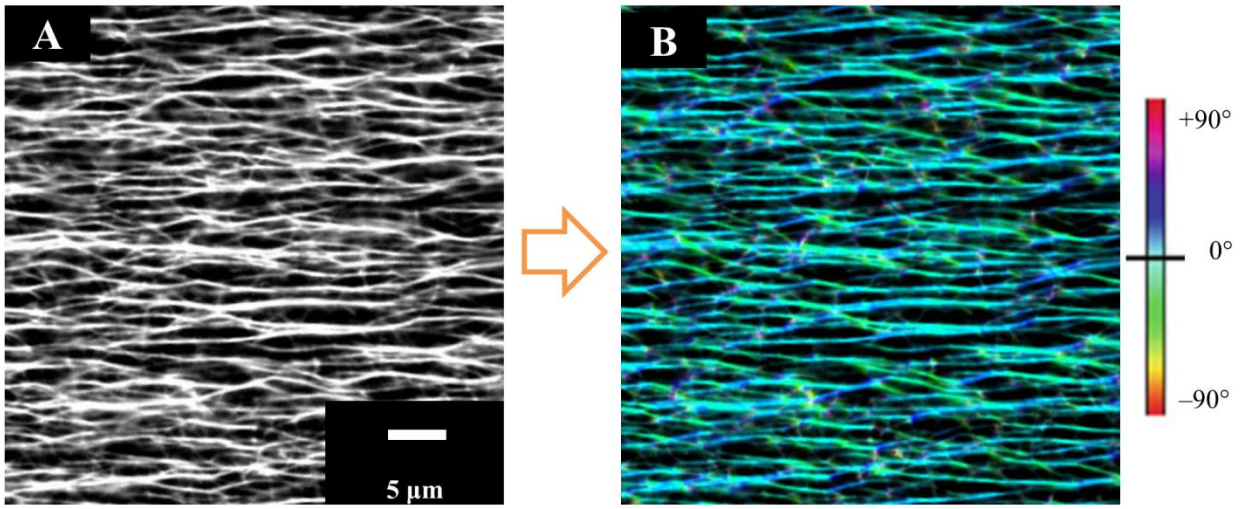

Figure 4.30 The orientation analysis of the fascin-crosslinked actin arrays using OrientationJ. (A) Original image of the arrays. (B) Color-coded map. Local orientations of the arrays are displayed according to the color scale.

In the orientation measurement of the arrays, the sum of local orientations as a function of the angles (θ) in the range from –90 ° to 90 ° was measured, and $\theta = 0°$ corresponded to the direction of the flow. The distribution of local orientations in the arrays was fit to the Gaussian function in Equation 1 (Figure 4.31)

$$f(\theta) = \frac{1}{w\sqrt{2\pi}} \exp\left(-\frac{1}{2}\left(\frac{\theta}{w}\right)^2\right) \quad (1)$$

For most of the arrays used in this study, $w = 7.6° \pm 0.5°$.

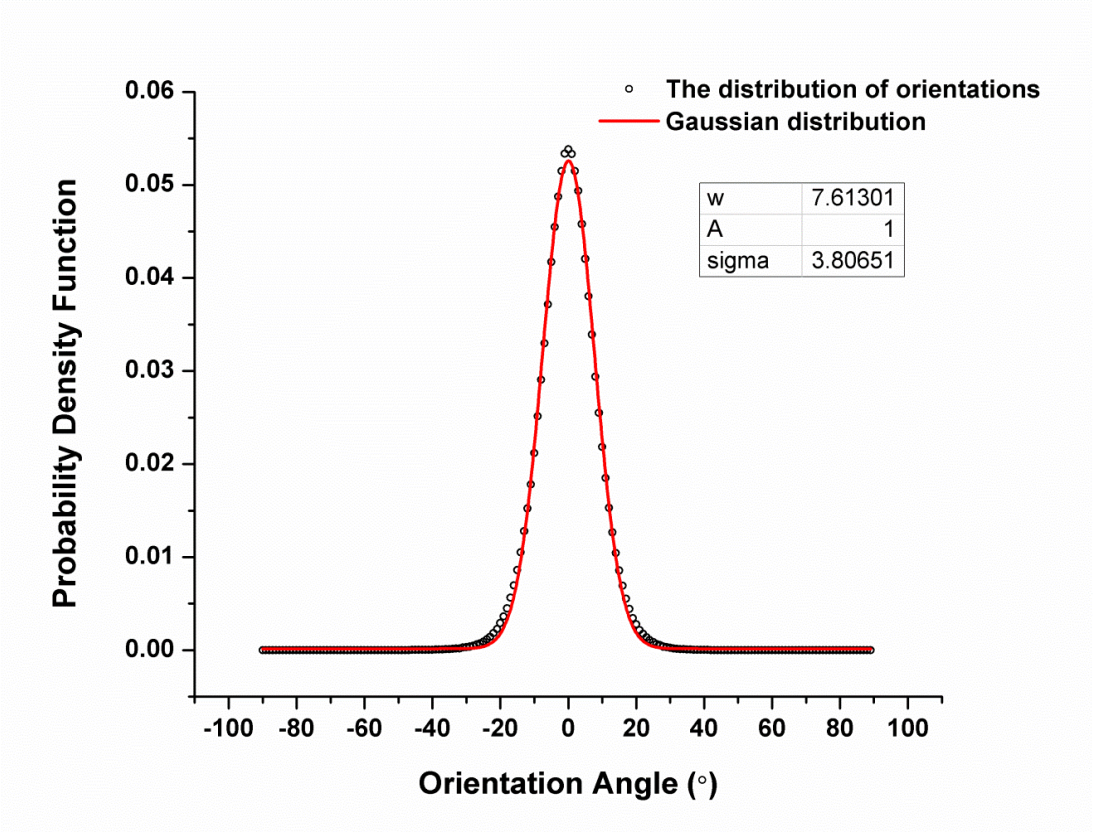

Figure 4.31 Guassian distribution of local orientations in the arrays. The orientation analysis of the fascin-crosslinked actin arrays using OrientationJ provided local orientation information in the range from –90 ° to 90 °. 0 ° corresponded to the direction of the flow. The distribution of local orientations was matched to the Gaussian distribution, and standard deviation of the distribution was acquired. For most of the arrays used in this study, their standard deviation was within 7.6 ° ± 0.5 °.

Experimentally, the high surface population of long F-actin was desirable for good coverage and alignment of the arrays. It was reasonable to assume that the surface population of F-actin was proportional to incubation time.

To investigate proper surface population of F-actin, four different incubation times (30, 60, 90 and 120 min) were tested. 25 μg/mL of bGA complexes in M-buffer was introduced on the streptavidin-coated surface during incubation times. When the incubation time was longer than 30 min, bGA complexes were introduced at 30 min interval to maintain the concentration of bGA complexes. Once the incubation of bGA complexes was complete, unbound bGA complexes were washed away with M-buffer several times. In order to measure the effect of surface population on the alignment of F-actin arrays, 2 μg/mL of fascin was introduced for 1 hour to form F-actin arrays. Once F-actin arrays were formed on the surface, their fluorescent images were analyzed using OrientationJ to measure the alignment. Figure 4.32 shows fluorescent images of F-actin on the surface and F-actin arrays according to incubation times. Each microscopy image comes with its associated look-up tables (LUTs). When adjusting LUTs of the image, the brightness and contrast of the image are changed. When applying the same LUTs to multiple fluorescent images, fluorescence intensities of images can be compared. In Figure 4.32A, optimized LUTs for the fluorescent image of 90 min incubation was applied to other images. The mean gray values of fluorescent images were approx. 8, 37, 122 and 175 for 30, 60, 90 and 120 min incubation, respectively. Images showed fluorescence intensity increased as incubation time increased, which meant the surface population of F-actin increased as incubation time increased. With this method, fluorescence intensities of greater than 120 min incubation were similar to the fluorescence intensity of 120 min. Therefore, it was assumed that the surface population of F-actin was saturated after 120 min incubation. Figure 4.32B shows fluorescent images of F-actin arrays in different incubation times. The images suggest that denser F-actin arrays are formed with longer incubation time. Figure 4.33 shows the orientation measurement for F-actin arrays in different incubation times. The data indicated the alignment of F-actin arrays increased as the surface population of F-actin increased. For 30 min incubation, the standard deviation of orientation distribution was 10.9 ° ± 0.8 °, while the standard deviation for 120 min incubation was reduced as 7.7 ° ± 0.1 °.

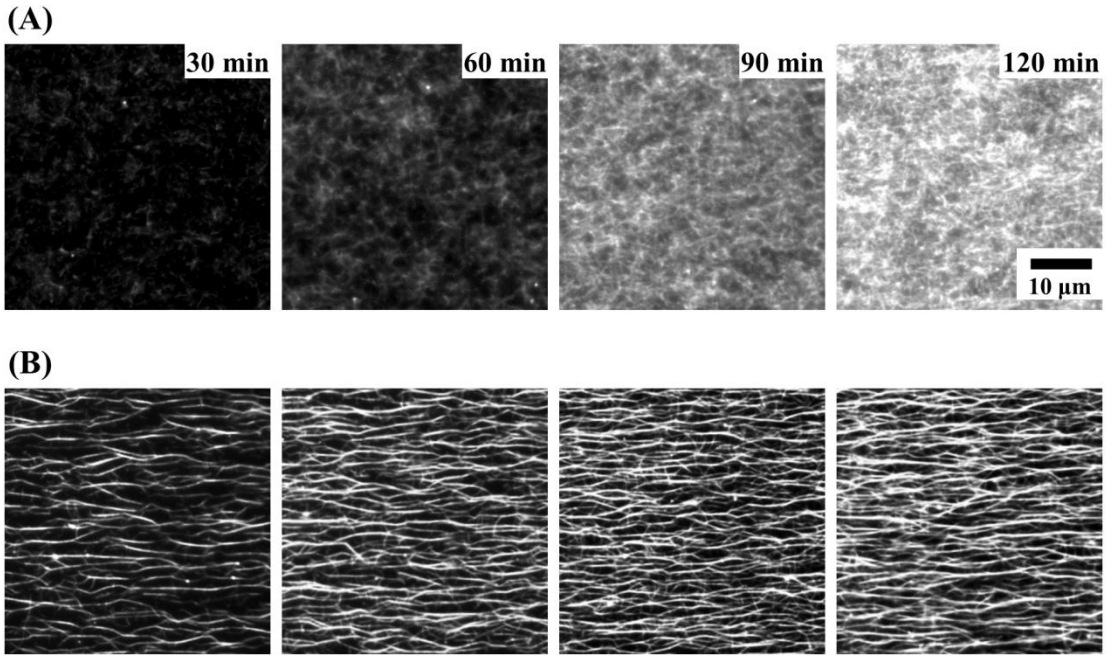

Figure 4.32 Fluorescent images of F-actin on the surface and F-actin arrays according to incubation times. (A) Fluorescent images of surface population of F-actin in different incubation times. (B) Fluorescent images of F-actin arrays in different incubation times.

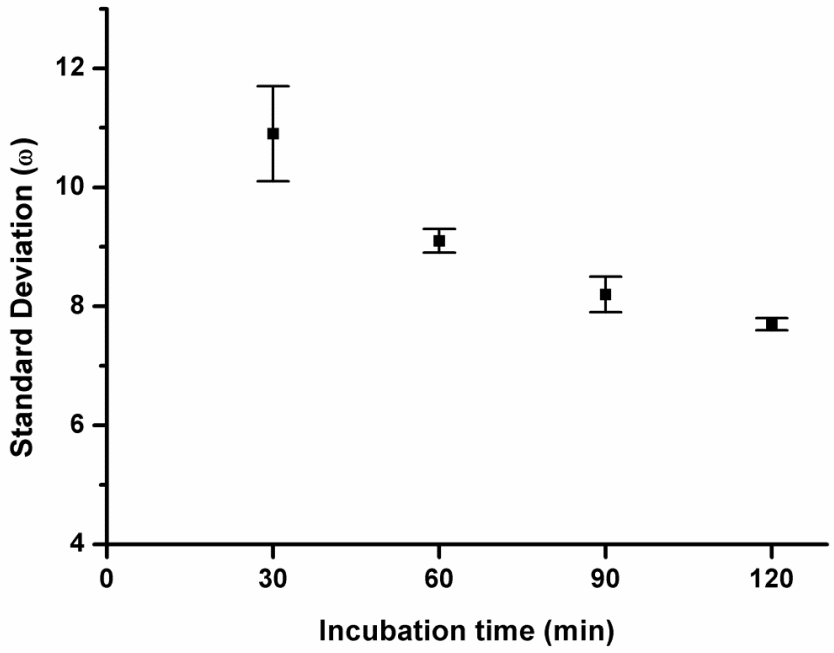

Figure 4.33 The orientation measurement for F-actin arrays in different incubation times. The data indicated the alignment of F-actin arrays increased as the surface population of F-actin increased. The standard deviations of orientation distribution were 10.9 ° ± 0.8 °, 9.1 ° ± 0.2 °, 8.2 ° ± 0.3 ° and 7.7 ° ± 0.1 ° for 30, 60, 90 and 120 min incubation, respectively.

The average length of bGA complexes could be adjusted using the molar ratio between F-actin and gelsolin. Longer F-actin was obtained with higher concentrations of F-actin over gelsolin [152]. To investigate the effect of the average length of bGA complexes on the alignment of F-actin arrays, three different molar ratios of F-actin and gelsolin (500:1, 1000:1 and 1500:1, w/w) were tested. To provide the same surface population of F-actin for each experiment, the concentration of gelsolin was kept the same, and the concentration of F-actin was adjusted when making bGA complexes. For instance, 50 ng/mL of biotinylated gelsolin and 25 μg/mL of F-actin were mixed for 500:1 molar ratio of bGA complexes while 50 ng/mL of biotinylated gelsolin and 75 μg/mL of F-actin were mixed for 1500:1 molar ratio of bGA complexes.

The solution containing bGA complexes in M-buffer was incubated on the streptavidin-coated surface for 120 min with the refreshment of bGA complexes every 30 min. To measure the effect of the length of F-actin on the alignment of F-actin arrays, 2 μg/mL of fascin was introduced for 1 hour. Figure 4.34 shows fluorescent images of F-actin on the surface and F-actin arrays according to molar ratios of bGA complexes. In Figure 4.34A, optimized LUTs for the fluorescent image of 1000:1 molar ratio were applied to other images. The mean gray values of fluorescent images were approx. 81, 108 and 169 for 500:1, 1000:1 and 1500:1 molar ratio, respectively. If it is assumed that the surface populations of F-actin are the same, the difference of the fluorescence intensity may result from the difference of the average length of bGA complexes. Longer bGA complexes have more fluorescence, which causes strong background signals. Figure 4.34B shows fluorescent images of F-actin arrays in different molar ratios of bGA complexes. The orientation measurement for F-actin arrays indicated that the alignment of F-actin arrays increased as the average length of bGA complexes increased. The standard deviations of orientation distribution were 7.8 ° ± 0.3 °, 7.2 ° ± 0.2 ° and 7.0 ° ± 0.1 ° for 500:1, 1000:1 and 1500:1 molar ratio of bGA complexes, respectively. Bead assays were conducted with HMM-coated 1.3 μm and 6.7 μm particles on those F-actin arrays. However, no significant difference was observed in the velocity of HMM-coated particles.

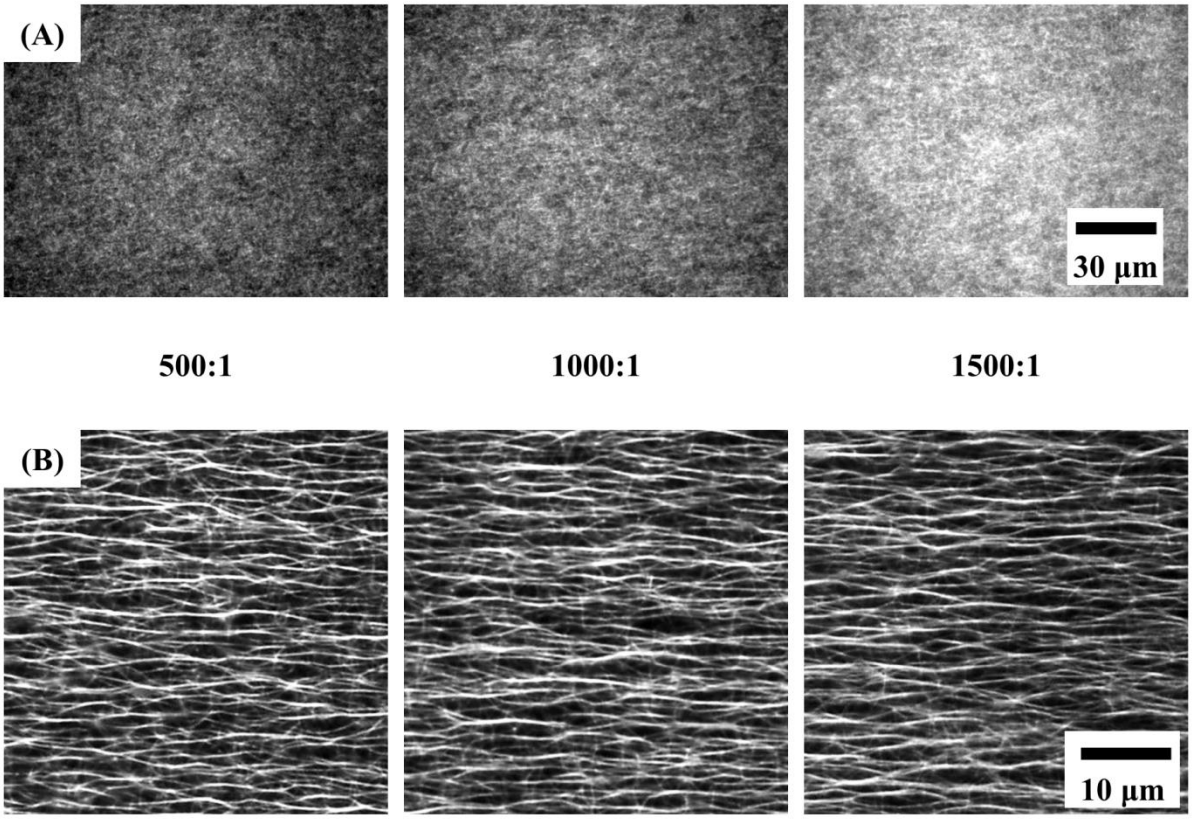

Figure 4.34 Fluorescent images of F-actin on the surface and F-actin arrays according to molar ratio of bGA complexes. (A) Fluorescent images of surface population of F-actin in different molar ratios of bGA complexes. (B) Fluorescent images of F-actin arrays in different molar ratios of bGA complexes. The orientation measurement indicated the alignment of F-actin arrays increased as the average length of bGA complexes increased.

After achieving a suitable surface population of F-actin, the effect of flow fields on the alignment of F-actin was investigated using flow fields with mean velocities of 1, 2, 3, 5, 7, and 10 mm/s. The pressure-driven flow is a parabolic flow, so the velocity of the flow near the surface differs from given mean velocities. The velocity profile of the flow inside the flow cell is given by [153]

$$v(x, y) = v_{\max}\left[1 - \left(\frac{x}{a}\right)^{p}\right]\left[1 - \left(\frac{y}{b}\right)^{q}\right] \tag{2}$$

where $2a = W$ and $2b = H$ are dimensions of the cross section in the rectangular channel. The values of parameters, p and q, can be calculated by

$$p = 1.7 + 0.5\alpha^{-\frac{1}{4}} \tag{3}$$

$$q = \begin{cases} 2 & \text{for } \alpha \le 1/3 \\ 2 + 0.3\left(\alpha - 1/3\right) & \text{for } \alpha > 1/3 \end{cases}$$

where $\alpha = b/a$, the aspect ratio of the channel. When a = 1000 μm and b = 90 μm, α = 0.09, so p = 2.61 and q = 2. The relation of $v_{\max}$ and mean velocity (V) is given by

$$v_{\max} = V\left[\frac{p+1}{p}\right]\left[\frac{q+1}{q}\right] \tag{4}$$

and Equation 2 becomes

$$v(x, y) = v_{\max}\left[1 - \left(\frac{x}{a}\right)^{2.61}\right]\left[1 - \left(\frac{y}{b}\right)^{2}\right] \tag{5}$$

From Equation 5, velocities of flows at the distance of 2 μm above the surface are estimated as approx. 0.09, 0.18, 0.27, 0.46, 0.64, and 0.91 mm/s for mean velocities of 1, 2, 3, 5, 7, and 10 mm/s, respectively as shown in Figure 4.35. Good alignment of F-actin was observed in flow fields ranging from mean velocities of 2 mm/s to 7 mm/s, while disconnection of suspended F-actin from the surface started to occur occasionally at around 10 mm/s. The flow had to be strong enough to align suspended F-actin along the flow direction, but gentle enough to prevent any damage to it. Therefore, in most experiments, a flow field of 2 mm/s was applied unless otherwise specified.

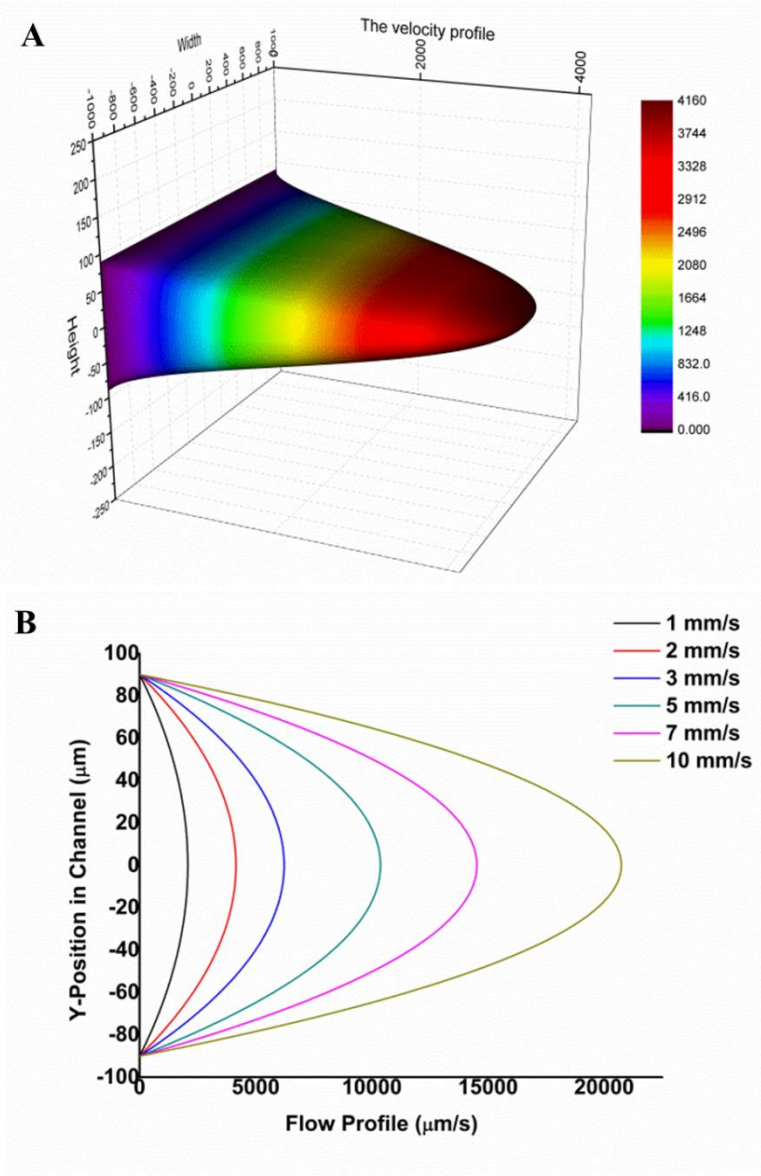

Figure 4.35 Simulation of the flow inside the flow cell. A. The 3D velocity profile of the flow inside the flow cell when the mean velocity is 2 μm/s. B. The velocity profile of flows at Y = 0 for 1, 2, 3, 5, 7, and 10 mm/s. Velocities of flows at the distance of 2 μm above the surface are estimated as approx. 0.09, 0.18, 0.27, 0.46, 0.64, and 0.91 mm/s for mean velocities of 1, 2, 3, 5, 7, and 10 mm/s, respectively.

Fluorescent images of F-actin arrays provided the first way to determine the formation of F-actin arrays and their alignment. In the observation using the fluorescence microscope, it was found that F-actin arrays were formed with 3-dimensional structures. It was demonstrated that it was possible to form a high population of long bGA complexes on the surface, and those F-actin arrays had better alignment. However, increasing numbers of bGA complexes binding to surface caused blocking of the non-specific binding site to be unstable. This led to non-specific bindings of short bGA complexes on the surface. As a result, two layers occurred when F-actin arrays were formed from the high population of bGA complexes as shown in Figure 4.36. The upper layer of F-actin arrays (Figure 4.36A) was aligned well along the flow field, while the lower layer of F-actin arrays (Figure 4.36B) was disordered.

In bead motility assays, HMM-coated particles moved on the upper layer of F-actin arrays and disordered lower layer of F-actin arrays seemed not to affect the movement of HMM-coated particles. These 3D network structures of F-actin arrays were observed with the laser scanning confocal microscope, as shown in Figure 4.37. These volume images were created by NIS-Elements AR (Nikon Instruments) after deconvolution using AutoQuant X3 (Media Cybernetics).

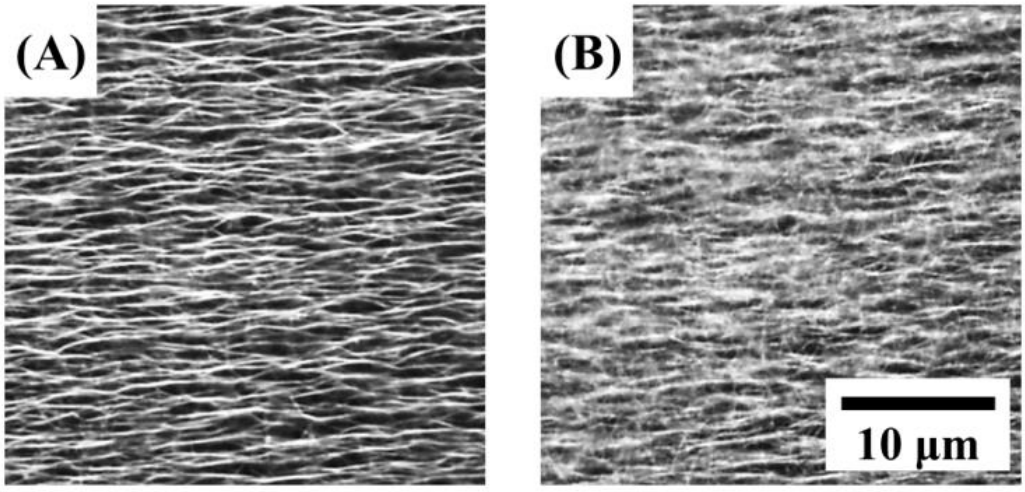

Figure 4.36 Two different layers in F-actin arrays taken from the same location. (A) The upper layer of F-actin arrays. F-actin was aligned along the flow field. (B) The lower layer of F-actin arrays. F-actin was disordered due to non-specific binding of short F-actin.

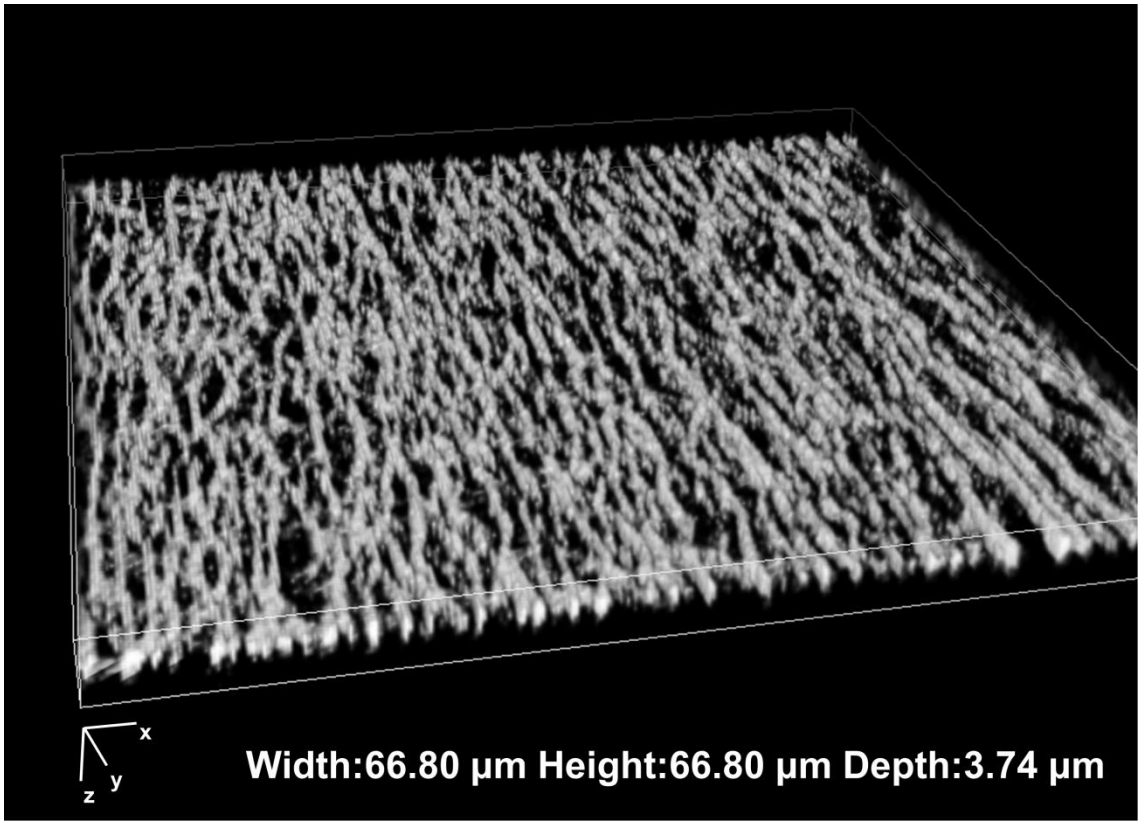

Figure 4.37 A 3D image of F-actin arrays using a confocal microscope.

The polarity of the arrays was identified using a scanning electron microscope (SEM; JSM 7600F, JEOL). When F-actin is decorated with HMM, arrowhead structures are appeared on the filament. This works for the arrays in the same manner [94].

The procedure of sample preparation for SEM imaging can be found in Chapter 3. Briefly, 200 μg/mL of HMM was incubated for 30 min on F-actin arrays in the absence of ATP. 2% of glutaraldehyde, 0.1% of tannic acid and 0.1% of uranyl acetate were introduced as described in the procedure. During dehydration of the sample, the cover slip where F-actin arrays formed was carefully detached from the flow cell. Intensive rinse with anhydrous ethanol was performed to remove any trace of water. After

critical point drying (Autosamdri-815B, Tousimis Research), 2 nm of platinum was deposited on the dried samples using E-beam evaporator (TEMESCAL BJD-2000, Ferrotec). In SEM images of F-actin arrays decorated with HMM, not only the 3D network structures of F-actin arrays were clearly observed, but also the polarity of F-actin in arrays was determined as shown in Figure 4.38 Some disordered actin filaments were found on the lower layer of F-actin arrays, but it was found that most actin filaments on the upper layer of F-actin arrays were arranged with the same polarity.

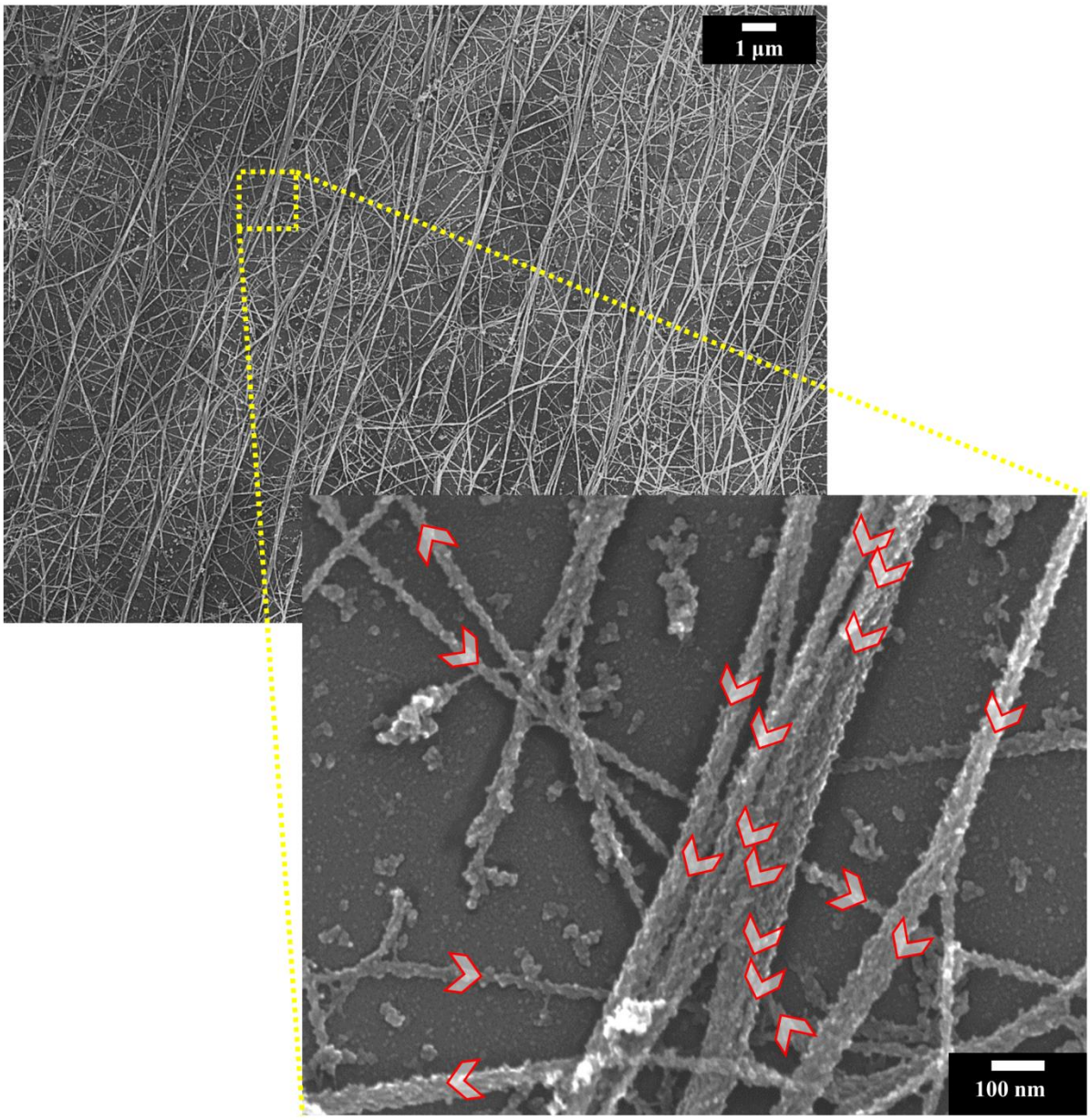

Figure 4.38 SEM images of F-actin arrays. The polarity of F-actin arrays can be confirmed from arrowhead structures in HMM decorated F-actin arrays.

4.4.2 Unidirectional transport of HMM-coated beads

The activity of HMM is greatly influenced by its adsorption behavior on a surface. High quality actin-HMM motility in gliding assays has been performed on hydrophobic surfaces such as nitrocellulose-coated or silanized surfaces as compared with hydrophilic surfaces [61, 154]. During the adsorption of HMM on the surface, hydrophobic interactions occur between the tail domain of HMM and the hydrophobic surface, exposing most HMM heads for interaction with F-actin [2, 155].

In bead assays, the surface of particles, especially nanoparticles, should be hydrophilic in order to facilitate suspension in aqueous solutions. While zero or very slow sliding velocities of motility on negatively charged surfaces has been accounted for by the electrostatic interactions between HMM heads and the surface [61], little investigation of actin-HMM motility on positively charged surfaces has been undertaken. Due to the charge distribution within an HMM molecule [61], it is possible that a negatively charged tail domain may electrostatically bind to positively charged surfaces while the positively charged motor domain of HMM is suspended above the surface to interact with F-actin.

To investigate actin-HMM motility on positively charged hydrophilic surfaces, 0.01 % of PLL was applied to the glass substrates. Velocities of sliding F-actin as a function of KCl concentrations were measured and were compared to those on nitrocellulose-coated surfaces, as shown in Figure 4.39. The movement of sliding F-actin was tracked using Manual Tracking (ImageJ's plugin). The data was analyzed using Matlab. As ionic strengths increased, the velocities of actin-HMM were increased until maximum velocity (≈ 4μm/s) was achieved at 40 mM KCl for nitrocellulose-coated surfaces and at 100 mM KCl for PLL-coated surfaces. The results indicate that actin-HMM motility on PLL-coated surfaces is as effective as on nitrocellulose-coated surfaces.

In addition, the sliding velocity of F-actin on PLL-coated surfaces is maximized at physiological ionic strength. For both surfaces, smooth and continuous sliding movement of F-actin was observed at lower ionic strengths. However, beyond the ionic strength of maximum velocity, F-actin started to dislocate from the surface and ceased its movement at higher ionic strengths. The behaviors of F-actin at higher ionic strengths were similar to those on the surface of lower HMM density [71], which suggests the activity of HMM may be disturbed at higher ionic strengths.

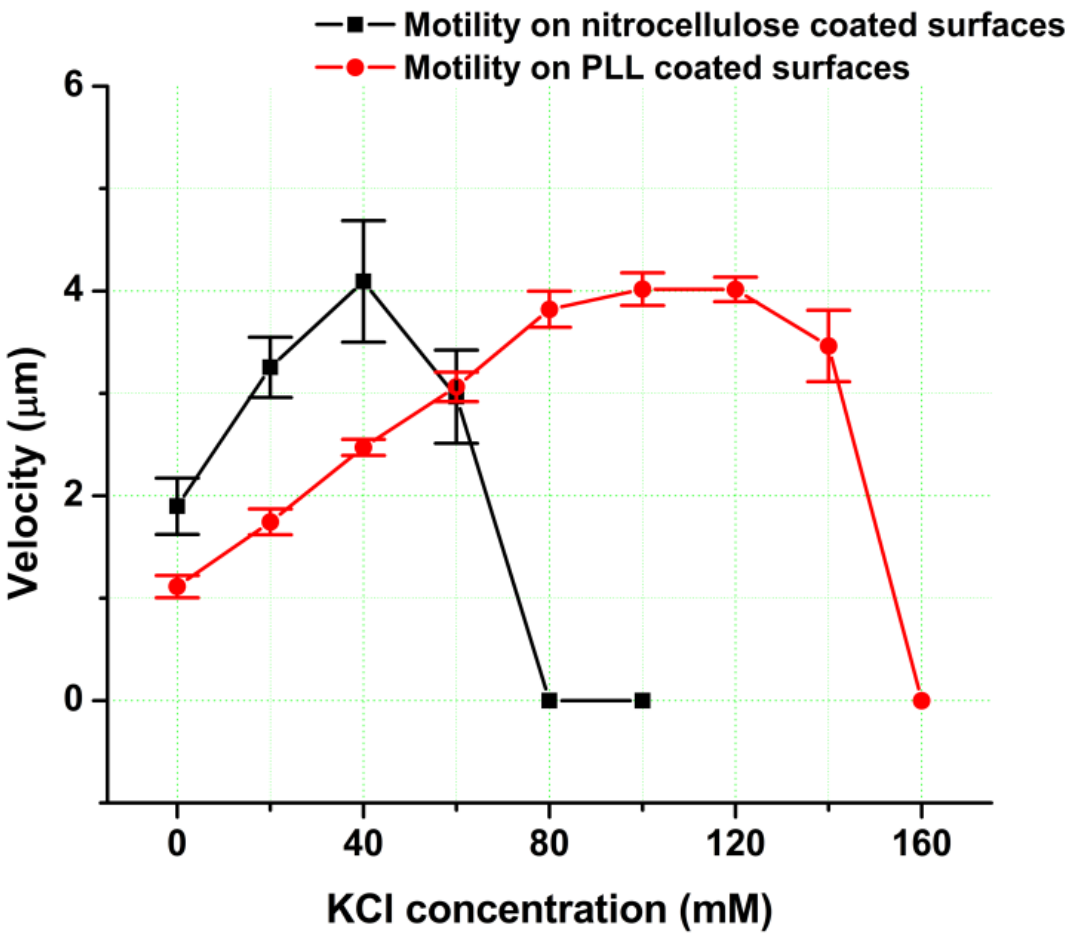

Figure 4.39 Comparison of actin-HMM motilities on nitrocellulose-coated surfaces and PLL-coated surfaces as a function of KCl concentrations. The velocities were proportional to ionic strengths until 40 mM and 100 mM KCl for nitrocellulose-coated surfaces and PLL-coated surfaces, respectively. Maximum velocity for both surfaces was approximately 4 μm/s. Beyond KCl concentrations of maximum velocity, F-actin started to dislocate from the surface and finally stopped its movement at 80 mM and 160 mM KCl, for nitrocellulose-coated surfaces and PLL-coated surfaces, respectively. (n = 30 from three independent experiments)

Given high quality actin-HMM motility on the PLL-coated surfaces, beads were coated with PLL for bead assays. To enhance the adsorption of PLL, carboxyl-functionalized beads (0.5, 1.3, 2.1, 4.5, and 6.7 μm in diameter, Spherotech Inc.) were used. When beads were incubated in 0.01 % PLL solution, all beads were diluted with PLL solution in order to achieve the same surface area (approx. 8.5 cm^2 for 200 μL). After 0.2 mg/mL of HMM was incubated with the PLL-coated beads for 30 min, the bead solution

was introduced into the flow cell where fascin-crosslinked actin arrays were formed. At first, beads were suspended in the medium, but, as soon as they came into contact with the arrays, they started to move along the arrays. All beads moving on the arrays showed unidirectional movement toward the end of the flow cell where the flow solution had been introduced to lay down F-actin, as shown in Figure 4.40A. Figure 4.40B indicates that the directional movement of HMM-coated beads was steady. Moreover, it was observed that the movement of HMM-coated beads was continuous up to several hundred micrometers.

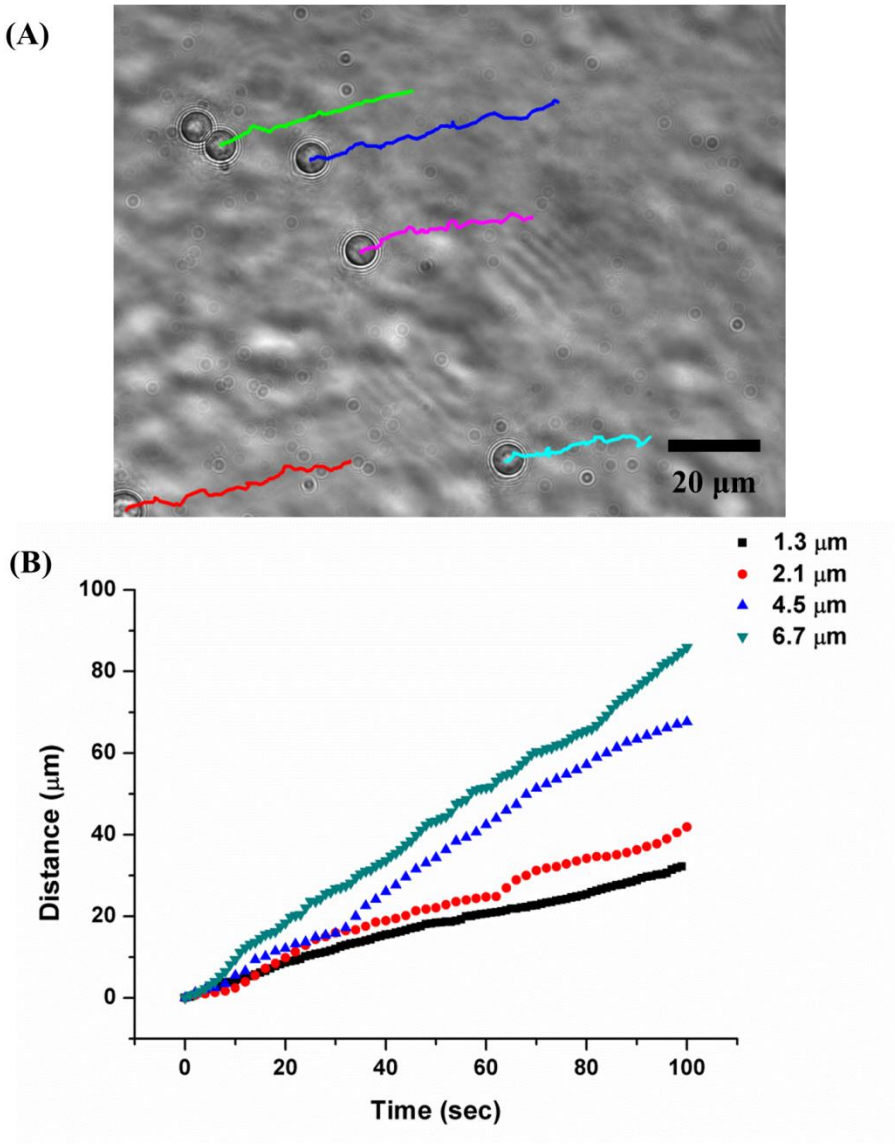

Figure 4.40 The movement of HMM-coated beads on fascin crosslinked F-actin arrays. (A) A tracking image of 6.7 µm beads on F-actin arrays. Tracking data were obtained using Manual Tracking in ImageJ, which also provided displays of tracking results. (B) A graph describing distances of moving beads as a function of time, indicating that the movement of HMM-coated beads was smooth and constant over the distances.

As a non-processive motor protein, the sliding velocity of F-actin is altered by the surface densities of HMM in gliding assays [71], and this feature can be observed in bead assays as well. When it is assumed that HMM is adsorbed uniformly on PLL-coated bead surfaces, the bead size will limit the number of HMM heads that interact with the arrays. Therefore, one may expect that the velocities of beads are likely altered by their sizes. This hypothesis was consistent with our data.

Figure 4.41 is an example showing different velocities affected by the size of beads. The movements of two different sized beads, 1.3 μm and 6.7 μm beads, were tracked in the same period. The 6.7 μm bead started its movement behind the 1.3 μm bead. However, the 6.7 μm bead almost caught up the 1.3 μm bead by the end of the allotted time. The average velocity of the 6.7 μm bead was approx. 0.77 μm/s, while the average velocity of the 1.3 μm bead was approx. 0.4 μm/s.

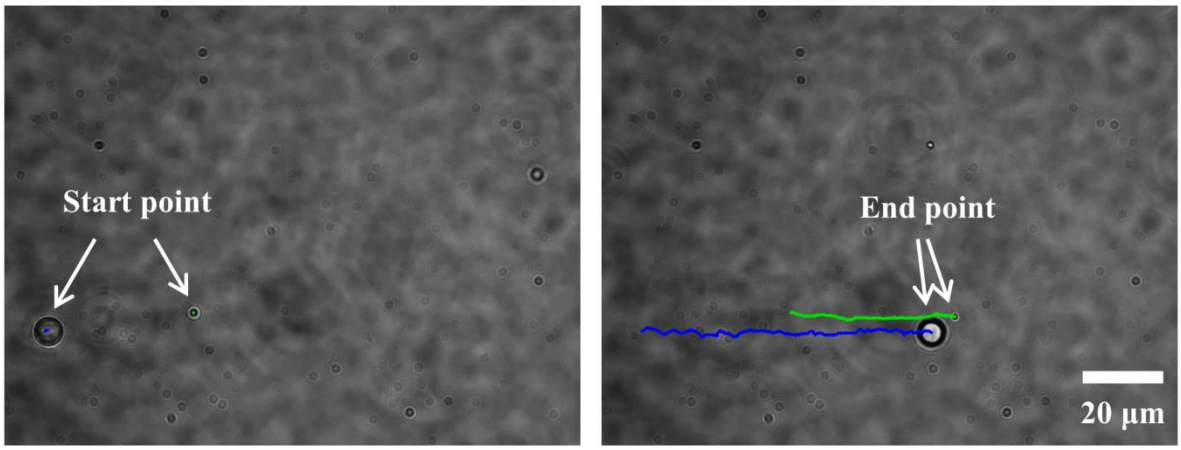

Figure 4.41 Different velocities affected by the size of a bead. The movements of 6.7 μm and 1.3 μm bead were recorded using Manual Tracking plugin in ImageJ software. For the measurement, an image sequence consisting of images with 2 second intervals was used (the video speed is accelerated 30-fold.). The average velocity of 6.7 μm bead was approx. 0.77 μm/s, while the average velocity of 1.3 μm bead was approx. 0.4 μm/s.

Figure 4.42 compares velocities of 0.5, 1.3, 2.1, 4.5, and 6.7 μm beads. No movement of 0.5 μm beads was observed, which might be due to lower number of HMM heads propelling the beads. However, starting with the movement of 1.3 μm beads, velocities of beads increased as their sizes increased, and the maximum velocity of beads was found in the movement of 6.7 μm beads. The velocities of 1.3, 2.1, 4.5, and 6.7 μm beads were 0.33 ± 0.07, 0.35 ± 0.08, 0.60 ± 0.14, and 0.79 ± 0.09 μm/s.

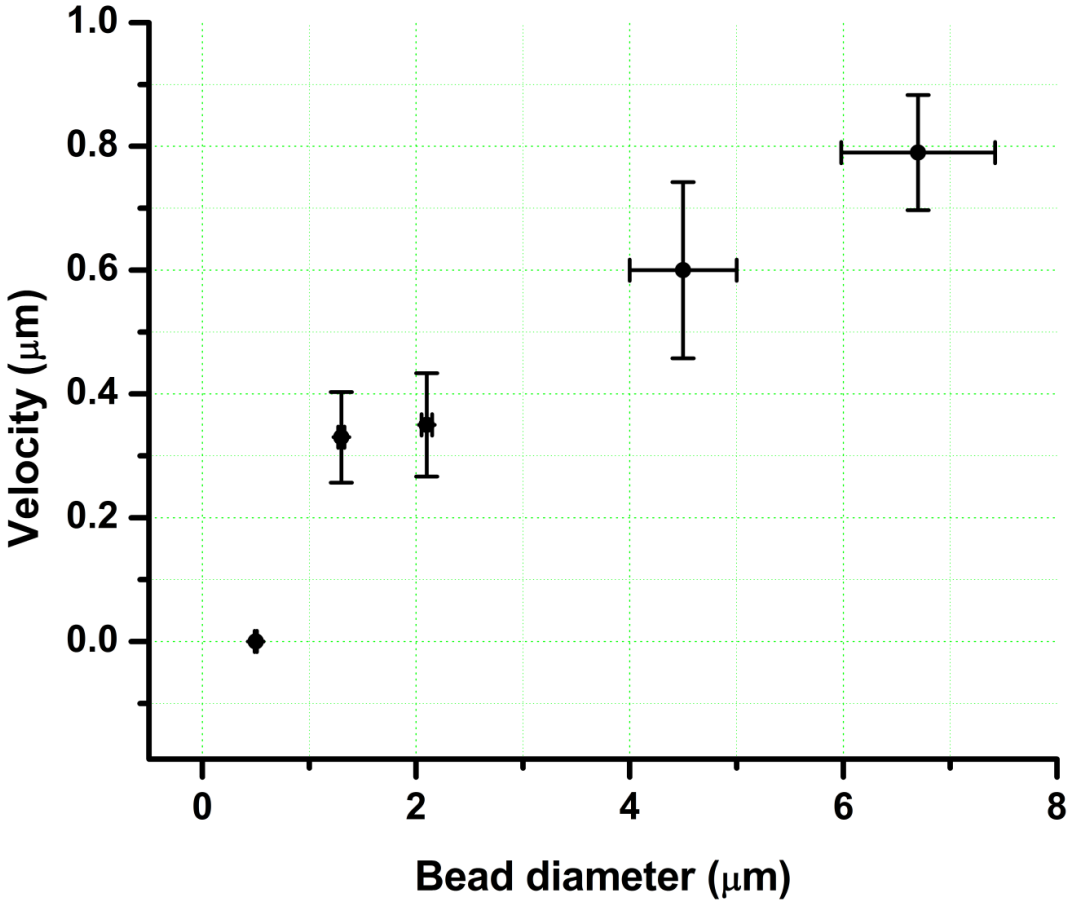

Figure 4.42 Mean velocities of different sized HMM-coated beads on fascin-crosslinked F-actin arrays. No movement of 0.5 μm beads occurred; otherwise, the velocity increased as the size of beads increased. The velocities of 1.3, 2.1, 4.5, and 6.7 μm beads were 0.33 ± 0.07, 0.35 ± 0.08, 0.60 ± 0.14, and 0.79 ± 0.09 μm/s. (n=35 from five independent experiments)

4.4.3 Patterned F-actin arrays

Further applications associated with this approach necessitate developing patterns of fascin-crosslinked actin arrays. In the course of creating these arrays, many materials can be micropatterned. For example, either APTES or biotin may be micropatterned, resulting in patterned actin arrays. While patterning of the arrays can be easily achieved with minor modifications, the material selected had to be carefully considered in order to achieve highly selective attachment of bGA complexes at the desired area.

In a previous study [152], it was found that no significant non-specific binding of F-actin occurred on blocking solution treated, biotin-coated surfaces. This suggests that highly selective attachment of GA complexes is promising at this stage, so streptavidin was chosen to be micropatterned. Various micropatterning techniques exist [156, 157], but microfluidic patterning was employed in order to assure the quality of the streptavidin coating.

A clean PDMS mold engraved with desired microfluidic channels was placed on a biotinylated glass substrate, and 100 μg/mL of streptavidin solution was introduced at the open ends of channels. At the end of the incubation period, the streptavidin solution was washed away with B-PBS buffer, and then the PDMS mold was removed to build a flow cell on the top of the streptavidin-patterned area.

Figure 4.43A shows a fluorescent image of streptavidin patterns on the biotin-coated surfaces after the removal of the PDMS mold. The image indicates that microfluidic patterning provided high selective patterning of streptavidin. bGA complexes were incubated on streptavidin-patterned area in the same manner used to create the original fascin-crosslinked actin arrays.

After unbound bGA complexes were washed away with M-buffer from the flow cell, the observation of the patterned surface confirmed that bGA complexes were patterned along the streptavidin-patterned area as shown in Figure 4.43B. It was also confirmed that no significant non-specific binding of bGA complexes occurred on the non-streptavidin coated area. 2 mm/s of the flow field containing fascin was utilized to form patterned actin arrays. The patterned actin arrays were identical to the original fascin-crosslinked actin arrays as shown in Figure 4.43C.

As expected, the movement of HMM-coated beads on the patterned arrays was also identical to those on the original arrays. No movement of beads occurred on areas where the actin arrays did not exist. 100 μm wide patterned arrays was demonstrated in this study, but the width of the arrays can be technically reduced. The SEM images of the arrays suggest the width of the arrays can be as narrow as 1 μm.

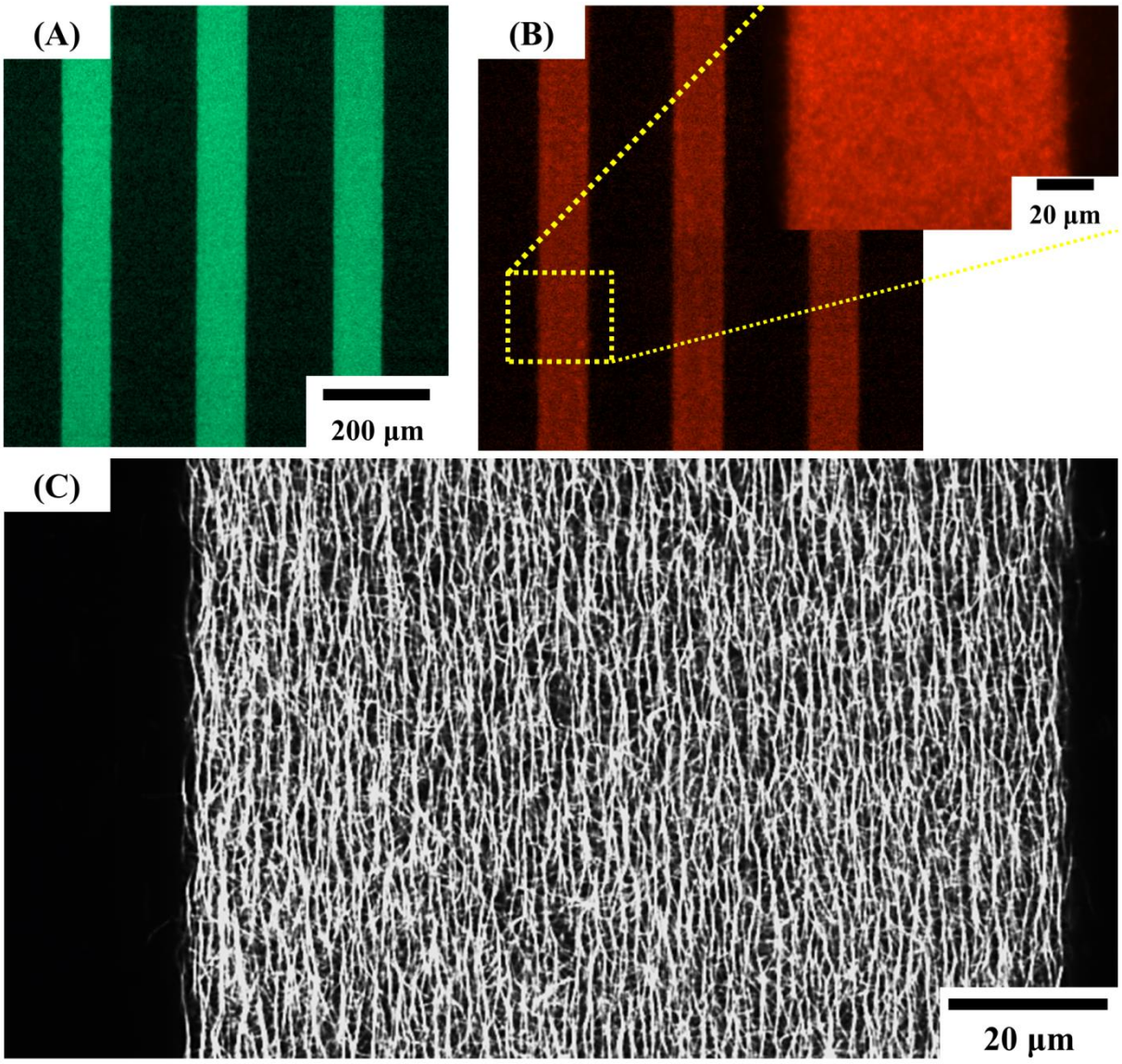

Figure 4.43 Patterned F-actin arrays. (A) Fluorescent image of patterned streptavidin on the biotin-coated surfaces. (B) Fluorescent image of patterned GA complexes. Compared to the streptavidin image, it was found that GA complexes were patterned along the streptavidin patterned area. (C) Fluorescent image of patterned F-actin arrays. The formation of patterned F-actin arrays was identical to the original F-actin arrays.

4.4.4 Conclusion

In the present study, cytoskeletal tracks were created in desired regions, similar to the way they are assembled in cells. Gelsolin was used to control not only the length of F-actin but also its polarity as anchored on the surfaces. After achieving a suitable surface population of F-actin, a flow field and fascin

were utilized to form unipolar F-actin arrays whose polarity was verified using SEM. When HMM-coated beads came into contact with the arrays, they started to move in the same direction over several hundred micrometers. This result suggests that nonprocessive motor proteins such as myosin II are able to perform the linear transport of cargoes in the same way that processive motor proteins do in cells.

This study provides several benefits for future applications. The variation in velocity of nonprocessive motor proteins according particle size can be utilized in sorting applications. For instance, when different sized particles carry different target molecules, starting at the same line, the distances particles move differ according to particle size. Therefore, each target molecule is naturally sorted, similar to the way gel electrophoresis works for the separation of biomolecules.

Although the capability of transport is limited to micro-sized particles in this study, micro-sized particles are more promising for delivery applications than nano-sized particles. Moreover, fascin-crosslinked actin arrays are applicable to the transport of nanoparticles using processive motor proteins such as myosin V. The transport of myosin V bound nanoparticles over a single actin filament has been demonstrated [68, 143, 158]. However, unidirectional transport over long distances has yet to be accomplished because of the lack of such tracks.

Patterned actin arrays will facilitate the development of myosin-based microdevices. For instance, a network of actin arrays using micropatterning will allow multi simultaneous linear transports of motor proteins, which is essential in micro total analysis systems (μTAS). Furthermore, myosin II is one of fastest motor proteins and is employed in skeletal muscles which generate mechanical forces. Therefore, myosin II has great potential to be utilized for applications requiring fast movement or force generation in the manner that nature uses it. This study may serve as a stepping stone for the development of such applications.

A couple of issues were raised in the present study. First, the movement of HMM-coated beads on fascin-crosslinked actin arrays caused the destruction of the arrays as shown in Figure 4.44. While HMM-coated beads moved along the arrays, the arrays were disconnected from the surfaces and released in the medium. Similar to our observations, there is a report demonstrating that the self-organization of actin/fascin bundles is depolymerized in the presence of myosin II at sufficient concentrations [159].

One hypothesis regarding the destruction is based on mechanical stress [160]. Simultaneous interactions of multiple myosin molecules cause compressive stress on single actin filaments. Such compressive stress is enough to lead to buckling and breakage of actin filaments [160]. While the tensile strength of straight actin filaments is up to 600 pN, the breakage of actin filaments occurs with the pull of 2.8 pN in the direction perpendicular to the filament [76]. The 2.8 pN force can be produced even by a

single myosin molecule [62]. Even though the mechanical stress hypothesis rests on single actin filaments, it may provide a clue to prevent the destruction of actin tracks.

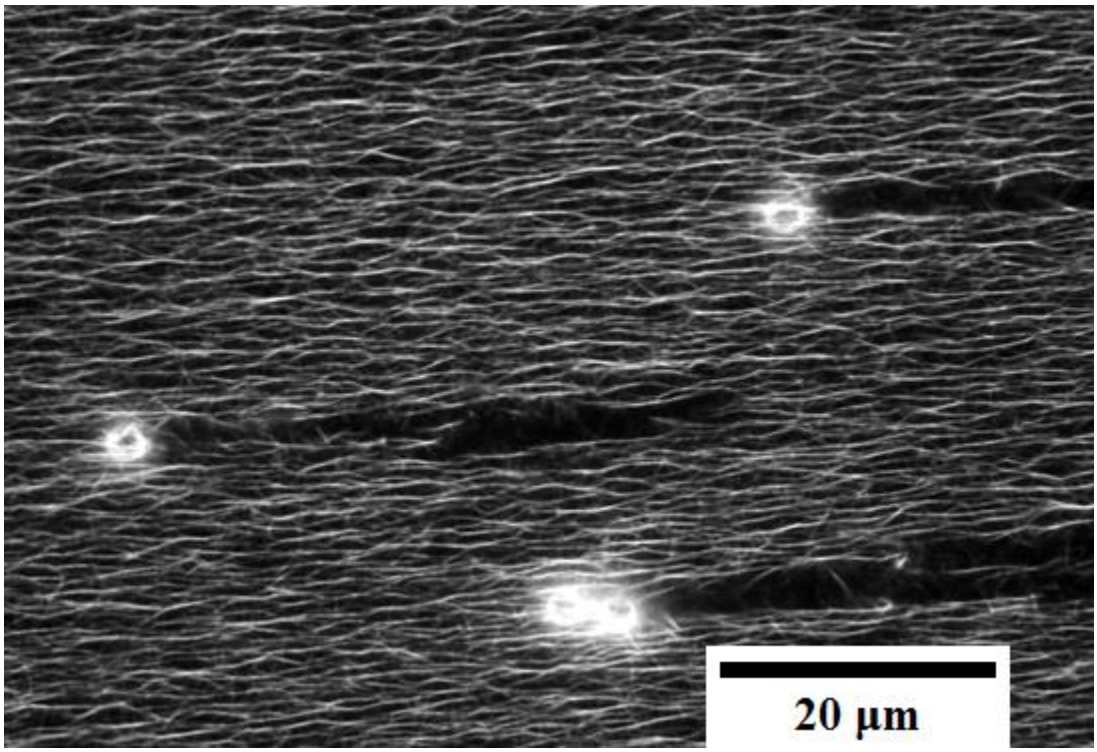

Figure 4.44 An image showing the destruction of the actin arrays as HMM-coated beads pass through the arrays.

To prevent this destruction, chemical modifications were attempted to strengthen the structures of the arrays by crosslinking two amino groups between actin subunits and/or the actin subunit and fascin. 10 mM of dimethyl suberimidate (20700, Thermo Fisher Scientific), 10 mM of bis(sulfosuccinimidyl) suberate (21580, Thermo Fisher Scientific), and 1 % of glutaraldehyde (G7526, Sigma) were incubated with fascin-crosslinked actin arrays.

The movement of HMM-coated 6.7 µm beads was observed. This result indicated that the destruction of the arrays was not prevented by theses chemical modifications, but the modification altered the velocities of HMM-coated beads as approx. 0.3 µm/s, 0.15 µm/s and 0 µm/s, respectively (n=6 from two independent experiments). The velocity changes may be because chemical modifications inhibit the interactions between actin and HMM [145].

Although chemical modifications failed to prevent the destruction of the arrays, apparently stable actin bundles exist in cells and perform cellular functions. For instance, *Nitella* actin cables served as tracks for unidirectional transport of myosin-coated beads [55]. Therefore, the combination of accessory proteins, which stabilize actin filaments and/or actin bundles, will be employed to help prevent the destruction in future studies [24, 161].

Another issue was that HMM-PLL coated beads were slower than gliding F-actin on PLL-coated surfaces. The slow movement of beads may be explained by electrostatic interactions between PLL-coated beads and the actin arrays [143]. In the gliding assay on PLL-coated surfaces, the electrostatic interactions between a single F-actin and PLL-coated surfaces may be negligible due to the size of F-actin. In contrast, in the bead assays, micro-sized and positively charged PLL-coated beads strive through a pool of negatively charged F-actin. As a result, the electrostatic interactions between beads and the arrays may affect the movement of HMM-coated beads.

Eventually, it was observed that some HMM-coated beads showed faster movements, comparable to the movement of F-actin on PLL-coated surfaces (Movie S5 in Supporting Information). The common circumstance involving those beads was that the surface of the beads was covered with some free F-actin. During the destruction of the arrays, although most F-actin was dispersed in the medium, some bound to the surface of beads, confirmed by the beads brightening due to F-actin binding. As F-actin binds to the surface of beads, electrostatic interactions between beads and the arrays may be diminished, resulting in comparable bead movement to that of F-actin on PLL-coated surfaces.

Intriguing questions regarding the function of myosin II were provoked by this study. It is known that the tail domain may regulate the activity of myosin [53]. However, the precise mechanism is still under investigation. Our findings also suggest that the tail domain affects the activity of myosin. Hydrophobic interactions between the tail domain and nitrocellulose-coated surfaces may cause the denaturation of the tail domain, which may result in maximum activity of myosin in ionic strengths lower than physiological ionic strengths. In contrast, hydrophilic interactions are generally reversible. This may not cause any change in the tail domain, which may result in maximum activity of myosin in the range of physiological ionic strengths. However, the precise role of ionic strengths in the regulation of myosin activity by the tail domain is unknown. This study cannot explain why no velocity change occurs in high KCl concentrations in bead assays. Hence, further studies are necessary to investigate the effects of loads on actin-HMM interactions with varying physiological ionic strengths.

CHAPTER 5 – Future directions

In this study, the unidirectional transport of heavy meromyosin (HMM)-coated beads is demonstrated on fascin-crosslinked actin arrays. The streptavidin-coated surface was properly blocked to prevent non-specific binding of F-actin. As a result, a high population of long gelsolin-actin complexes was suspended in the medium for subsequent processes. A flow field was utilized to lay down F-actin aligned along the direction of the flow and fascin crosslinked laid F-actin to prevent F-actin resuspension.

When HMM-coated beads came into contact with the fascin-crosslinked actin arrays, they started to move in the same direction over long distances. Due to the nonprocessive nature of myosin II motor protein, the bead size limited the number of HMM heads on the area in contact with F-actin arrays, which resulted in beads traveling at different velocities according to their sizes. Furthermore, this study demonstrates the patterning of actin arrays, which could serve as a basis for the development of future applications.

During this study, knowledge in the fields including microfabrication, biochemistry, surface chemistry, micropatterning techniques, and nanotechnology has been acquired. In addition, we have gained more understanding and ability to develop transportation and actuation systems at nano-scale. Based on these experiences and skills, we may continue to pursuit the development of transportation systems using motor proteins. Hence, we propose a new methodology to direct the self-assembly of polarized actin tracks, which are essential to cellular transport and nano-scale actuation in hybrid bionano-devices. The self-assembly of actin on the device surface is accomplished by harnessing biological interactions of actin associated proteins, selective molecular micropatterning, and spatial and temporal control. This provides nanoscale and microscale order that mimics actin assemblies found in natural systems. Myosin-based motor transport occurs on these ordered actin tracks. Immediate applications for this technology include sorting, biosensing, and concentrating biomolecules.

The goal of a new methodology is achieved through two specific aims. The first aim centers on precise fabrication of actin tracks using fasctin micropatterning. To further support this aim, the actin filaments are stabilized with actin binding proteins. The second aim involves activities which result in flexible strategies to induce self-assembly of polarized actin tracks using spatial and temporal control of molecules. This self-assembly is directed with caged-ATP. Control of medium viscosity and hydrodynamic flow further confine the delivery of the caged-ATP. These combined aims produce highly ordered cytoskeletal structures with applications in force generation and actuation for hybrid devices.

Development of fascin patterning on the substrate: The development of an artificial actin cortex assembly along 2D arrays of slender silicon pillars has been reported [162]. In this proposed future work, fascin plays and serves as a localizing factor of self-assembled actin tracks. When fascin proteins are patterned on surfaces, they may act like actin-membrane attachment proteins, which tack actin structures to the overlying membrane. Local anchoring of actin will result in the self-assembly of actin tracks along fascin-coated patterns. In addition, the self-assembly of the actin tracks is expected to be polarized due to the characteristics of fascin.

The geometrical boundary conditions of actin growth and orientation can be manipulated by means of the selective molecular micropatterning. To prevent isotropic growth of actin tracks, the width of fascin-coated patterns will be limited. Fascin will be biointylated and streptavidin-coated patterns will be created using micropatterning techniques to fabricate fascin-coated patterns.

Any change of fascin activity is determined following biotinylation. Fascin bundles actin to saturation at a stoichiometry of 1:3 (fascin:actin) [94]. Actin bundling assays with biotinylated fascin and untreated fascin will be conducted and compared.

Immobilized fascin may have limited accessibility to actin molecules. This could potentially affect actin bundling. Therefore, NHS-PEG_X-biotin products are used with spacer arms composed of different lengths of PEG molecules. For biotinylated fascin long spacer arms that are highly flexible are most likely to produce accessible fascin. Actin polymerization assays will be conducted on fascin-coated surface with various spacer arms to observe actin bundle formation. This experiment will also reveal optimal widths of fascin-coated patterns that prevent isotropic growth of actin tracks, while maintaining bundling affinity.

Spatial and temporal control of actin self-assembly: Once fascin molecules are micro-patterned on the surface, it is critical to control the growth direction of self-assembled actin tracks. In filopodia, a variety of proteins are localized in the tip, including formin, VASP, profilin, and N-WASP. This protein complex supports the growth of actin bundles [163]. In the proposed future work, the role of the tip complex of filopodia is mimicked by controlling the distribution and concentration of actin and ATP molecules. This will guide the direction of the growth of self-assembled actin tracks.

The concentration of actin monomers must be above a critical concentration to initiate actin polymerization. In contrast, actin will depolymerize when the concentration is below this critical value. The critical concentration varies in the presence of actin-associated proteins or chemicals. For instance, ATP bound G-actin is easier to polymerize than ADP bound G-actin. In addition, the different ends of actin filaments require different critical concentrations since both ends have different kinetic rate

constants for association and dissociation. One study reported that in the presence of ATP, the critical concentration at the plus end is 0.1 μM, while the critical concentration at the minus end is 0.8 μM [164]. In addition, it is known that the critical concentration of ADP-actin at the barbed end is 1.8 μM [165].

In proposed future work, actin monomers and caged-ATP are continuously supplied by means of precise flow and diffusion controls. A solution of 0.8–1 μM actin with caged-ATP will not be polymerized until a UV light opens the caged structure, releasing the ATP. As UV light activates caged-ATP over fascin-coated patterns, the critical concentration of actin becomes low, and actin polymerization is initiated. Immobilized fascin proteins mimic actin-membrane attachment proteins. As a result, the direction of growth of the plus end is towards the fascin-rich area.

The polarity of self-assembled actin tracks will be identified using a scanning electron microscope (SEM; JSM 7600F, JEOL). When F-actin is decorated with HMM, arrowhead structures are appeared on the filament. The procedure of sample preparation for SEM imaging followed published procedure with 0.1 M sodium phosphate, buffered at pH 7.0. After critical point drying (Autosamdri-815B, Tousimis Research), 2 nm of platinum is deposited on the samples using an E-beam evaporator (TEMESCAL BJD-2000, Ferrotec) [93].

Prevention of the destruction of the self-assembled actin tracks: It is expected that self-assembled actin tracks will be obliterated when they interact with myosin II molecules. In the previously proposed work, the movement of HMM-coated particles on fascin-cross-linked actin arrays caused the obliteration of the arrays. While HMM-coated particles moved along the arrays, the arrays disconnected from the surfaces and released into the medium.

However, it is apparent that stable actin cytoskeletal structures exist in cells and perform cellular functions. These actin structures often interact with actin-associated proteins to mechanically strengthen the overall structures. In skeletal muscle, actin filaments interact with thick filaments formed by myosin II for muscle contraction. Thin filaments consist of actin filaments, tropomyosins, and troponins. Tropomyosin is wrapped around actin filaments to stabilize them. It is also reported that tropomyosin stabilizes actin bundles as well as filaments [166, 167]. In addition, several actin-cross-linking proteins are often found in the same actin bundles and work together to strengthen their structures. It is reported that the combination of α-actinin and fascin produces mechanically robust actin networks [168]. By means of such actin-associated proteins, therefore, it may be possible to self-assembled actin tracks resistant to the compressive stress generated by interactions with myosin molecules.

In the proposed future work, the effect of tropomyosin and several actin-cross-linking proteins including filamin and α-actinin will be investigated. The success of the formation of non-destructive actin tracks will be determined by interactions with HMM-coated particles. Proteins to be investigated, including tropomyosin, filamin, and α-actinin and their fluorescently labeled antibodies, are commercially available at Sigma-Aldrich or MyBioSource. This study will provide stable actin tracks to facilitate the development of a biological motor system used to advance our understanding of the actin-myosin motors.

Demonstration of highly ordered self-assembled actin tracks: The approach utilized to fabricate linear tracks of polarized self-assembled actin is expanded to create branched, or Y-shaped, actin tracks as shown in Figure 5.1A. This branching is a basic component of *in vivo* actin structures. Arranging a finite number of Y-shaped actin tracks, is a straightforward strategy to create diverse actin structures (Figure 5.1B and C) applicable for sorting, biosensing, and concentrating.

The main challenge to creating multiple Y-shaped, self-assembled actin tracks is to prevent isotropic growth at the branch sites. Since the process flow direction is parallel to the portion of the channel that leads to the branch (i.e. the straight side of "Y"), the width of branches will be broadened. This is a consequence of the fact that the process flow is parallel with the base of the branch structure. For example, if the branch angle is 40°, then the effective branch width exposed to the process flow will be 30.5% wider than the straight side. To prevent isotropic growth, various branch angles will be explored and the width of fascin-coated patterns on branch sites will be adjusted as necessary. With successful growth of Y-shaped actin tracks, more elegant actin structures will then be fabricated. These structures are included, but not limited to, vascular-like, aster-like, or honeycomb-like structures.

Each of these actin structures serves a unique application. Vascular-like structures can be utilized for particle sorting applications. When myosin-coated particles enter the minus end, they move along actin tracks and are collected on branches at the plus end. The distribution of myosin-coated particles that are directed to each branch is related to the symmetry of the branched structure. Aster-like structures are also utilized for biosensing and concentrating. For these structures (shown in Figure 5.1C), the plus ends are located at peripheral regions and the minus is at center. Plus end-directed motor proteins like myosin II and myosin V move toward the periphery regions while myosin VI, a minus end-directed motor protein [169], moves toward the center. These myosin-coated particles will carry antibodies that accumulate antigens and concentrate these antigens at the aster center for biosensing applications. Moreover, honeycomb-like actin tracks will carry out similar functions, except that the direction of movement for concentration is focused at the both ends of the structure.

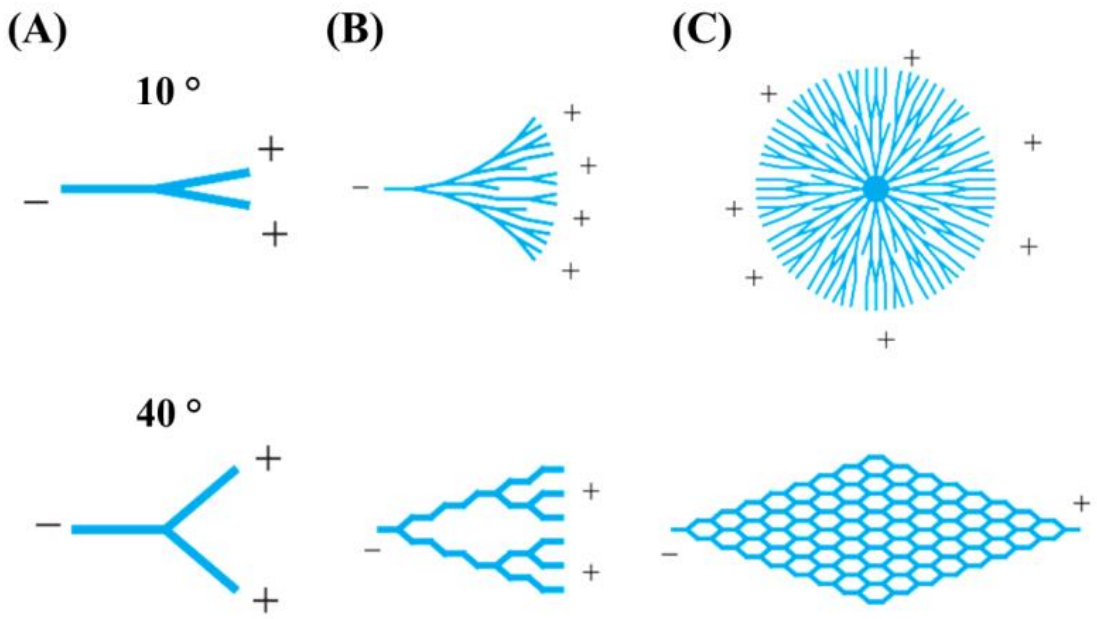

Figure 5.1 Y-shaped and highly ordered actin tracks.

In addition to lab-on-a-chip applications, this proposed research is applicable to *in vitro* studies of actin-based cytoskeletal structures that exist in living cells. Since assembly of highly ordered actin tracks has the potential to create sophisticated actin structures similar to those in cells, the proposed hybrid-bionano devices serve as an innovative tool to design and implement *in vitro* assays that model *in vivo* functions performed by these cytoskeletal complexes.

APPENDIX: MATLAB CODES

Velocity Calculation

```
%Import tracking data generated by the manual tracking
clear

[a b]=size(results); %Extract x and y values

sep=[];

ave_vel=[]; %average velocities for each tracking

ave_std=[]; %STDs for each tracking

for i=1:a

    if results(i,7)==-1
        sep=[sep i];
    end

end

[c d]=size(sep);

for j=1:d

    if j ~= d

        Factin{j}=results(sep(j):sep(j+1)-1,7);

    else

        Factin{j}=results(sep(j):a,7);

    end

end

for j=1:d

    [171]=size(Factin{j});
    Factin{j}(1,2)=mean(Factin{j}(2:e,1));
    Factin{j}(2,2)=std(Factin{j}(2:e,1));
    ave_vel=[ave_vel Factin{j}(1,2)];
    ave_std=[ave_std Factin{j}(2,2)];
    Factin{j}(1,3)=0;
```

```
    for x=2:e
        Factin{j}(x,3)=Factin{j}(x-1,3)+Factin{j}(x,1);
    end
end
mean(ave_vel) %total average velocity
std(ave_vel) %STD for average velocities
```

Length Calculation

```
%Import tracking data generated by the manual tracking
clear
[a b]=size(results);
step=[];
Length_F=0;
for i=1:a
    if results(i,6)==-1
        step=[step i];
    end
end
[c d]=size(step);
for j=1:d
    if j ~= d
        Length_F(j)=sum(results(step(j)+1:step(j+1)-1,6));
    else
        Length_F(j)=sum(results(step(j)+1:a,6));
```

```
    end
end
Length_F %length of F-actin for each tracking
```

Coverage Calculation

```
% image will be imported manually
bwim=im2bw(mei); %convert black and white image
figure
imshow(bwim)
z=0;
for i=1:1024
    for j=1:1344
        if bwim(i,j)==0
            z=z+1;
        end
    end
end
covered = z/(1024*1344)*100
```

2D parabolic flow

```
%2D profiles of parabolic flows
clear
y=-90:0.1:90;
m_vel=[1000 2000 3000 5000 7000 10000];
d=180;
for i=1:6
    u{i}=3/2*m_vel(i).*(1-(y./(d/2)).^2);
    plot(u{i},y), hold on
end
x=0:10:15000;
sl=-87*ones(1,1501);
figure
plot(x,sl)
```

3D parabolic flow

```
%3D profile of a parabolic flow
clear
a=1000;
b=90;
s=2.61;
r=2;
x=-1000:1:1000;
```

```
y=-90:1:90;
u_max=(((s+1)/s)*((r+1)/r))*[1000 2000 3000 5000 7000 10000];
[x1,y1]=meshgrid(x,y);
for i=1:6
    z{i}=u_max(i).*(1-(abs(x1)./a).^s).*(1-(abs(y1)./b).^r);
end
figure
surf(x1,y1,z{6},'EdgeColor','none')
```

BIBLIOGRAPHY

[1] M. G. L. v. d. Heuvel and C. Dekker, "Motor proteins at work for nanotechnology," *Science,* vol. 317, pp. 333-336, 2007.

[2] B. Alberts, A. Johnson, J. Lewis, M. Raff, K. Roberts, and P. Walter, *Molecular biology of the cell*, 4 edition ed.: Garland Science, 2002.

[3] D. Riveline, A. Ott, F. Jülicher, D. A. Winkelmann, O. Cardoso, J.-J. Lacapère, S. Magnúsdóttir, J.-L. Viovy, L. Gorre-Talini, and J. Prost, "Acting on Actin: The Electric Motility Assay," *European Biophysics Journal,* vol. 27, pp. 403-408, 1998.

[4] S. B. Asokan, L. Jawerth, R. L. Carroll, R. E. Cheney, S. Washburn, and R. Superfine, "Two-dimensional manipulation and orientation of actin-myosin systems with dielectrophoresis," *Nano Letters,* vol. 3, pp. 431-437, 2003.

[5] R. Stracke, K. J. Böhm, J. Burgold, H.-J. Schacht, and E. Unger, "Physical and technical parameters determining the functioning of a kinesin-based cell-free motor system," *Nanotechnology,* vol. 11, pp. 52-56, 2000.

[6] Y. Hiratsuka, T. Tada, K. Oiwa, T. Kanayama, and T. Q. P. Uyeda, "Controlling the direction of kinesin-driven microtubule movements along microlithographic tracks," *Biophysical Journal,* vol. 81, pp. 1555-1561, 2001.

[7] J. A. Spudich, S. J. Kron, and M. P. Sheetz, "Movement of myosin-coated beads on oriented filaments reconstituted from purified actin," *Nature,* vol. 315, pp. 584-586, 1985.

[8] F. B. Straub, *in STUDIES From the Institute of Medical Chemistry University Szeged* vol. 2, 1942.

[9] E. D. Korn, "Actin Polymerization and its Regulation by Proteins from Non-muscle Cells," *Physiological Reviews,* vol. 62, pp. 672-737, 1982.

[10] E. Korn, M. Carlier, and D. Pantaloni, "Actin Polymerization and ATP Hydrolysis," *Science,* vol. 238, pp. 638-644, October 30, 1987 1987.

[11] W. Kabsch and J. Vandekerckhove, "Structure and Function of Actin," *Annual Review of Biophysics and Biomolecular Structure,* vol. 21, pp. 49-76, 1992.

[12] L. R. Otterbein, P. Graceffa, and R. Dominguez, "The crystal structure of uncomplexed actin in the ADP state," *Science,* vol. 293, pp. 708-711, Jul 2001.

[13] M.-F. Carlier and D. Pantaloni, "Control of Actin Dynamics in Cell Motility," *Journal of Molecular Biology,* vol. 269, pp. 459-467, 1997.

[14] K. C. Holmes, D. Popp, W. Gebhard, and W. Kabsch, "Atomic Model of The Actin Filament," *Nature,* vol. 347, pp. 44-49, Sep 1990.

[15] T. D. Pollard and J. A. Cooper, "Actin and Actin-binding Proteins - A Critical Evaluation of Mechanisms and Functions," *Annual Review of Biochemistry,* vol. 55, pp. 987-1035, 1986.

[16] A. Uzman, "Molecular Cell Biology (4th edition) - Harvey Lodish, Arnold Berk, S. Lawrence Zipursky, Paul Matsudaira, David Baltimore and James Darnell; Freeman & Co., New York, NY, 2000, 1084 pp., list price $102.25, ISBN 0-7167-3136-3," *Biochemistry and Molecular Biology Education,* pp. 126-128, 2001.

[17] L. L. Frado and R. Craig, "Electron-microscopy of the Actin-myosin Head Complex in the Presence of ATP," *Journal of Molecular Biology,* vol. 223, pp. 391-397, Jan 1992.

[18] J. F. Casella, M. D. Flanagan, and S. Lin, "Cytochalasin-D Inhibits Actin Polymerization and Induces Depolymerization of Actin-filaments formed during Platelet Shape Change," *Nature,* vol. 293, pp. 302-305, 1981.

[19] M. Coue, S. L. Brenner, I. Spector, and E. D. Korn, "Inhibition of Actin Polymerization by Latrunculin-A," *Febs Letters,* vol. 213, pp. 316-318, Mar 1987.

[20] T. Wakatsuki, B. Schwab, N. C. Thompson, and E. L. Elson, "Effects of cytochalasin D and latrunculin B on mechanical properties of cells," *Journal of Cell Science,* vol. 114, pp. 1025-1036, Mar 2001.

[21] J. A. Cooper, "Effects of Cytochalasin and Phalloidin on Actin," *Journal of Cell Biology,* vol. 105, pp. 1473-1478, Oct 1987.

[22] J. E. B. Fox, "3 - Platelet Contractile Proteins," in *Biochemistry of Platelets*, D. R. P. A. Shuman, Ed., ed: Academic Press, 1986, pp. 115-157.

[23] E. M. De La Cruz, E. M. Ostap, R. A. Brundage, K. S. Reddy, H. L. Sweeney, and D. Safer, "Thymosin-beta(4) changes the conformation and dynamics of actin monomers," *Biophysical Journal,* vol. 78, pp. 2516-2527, May 2000.

[24] C. G. Dos Remedios, D. Chhabra, M. Kekic, I. V. Dedova, M. Tsubakihara, D. A. Berry, and N. J. Nosworthy, "Actin Binding Proteins: Regulation of Cytoskeletal Microfilaments," *Physiological Reviews,* vol. 83, pp. 433-473, Apr 2003.

[25] A. Weber, C. R. Pennise, G. G. Babcock, and V. M. Fowler, "Tropomodulin Caps the Pointed Ends of Actin-filaments," *Journal of Cell Biology,* vol. 127, pp. 1627-1635, Dec 1994.

[26] J. F. Casella, D. J. Maack, and S. Lin, "Purification and initial Characterization of a Protein from Skeletal-muscle that caps the Barbed ends of Actin-filaments," *Journal of Biological Chemistry,* vol. 261, pp. 915-921, Aug 1986.

[27] J. R. Glenney, P. Kaulfus, P. Matsudaira, and K. Weber, "F-actin Binding and Bundling Properties of Fimbrin, a Major Cytoskeletal Protein of Microvillus Core Filaments," *Journal of Biological Chemistry,* vol. 256, pp. 9283-9288, 1981.

[28] T. D. Pollard, L. Blanchoin, and R. D. Mullins, "Molecular mechanisms controlling actin filament dynamics in nonmuscle cells," *Annual Review of Biophysics and Biomolecular Structure,* vol. 29, pp. 545-576, 2000.

[29] A. Bretscher and K. Weber, "Villin is a Major Protein of the Microvillus Cytoskeleton which Binds both G-actin and F-actin in a Calcium-dependent Manner," *Cell,* vol. 20, pp. 839-847, 1980.

[30] R. A. Edwards and J. Bryan, "Fascins, a Family of Actin Bundling Proteins," *Cell Motility and the Cytoskeleton,* vol. 32, pp. 1-9, 1995.

[31] S. L. Brenner and E. D. Korn, "Spectrin-actin Interaction - Phosphorylated and Dephosphorylated Spectrin Tetramer Cross-link F-actin," *Journal of Biological Chemistry,* vol. 254, pp. 8620-8627, 1979.

[32] A. H. Ahn and L. M. Kunkel, "The Structural and Functional Diversity of Dystrophin," *Nature Genetics,* vol. 3, pp. 283-291, Apr 1993.

[33] D. H. Wachsstock, W. H. Schwarz, and T. D. Pollard, "Cross-linker Dynamics Determine the Mechanical-properties of Actin Gels," *Biophysical Journal,* vol. 66, pp. 801-809, Mar 1994.

[34] G. M. Cooper, *The Cell: A Molecular Approach*, 2nd ed.: Sinauer Associates, 2000.

[35] V. Bennett and D. M. Gilligan, "The Spectrin-based Membrane Skeleton and Micron-scale Organization of the Plasma-Membrane," *Annual Review of Cell Biology,* vol. 9, pp. 27-66, 1993.

[36] R. A. Anderson and R. E. Lovrien, "Glycophorin is linked by Band-4.1 Protein to the Human-erythrocyte Membrane Skeleton," *Nature,* vol. 307, pp. 655-658, 1984.

[37] A. J. Ridley and A. Hall, "The small GTP-binding protein rho regulates the assembly of focal adhesions and actin stress fibers in response to growth factors," *Cell,* vol. 70, pp. 389-399, 1992.

[38] S. Miyamoto, H. Teramoto, O. A. Coso, J. S. Gutkind, P. D. Burbelo, S. K. Akiyama, and K. M. Yamada, "Integrin Function - Molecular Hierarchies of Cytoskeletal and Signaling Molecules," *Journal of Cell Biology,* vol. 131, pp. 791-805, Nov 1995.

[39] A. F. Huxley and R. Niedergerke, "Structural changes in muscle during contraction; interference microscopy of living muscle fibres," *Nature,* vol. 173, pp. 971-3, 1954 May 1954.

[40] H. Huxley and J. Hanson, "Changes in the Cross-striations of Muscle during Contraction and Stretch and their Structural Interpretation," *Nature,* vol. 173, pp. 973-6, 1954 May 1954.

[41] J. R. Sellers, "Myosins: a diverse superfamily," *Biochimica Et Biophysica Acta-Molecular Cell Research,* vol. 1496, pp. 3-22, Mar 2000.

[42] M. S. Mooseker and R. E. Cheney, "Unconventional myosins," *Annual Review of Cell and Developmental Biology,* vol. 11, pp. 633-675, 1995.

[43] M. Kneussel and W. Wagner, "Myosin motors at neuronal synapses: drivers of membrane transport and actin dynamics," *Nature Reviews Neuroscience,* vol. 14, pp. 233-247, Apr 2013.

[44] M. A. Geeves and K. C. Holmes, "Structural mechanism of muscle contraction," *Annual Review of Biochemistry,* vol. 68, pp. 687-728, 1999.

[45] I. Rayment, W. R. Rypniewski, K. Schmidtbase, R. Smith, D. R. Tomchick, M. M. Benning, D. A. Winkelmann, G. Wesenberg, and H. M. Holden, "3-Dimensional Structure of Myosin Subfragment-1 - A Molecular Motor," *Science,* vol. 261, pp. 50-58, Jul 1993.

[46] M. Schliwa and G. Woehlke, "Molecular motors," *Nature,* vol. 422, pp. 759-765, Apr 2003.

[47] K. Kitamura, M. Tokunaga, A. H. Iwane, and T. Yanagida, "A single myosin head moves along an actin filament with regular steps of 5.3 nanometres," *Nature,* vol. 397, pp. 129-134, Jan 1999.

[48] M. L. Walker, S. A. Burgess, J. R. Sellers, F. Wang, J. A. Hammer, J. Trinick, and P. J. Knight, "Two-headed binding of a processive myosin to F-actin," *Nature,* vol. 405, pp. 804-+, Jun 2000.

[49] C. Veigel, M. L. Bartoo, D. C. S. White, J. C. Sparrow, and J. E. Molloy, "The stiffness of rabbit skeletal actomyosin cross-bridges determined with an optical tweezers transducer," *Biophysical Journal,* vol. 75, pp. 1424-1438, Sep 1998.

[50] H. Tanaka, K. Homma, A. H. Iwane, E. Katayama, R. Ikebe, J. Saito, T. Yanagida, and M. Ikebe, "The motor domain determines the large step of myosin-V," *Nature,* vol. 415, pp. 192-195, Jan 2002.

[51] S. S. Margossian and S. Lowey, "Preparation of Myosin and its Subfragments from Rabbit Skeletal-muscle," *Methods in Enzymology,* vol. 85, pp. 55-71, 1982.

[52] Y. Y. Toyoshima, S. J. Kron, E. M. McNally, K. R. Niebling, C. Toyoshima, and J. A. Spudich, "Myosin subfragment-1 is sufficient to move actin filaments in vitro," *Nature,* vol. 328, pp. 536-539, 1987.

[53] B. Guo and W. H. Guilford, "The Tail of Myosin Reduces Actin Filament Velocity in the In Vitro Motility Assay," *Cell Motility and the Cytoskeleton,* vol. 59, pp. 264-272, 2004.

[54] J. Howard, *Mechanics of motor proteins and the cytoskeleton*: Sinauer Associates Inc., 2001.

[55] M. P. Sheetz and J. A. Spudich, "Movement of Myosin-coated Fluorescent Beads on Actin Cable Invitro," *Nature,* vol. 303, pp. 31-35, 1983.

[56] S. J. Kron and J. A. Spudich, "Fluorescent Actin-filaments Move on Myosin fixed to a Glass-surface," *Proceedings of the National Academy of Sciences of the United States of America,* vol. 83, pp. 6272-6276, Sep 1986.

[57] H. Hess and V. Vogel, "Molecular shuttles based on motor proteins: active transport in synthetic environments," *Reviews in Molecular Biotechnology,* vol. 82, pp. 67-85, 2001.

[58] Y. Harada, K. Sakurada, T. Aoki, D. D. Thomas, and T. Yanagida, "Mechanochemical coupling in actomyosin energy transduction studied by invitro movement assay," *Journal of Molecular Biology,* vol. 216, pp. 49-68, Nov 1990.

[59] D. V. Nicolau, H. Suzuki, S. Mashiko, T. Taguchi, and S. Yoshikawa, "Actin Motion on Microlithographically Functionalized Myosin Surfaces and Tracks," *Biophysical Journal,* vol. 77, pp. 1126-1134, 1999.

[60] J. A. Jaber, P. B. Chase, and J. B. Schlenoff, "Actomyosin-driven Motility on Patterned Polyelectrolyte Mono- and Multilayers," *Nano Letters,* vol. 3, pp. 1505-1509, Nov 2003.

[61] N. Albet-Torres, J. O'Mahony, C. Charlton, M. Balaz, P. Lisboa, T. Aastrup, A. Mansson, and I. A. Nicholls, "Mode of heavy meromyosin adsorption and motor function correlated with surface hydrophobicity and charge," *Langmuir,* vol. 23, pp. 11147-11156, Oct 2007.

[62] J. T. Finer, R. M. Simmons, and J. A. Spudich, "Single myosin molecule mechanics - piconewton forces and nanometer steps," *Nature,* vol. 368, pp. 113-119, Mar 1994.

[63] T. Nishizaka, H. Miyata, H. Yoshikawa, S. Ishiwata, and K. Kinosita, "Unbinding Force of a Single Motor Molecule of Muscle Measured using Optical Tweezers," *Nature,* vol. 377, pp. 251-254, Sep 1995.

[64] M. J. Tyska, D. E. Dupuis, W. H. Guilford, J. B. Patlak, G. S. Waller, K. M. Trybus, D. M. Warshaw, and S. Lowey, "Two heads of myosin are better than one for generating force and motion," *Proceedings of the National Academy of Sciences of the United States of America,* vol. 96, pp. 4402-4407, Apr 1999.

[65] K. Saito, T. Aoki, and T. Yanagida, "Movement of Single Myosin-filaments and Myosin Step-size on an Actin Filament suspended in Solution by a Laser Trap," *Biophysical Journal,* vol. 66, pp. 769-777, Mar 1994.

[66] N. Suzuki, H. Miyata, S. Ishiwata, and K. Kinosita, "Preparation of bead-tailed actin filaments: Estimation of the torque produced by the sliding force in an in vitro motility assay," *Biophysical Journal,* vol. 70, pp. 401-408, Jan 1996.

[67] J. Howard, A. J. Hudspeth, and R. D. Vale, "Movement of Microtubule by Single Kinesin Molecules," *Nature,* vol. 342, pp. 154-158, Nov 1989.

[68] A. D. Mehta, R. S. Rock, M. Rief, J. A. Spudich, M. S. Mooseker, and R. E. Cheney, "Myosin-V is a processive actin-based motor," *Nature,* vol. 400, pp. 590-593, Aug 1999.

[69] M. Tominaga, H. Kojima, E. Yokota, H. Orii, R. Nakamori, E. Katayama, M. Anson, T. Shimmen, and K. Oiwa, "Higher plant myosin XI moves processively on actin with 35 nm steps at high velocity," *Embo Journal,* vol. 22, pp. 1263-1272, Mar 2003.

[70] Y. Y. Toyoshima, S. J. Kron, and J. A. Spudich, "The Myosin Step Size - Measurement of the Unit Displacement per ATP hydrolyzed in an Invitro Assay," *Proceedings of the National Academy of Sciences of the United States of America,* vol. 87, pp. 7130-7134, Sep 1990.

[71] T. Q. P. Uyeda, S. J. Kron, and J. A. Spudich, "Myosin step size: estimation from slow sliding movement of actin over low densities of heavy meromyosin," *Journal of Molecular Biology,* vol. 214, pp. 699-710, 1990.

[72] K. Kawaguchi and S. i. Ishiwata, "Temperature Dependence of Force, Velocity, and Processivity of Single Kinesin Molecules," *Biochemical and Biophysical Research Communications,* vol. 272, pp. 895-899, 2000.

[73] M. Kawai, K. Kawaguchi, M. Saito, and S. Ishiwata, "Temperature change does not affect force between single actin filaments and HMM from rabbit muscles," *Biophysical Journal,* vol. 78, pp. 3112-3119, Jun 2000.

[74] R. C. Woledge, N. A. Curtin, and E. Homsher, *Energetic Aspects of Muscle Contraction*: Academic Press, 1985.

[75] H. Suzuki, A. Yamada, K. Oiwa, H. Nakayama, and S. Mashiko, "Control of Actin moving Trajectory by Patterned poly(methyl methacrylate) Tracks," *Biophysical Journal,* vol. 72, pp. 1997-2001, May 1997.

[76] Y. Arai, R. Yasuda, K. Akashi, Y. Harada, H. Miyata, K. Kinosita, and H. Itoh, "Tying a molecular knot with optical tweezers," *Nature,* vol. 399, pp. 446-448, Jun 1999.

[77] R. Bunk, J. Klinth, L. Montelius, I. A. Nicholls, P. Omling, S. Tågerud, and A. Månsson, "Actomyosin Motility on Nanostructured Surfaces," *Biochemical and Biophysical Research Communications,* vol. 301, pp. 783-788, 2003.

[78] R. Bunk, P. Carlberg, A. Mansson, I. A. Nicholls, P. Omling, M. Sundberg, S. Tagerud, and L. Montelius, "Guiding molecular motors with nano-imprinted structures," *Japanese Journal of Applied Physics Part 1-Regular Papers Brief Communications & Review Papers,* vol. 44, pp. 3337-3340, May 2005.

[79] R. Bunk, M. Sundberg, A. Mansson, I. A. Nicholls, P. Omling, S. Tagerud, and L. Montelius, "Guiding motor-propelled molecules with nanoscale precision through silanized bi-channel structures," *Nanotechnology,* vol. 16, pp. 710-717, Jun 2005.

[80] H. Hess, J. Clemmens, C. M. Matzke, G. D. Bachand, B. C. Bunker, and V. Vogel, "Ratchet patterns sort molecular shuttles," *Applied Physics a-Materials Science & Processing,* vol. 75, pp. 309-313, Aug 2002.

[81] S. G. Moorjani, L. Jia, T. N. Jackson, and W. O. Hancock, "Lithographically patterned channels spatially segregate kinesin motor activity and effectively guide microtubule movements," *Nano Letters,* vol. 3, pp. 633-637, May 2003.

[82] L. L. Jia, S. G. Moorjani, T. N. Jackson, and W. O. Hancock, "Microscale transport and sorting by kinesin molecular motors," *Biomedical Microdevices,* vol. 6, pp. 67-74, Mar 2004.

[83] M. G. L. van den Heuvel, C. T. Butcher, R. M. M. Smeets, S. Diez, and C. Dekker, "High rectifying efficiencies of microtubule motility on kinesin-coated gold nanostructures," *Nano Letters,* vol. 5, pp. 1117-1122, Jun 2005.

[84] Y. M. Huang, M. Uppalapati, W. O. Hancock, and T. N. Jackson, "Microfabricated capped channels for biomolecular motor-based transport," *Ieee Transactions on Advanced Packaging,* vol. 28, pp. 564-570, Nov 2005.

[85] Y. M. Huang, M. Uppalapati, W. O. Hancock, and T. N. Jackson, "Microtubule transport, concentration and alignment in enclosed microfluidic channels," *Biomedical Microdevices,* vol. 9, pp. 175-184, Apr 2007.

[86] M. G. L. van den Heuvel, M. P. De Graaff, and C. Dekker, "Molecular sorting by electrical steering of microtubules in kinesin-coated channels," *Science,* vol. 312, pp. 910-914, May 2006.

[87] K. J. Bohm, J. Beeg, G. M. zu Horste, R. Stracke, and E. Unger, "Kinesin-driven sorting machine on large-scale microtubule arrays," *Ieee Transactions on Advanced Packaging,* vol. 28, pp. 571-576, Nov 2005.

[88] D. Turner, C. Y. Chang, K. Fang, P. Cuomo, and D. Murphy, "Kinesin movement on glutaraldehyde-fixed microtubules," *Analytical Biochemistry,* vol. 242, pp. 20-25, Nov 1996.

[89] K. J. Bohm, R. Stracke, P. Muhlig, and E. Unger, "Motor protein-driven unidirectional transport of micrometer-sized cargoes across isopolar microtubule arrays," *Nanotechnology,* vol. 12, pp. 238-244, Sep 2001.

[90] H. Morgan, M. P. Hughes, and N. G. Green, "Separation of submicron bioparticles by dielectrophoresis," *Biophysical Journal,* vol. 77, pp. 516-525, 1999.

[91] R. D. Miller and T. B. Jones, "Electro-orientation of Ellipsoidal Erythrocytes - Theory and Experiment," *Biophysical Journal,* vol. 64, pp. 1588-1595, May 1993.

[92] J. A. Spudich and S. Watt, "Regulation of Rabbit Skeletal Muscle Contraction. 1.Biochemical Studies of Interaction of Tropomyosin-Troponin Complex with Actin and Proteolytic Fragments of Myosin," *Journal of Biological Chemistry,* vol. 246, pp. 4866-4871, 1971.

[93] T. M. Svitkina, A. B. Verkhovsky, and G. G. Borisy, "Improved procedures for electron microscopic visualization of the cytoskeleton of cultured cells," *Journal of Structural Biology*, vol. 115, pp. 290-303, Nov-Dec 1995.

[94] R. Ishikawa, T. Sakamoto, T. Ando, S. Higashi-Fujime, and K. Kohama, "Polarized actin bundles formed by human fascin-1: their sliding and disassembly on myosin II and myosin V in vitro," *Journal of Neurochemistry*, vol. 87, pp. 676-685, Nov 2003.

[95] H. Ris, "The cytoplasmic Filament System in Critical-point dried Whole Mounts and Plastic-embedded Sections," *Journal of Cell Biology*, vol. 100, pp. 1474-1487, 1985.

[96] D. Braunstein, "Imaging an F-actin Structure with Noncontact Scanning Force Microscopy," *Journal of Vacuum Science & Technology a-Vacuum Surfaces and Films*, vol. 13, pp. 1733-1736, May-Jun 1995.

[97] J. S. Bunch, T. N. Rhodin, and P. L. McEuen, "Noncontact-AFM imaging of molecular surfaces using single-wall carbon nanotube technology," *Nanotechnology*, vol. 15, p. S76, 2004.

[98] M. T. Postek, *Scanning Electron Microscopy: A Student's Handbook*: Ladd Research Industries, Incorporated, 1980.

[99] H. L. Yin and T. P. Stossel, "Control of Cytoplasmic Actin Gel-sol Transformation by Gelsolin, a Calcium-dependent Regulatory Protein," *Nature*, vol. 281, pp. 583-586, 1979.

[100] H. E. Harris and A. G. Weeds, "Plasma Gelsolin Caps and Severs Actin-filaments," *Febs Letters*, vol. 177, pp. 184-188, 1984.

[101] P. A. Janmey and T. P. Stossel, "Modulation of Gelsolin Function by Phosphatidylinositol 4,5-Bisphosphate," *Nature*, vol. 325, pp. 362-364, Jan 1987.

[102] P. A. Janmey, K. Iida, H. L. Yin, and T. P. Stossel, "Polyphosphoinositide Micelles and Polyphosphoinositide-containing Vesicles Dissociate Endogenous Gelsolin-actin Complexes and Promote Actin Assmebly from the Fast-growing end of Actin-filaments blocked by Gelsolin," *Journal of Biological Chemistry*, vol. 262, pp. 12228-12236, Sep 1987.

[103] H. L. Yin, "Gelsolin - Calcium-regulated and Polyphosphoinositide-regulated Actin-modulating Protein," *Bioessays*, vol. 7, pp. 176-179, Oct 1987.

[104] C. C. Cunningham, T. P. Stossel, and D. J. Kwiatkowski, "Enhanced Motility in NIH-3T3 Fibroblasts that Overexpress Gelsolin," *Science*, vol. 251, pp. 1233-1236, Mar 1991.

[105] L. D. Burtnick, E. K. Koepf, J. Grimes, E. Y. Jones, D. I. Stuart, P. J. McLaughlin, and R. C. Robinson, "The crystal structure of plasma gelsolin: Implications for actin severing, capping, and nucleation," *Cell*, vol. 90, pp. 661-670, Aug 1997.

[106] L. A. Selden, H. J. Kinosian, J. Newman, B. Lincoln, C. Hurwitz, L. C. Gershman, and J. E. Estes, "Severing of F-Actin by the amino-terminal half of gelsolin suggests internal cooperativity in gelsolin," *Biophysical Journal*, vol. 75, pp. 3092-3100, Dec 1998.

[107] J. G. Kiselar, P. A. Janmey, S. C. Almo, and M. R. Chance, "Visualizing the Ca2+-dependent activation of gelsolin by using synchrotron footprinting," *Proceedings of the National Academy of Sciences of the United States of America*, vol. 100, pp. 3942-3947, Apr 2003.

[108] S. Nag, Q. Ma, H. Wang, S. Chumnarnsilpa, W. L. Lee, M. Larsson, B. Kannan, M. Hernandez-Valladarez, L. D. Burtnick, and R. C. Robinson, "Ca(2+) Binding by Domain 2 Plays a Critical Role in the Activation and Sabilization of Gelsolin," *Proceedings of the National Academy of Sciences of the United States of America*, vol. 106, pp. 13713-13718, Aug 2009.

[109] P. G. Allen and P. A. Janmey, "Gelsolin Displaces Phalloidin from Actin-filaments - a new Fluorescence Method shows that both Ca2+ and Mg2+ effect the rate at which Gelsolin severs F-actin," *Journal of Biological Chemistry*, vol. 269, pp. 32916-32923, Dec 1994.

[110] H. J. Kinosian, L. A. Selden, J. E. Estes, and L. C. Gershman, "Kinetics of gelsolin interaction with phalloidin-stabilized F-actin, rate constants for binding and severing," *Biochemistry*, vol. 35, pp. 16550-16556, Dec 1996.

[111] H. J. Kinosian, J. Newman, B. Lincoln, L. A. Selden, L. C. Gershman, and J. E. Estes, "Ca2+ Regulation of Gelsolin Activity: Binding and Severing of F-actin," *Biophysical Journal*, vol. 75, pp. 3101-3109, Dec 1998.

[112] K. M. Lin, M. Mejillano, and H. L. Yin, "Ca2+ Regulation of Gelsolin by its C-terminal Tail," *Journal of Biological Chemistry*, vol. 275, pp. 27746-27752, Sep 2000.

[113] C. Roustan, I. Ferjani, S. K. Maciver, A. Fattoum, B. Rebiere, and Y. Benyarnin, "Calcium-induced Conformational Changes in the Amino-terminal half of Gelsolin," *Febs Letters*, vol. 581, pp. 681-686, Feb 2007.

[114] J. A. Lamb, P. G. Allen, B. Y. Tuan, and P. A. Janmey, "Modulation of Gelsolin Function - Activation at low pH overrides Ca2+ Requirement," *Journal of Biological Chemistry*, vol. 268, pp. 8999-9004, Apr 1993.

[115] H. Choe, L. D. Burtnick, M. Mejillano, H. L. Yin, R. C. Robinson, and S. Choe, "The Calcium Activation of Gelsolin: Insights from the 3 Angstrom Structure of the G4-G6/actin complex," *Journal of Molecular Biology*, vol. 324, pp. 691-702, Dec 2002.

[116] P. J. McLaughlin, J. T. Gooch, H. G. Mannherz, and A. G. Weeds, "Structure of Gelsolin Segment-1 - Actin Complex and the Mechanism of Filament Severing," *Nature*, vol. 364, pp. 685-692, Aug 1993.

[117] L. D. Burtnick, D. Urosev, E. Irobi, K. Narayan, and R. C. Robinson, "Structure of the N-terminal half of gelsolin bound to actin: roles in severing, apoptosis and FAF," *Embo Journal*, vol. 23, pp. 2713-2722, Jul 2004.

[118] B. J. Pope, J. T. Gooch, and A. G. Weeds, "Probing the effects of calcium on gelsolin," *Biochemistry*, vol. 36, pp. 15848-15855, Dec 1997.

[119] Ashish, M. S. Paine, P. B. Perryman, L. Yang, H. L. Yin, and J. K. Krueger, "Global structure changes associated with Ca2+ activation of full-length human plasma gelsolin," *Journal of Biological Chemistry*, vol. 282, pp. 25884-25892, Aug 2007.

[120] E. L. Bearer, "Direct Observation of Actin Filament Severing by Gelsolin and Binding Gcap39 and Capz," *Journal of Cell Biology*, vol. 115, pp. 1629-1638, Dec 1991.

[121] J. E. Estes, L. A. Selden, and L. C. Gershman, "Mechanism of Action of Phalloidin on the Polymerization of Muscle Actin," *Biochemistry*, vol. 20, pp. 708-712, 1981.

[122] http://www.rcsb.org/pdb/home/home.do.

[123] S. Gallagher, S. E. Winston, S. A. Fuller, and J. G. R. Hurrell, "Immunoblotting and immunodetection," *Current protocols in molecular biology / edited by Frederick M. Ausubel ... [et al.]*, vol. Chapter 10, p. Unit 10.8, 2008.

[124] M. Steinitz, "Quantitation of the blocking effect of tween 20 and bovine serum albumin in ELISA microwells," *Analytical Biochemistry*, vol. 282, pp. 232-238, Jul 2000.

[125] H. Q. Sun, M. Yamamoto, M. Mejillano, and H. L. Yin, "Gelsolin, a multifunctional actin regulatory protein," *Journal of Biological Chemistry*, vol. 274, pp. 33179-33182, Nov 1999.

[126] S. Khaitlina and H. Hinssen, "Ca-Dependent Binding of Actin to Gelsolin," *Febs Letters*, vol. 521, pp. 14-18, Jun 2002.

[127] T. Shimmen and M. Yano, "Active Sliding Movement of Latex Beads coated with Skeletal-muscle Myosin on Chara Actin Bundles," *Protoplasma*, vol. 121, pp. 132-137, 1984.

[128] K. Oiwa, S. Chaen, E. Kamitsubo, T. Shimmen, and H. Sugi, "Steady-state Froce Velocity Relation in the ATP-dependent Sliding Movement of Myosin-coated Beads on Actin Cables Invitro Studied with a Centrifuge Microscope," *Proceedings of the National Academy of Sciences of the United States of America*, vol. 87, pp. 7893-7897, Oct 1990.

[129] N. Hirokawa, "Kinesin and dynein superfamily proteins and the mechanism of organelle transport," *Science*, vol. 279, pp. 519-526, Jan 1998.

[130] R. D. Vale, "The molecular motor toolbox for intracellular transport," *Cell*, vol. 112, pp. 467-480, Feb 2003.

[131] H. E. Huxley, "Mechanism of Muscular Contraction," *Science*, vol. 164, pp. 1356-&, 1969.

[132] R. S. Adelstein and E. Eisenberg, "Regulation and Kinetics of the Actin-myosin-ATP interaction," *Annual Review of Biochemistry*, vol. 49, pp. 921-956, 1980.

[133] M. P. Sheetz, R. Chasan, and J. A. Spudich, "ATP-dependent Movement of Myosin Invitro - Characterization of A Quantitative Assay," *Journal of Cell Biology*, vol. 99, pp. 1867-1871, 1984.

[134] H. Hess, G. D. Bachand, and V. Vogel, "Powering nanodevices with biomolecular motors," *Chemistry-a European Journal*, vol. 10, pp. 2110-2116, May 2004.

[135] T. Mitchison and M. Kirschner, "Dynamic Instability of Microtubule Growth," *Nature*, vol. 312, pp. 237-242, 1984.

[136] T. Mitchison and M. Kirschner, "Cytoskeletal Dynamics and Nerve Growth," *Neuron*, vol. 1, pp. 761-772, Nov 1988.

[137] M. D. Welch, A. Mallavarapu, J. Rosenblatt, and T. J. Mitchison, "Actin Dynamics in vivo," *Current Opinion in Cell Biology*, vol. 9, pp. 54-61, Feb 1997.

[138] Y. Lee and P. Famouri, "The movement of actin–myosin biomolecular linear motor under AC electric fields: An experimental study," *Journal of Colloid and Interface Science*, vol. 394, pp. 312-318, 2013.

[139] H. Hess, J. Clemmens, D. Qin, J. Howard, and V. Vogel, "Light-Controlled Molecular Shuttles Made from Motor Proteins Carrying Cargo on Engineered Surfaces," *Nano Letters*, vol. 1, pp. 235-239, 2001/05/01 2001.

[140] J. Clemmens, H. Hess, R. Doot, C. M. Matzke, G. D. Bachand, and V. Vogel, "Motor-protein "roundabouts": Microtubules moving on kinesin-coated tracks through engineered networks," *Lab on a Chip*, vol. 4, pp. 83-86, 2004.

[141] L. Limberis, J. J. Magda, and R. J. Stewart, "Polarized alignment and surface immobilization of microtubules for kinesin-powered nanodevices," *Nano Letters*, vol. 1, pp. 277-280, May 2001.

[142] T. B. Brown and W. O. Hancock, "A polarized microtubule array for kinesin-powered-nanoscale assembly and force generation," *Nano Letters*, vol. 2, pp. 1131-1135, Oct 2002.

[143] J. Z. Yuan, A. Pillarisetti, Y. E. Goldman, and H. H. Bau, "Orienting Actin Filaments for Directional Motility of Processive Myosin Motors," *Nano Letters*, vol. 13, pp. 79-84, Jan 2013.

[144] A. Kakugo, S. Sugimoto, J. P. Gong, and Y. Osada, "Gel machines constructed from chemically cross-linked actins and myosins," *Advanced Materials*, vol. 14, pp. 1124-1126, Aug 2002.

[145] E. Prochniewicz and T. Yanagida, "Inhibition of Sliding Movement of F-actin by Cross-linking Emphasizes the Role of Actin Structure in the Mechanism of Motility," *Journal of Molecular Biology*, vol. 216, pp. 761-772, Dec 1990.

[146] A. Weeds, "Actin-binding Proteins - Regulators of Cell Architecture and Motility," *Nature*, vol. 296, pp. 811-816, 1982.

[147] P. K. Mattila and P. Lappalainen, "Filopodia: molecular architecture and cellular functions," *Nature Reviews Molecular Cell Biology*, vol. 9, pp. 446-454, Jun 2008.

[148] M. S. Mooseker, "Organization, Chemistry, and Assembly of the Cytoskeletal Apparatus of the Intestinal Brush-border," *Annual Review of Cell Biology*, vol. 1, pp. 209-241, 1985.

[149] N. Kureishy, V. Sapountzi, S. Prag, N. Anilkumar, and J. C. Adams, "Fascins, and their roles in cell structure and function," *Bioessays*, vol. 24, pp. 350-361, Apr 2002.

[150] S. Yamashiro, Y. Yamakita, S. Ono, and F. Matsumura, "Fascin, an actin-bundling protein, induces membrane protrusions and increases cell motility of epithelial cells," *Molecular Biology of the Cell*, vol. 9, pp. 993-1006, May 1998.

[151] R. Rezakhaniha, A. Agianniotis, J. T. C. Schrauwen, A. Griffa, D. Sage, C. V. C. Bouten, F. N. van de Vosse, M. Unser, and N. Stergiopulos, "Experimental investigation of collagen waviness and orientation in the arterial adventitia using confocal laser scanning microscopy," *Biomechanics and Modeling in Mechanobiology*, vol. 11, pp. 461-473, Mar 2012.

[152] Y. Lee, M.-Y. Wei, and P. Famouri, "A visualized observation of calcium-dependent gelsolin activity upon the surface coverage of fluorescent-tagged actin filaments," *Journal of Colloid and Interface Science*, vol. 389, pp. 182-7, 2013 Jan 1 (Epub 2012 Sep 2013.

[153] J. Berthier and P. Silberzan, *Microfluidics for Biotechnology*: Artech House, 2010.

[154] M. Sundberg, M. Balaz, R. Bunk, J. P. Rosengren-Holmberg, L. Montelius, I. A. Nicholls, P. Omling, S. Tagerud, and A. Mansson, "Selective spatial localization of actomyosin motor function by chemical surface patterning," *Langmuir*, vol. 22, pp. 7302-7312, Aug 2006.

[155] Y. Y. Toyoshima, "How are Myosin Fragments Bound to Nitrocellulose Film ?," in *Mechanism of Myofilament Sliding in Muscle Contraction*. vol. 332, H. Sugi and G. Pollack, Eds., ed: Springer US, 1993, pp. 259-265.

[156] D. Falconnet, G. Csucs, H. M. Grandin, and M. Textor, "Surface engineering approaches to micropattern surfaces for cell-based assays," *Biomaterials,* vol. 27, pp. 3044-3063, Jun 2006.

[157] F. L. Yap and Y. Zhang, "Protein and cell micropatterning and its integration with micro/nanoparticles assembly," *Biosensors & Bioelectronics,* vol. 22, pp. 775-788, Jan 2007.

[158] M. Y. Ali, E. B. Krementsova, G. G. Kennedy, R. Mahaffy, T. D. Pollard, K. M. Trybus, and D. M. Warshaw, "Myosin Va maneuvers through actin intersections and diffuses along microtubules," *Proceedings of the National Academy of Sciences of the United States of America,* vol. 104, pp. 4332-4336, Mar 2007.

[159] L. Haviv, D. Gillo, F. Backouche, and A. Bernheim-Groswasser, "A cytoskeletal demolition worker: Myosin II acts as an actin depolymerization agent," *Journal of Molecular Biology,* vol. 375, pp. 325-330, Jan 2008.

[160] S. K. Vogel, Z. Petrasek, F. Heinemann, and P. Schwille, "Myosin motors fragment and compact membrane-bound actin filaments," *eLife,* vol. 2, p. e00116, 2013 (Epub 2013 Jan 2013.

[161] T. D. Pollard and G. G. Borisy, "Cellular Motility Driven by Assembly and Disassembly of Actin Filaments," *Cell,* vol. 112, pp. 453-465, Feb 2003.

[162] W. H. Roos, A. Roth, J. Konle, H. Presting, E. Sackmann, and J. P. Spatz, "Freely suspended actin cortex models on arrays of microfabricated pillars," *Chemphyschem,* vol. 4, pp. 872-877, Aug 2003.

[163] K. Lee, J. L. Gallop, K. Rambani, and M. W. Kirschner, "Self-Assembly of Filopodia-Like Structures on Supported Lipid Bilayers," *Science,* vol. 329, pp. 1341-1345, Sep 2010.

[164] J. R. Kuhn and T. D. Pollard, "Real-time measurements of actin filament polymerization by total internal reflection fluorescence microscopy," *Biophysical Journal,* vol. 88, pp. 1387-1402, Feb 2005.

[165] I. Fujiwara, D. Vavylonis, and T. D. Pollard, "Polymerization kinetics of ADP- and ADP-P-i-actin determined by fluorescence microscopy," *Proceedings of the National Academy of Sciences of the United States of America,* vol. 104, pp. 8827-8832, May 2007.

[166] T. M. Huckaba, T. Lipkin, and L. A. Pon, "Roles of type II myosin and a tropomyosin isoform in retrograde actin flow in budding yeast," *Journal of Cell Biology,* vol. 175, pp. 957-969, Dec 2006.

[167] E. Lazarides, "Actin, Alpha-actinin, and Tropomyosin Interaction in Structural Organization of Actin-filaments in Nonmuscle Cells," *Journal of Cell Biology,* vol. 68, pp. 202-219, 1976.

[168] Y. Tseng, B. W. Schafer, S. C. Almo, and D. Wirtz, "Functional synergy of actin filament cross-linking proteins," *Journal of Biological Chemistry,* vol. 277, pp. 25609-25616, Jul 2002.

[169] A. L. Wells, A. W. Lin, L. Q. Chen, D. Safer, S. M. Cain, T. Hasson, B. I. Carragher, R. A. Milligan, and H. L. Sweeney, "Myosin VI is an actin-based motor that moves backwards," *Nature,* vol. 401, pp. 505-508, Sep 1999.